

Department of Electrical and Computer Engineering

***Real-time Digital Control of DFIG-based Wind
Generators for Grid Support***

Mohsen Mesbah

This thesis is presented for the Degree of

Doctor of Philosophy

of

Curtin University

February 2012

Declaration

To the best of my knowledge and belief this thesis contains no material previously published by any other person except where due acknowledgment has been made.

This thesis contains no material which has been accepted for the award of any other degree or diploma in any university.

Signature:.....

Date: ...18 April 2013.....

Acknowledgement

I am deeply grateful to my supervisor, Professor Syed M. Islam, for his guidance, patience and support. I am much obliged to the staff members of Electrical and Computer Engineering Department especially Zibby Cielma, Russel Wilkinson, Nicholas King, Mark Fowler, Nazanin Mohammadi, and Serguei Mokroous. I would like to thank my co-supervisor, Professor Masoum, for his assistance and support during the course of my study. Also, I need to thank my friend, Paul Moses, for his patience, encouragements and effort. I am greatly indebted to Professor Peter Wolfs, for his advice and technical solutions. Finally, I need to acknowledge the financial support from Curtin University through Curtin International Postgraduate Research Scholarship (CIPRS).

Dedication

To my dear wife Parisa for her encouragement and support

Abstract

In this thesis, a set of new converter /control techniques are developed for the Grid Side and Rotor Side converter applications in DFIG wind power generation. A real time digital simulation technique is also presented which is capable of studying in real time the performance of the DFIG wind power generator connected to grid. A number of practical control strategies for DFIGs are implemented and their performances are compared. Results show that a new improved direct power controller is able to provide very quick transient response for both the active power and the reactive power output from the DFIG wind energy conversion system. Extensive simulations and practical implementation of the algorithms on a digital controller embedded inside a digital signal processor are implemented. The hardware and software of the developed prototype DFIG control mechanism is described in detail in this dissertation. In addition, to study the effect of voltage sag and other types of transient disturbances and faults, a prototype of a fault generator using the same digital signal processor has been implemented. Effect of such disturbances on a transformer is investigated which is the nearest most probable location of a grid fault or disturbance.

Table of Content

Abstract.....	V
Table of Content	VI
List of Figures.....	VIII
List of Tables.....	XI
Chapter 1. Introduction.....	1
1.1 Introduction.....	2
1.2 Thesis outline.....	3
1.3 DFIG Structure and control.....	4
1.4 Literature review.....	6
1.5 Conclusions.....	8
1.6 References.....	8
Chapter 2. Grid Side Converter (GSC).....	11
2.1 Introduction.....	12
2.2 Direct Active Power Control.....	14
2.2.1. Direct Active Power Control Principles.....	14
2.2.2. Application of AC-DC DAPC Converter in Wind	23
2.2.3. Simulation Results.....	24
2.2.4. Conclusion.....	29
2.3 Improved Predictive Direct Power Control.....	30
2.3.1. Principles of operation.....	30
2.3.2. Simulation Results.....	32
2.3.3. Conclusions.....	39
2.4 Fuzzy Predictive Direct Power Control (FP-DPC).....	40
2.4.1. Principles of operation.....	40
2.4.2. Simulation Results	43
2.4.3. Experimental Results.....	48
2.4.4. Conclusions.....	52
2.5 Average Current Control Strategy.....	53
2.5.1. Principles of operation.....	53
2.5.2. Simulation Results.....	55
2.5.3. Conclusions.....	56

2.6 Conclusions.....	57
2.7 References.....	58
Chapter 3. Rotor Side Converter (RSC).....	59
3.1. Introduction.....	60
3.2. Control Loop Design of DFIG (based on CC).....	61
3.3. Hardware Requirements and Solutions.....	64
3.3.1. Overall system structure.....	64
3.3.2. Controller selection.....	65
3.3.3. Current Measurement Circuit.....	65
3.3.4. Voltage Measurement Circuit.....	66
3.3.5. Digital IOs.....	67
3.3.6. Resulting Designed Board.....	67
3.3.7. Intelligent Power Modules.....	67
3.4. Some Practical Considerations.....	68
3.4.1. Data samples.....	68
3.4.2. Switching when using variable frequency switching methods.....	69
3.5. Experimental Results.....	69
3.6. Conclusions.....	77
3.7. References.....	77
Chapter 4. Fault Simulator.....	78
4.1. Introduction.....	79
4.2. Fault Emulator Hardware Prototype.....	81
4.3. Voltage Sag Transient Disturbances.....	83
4.3.1. IEEE-1159 Definition of Voltage Sag.....	83
4.3.2. Causes of Voltage Sag.....	83
4.3.3. Symptoms of Voltage Sags on Power Systems.....	83
4.3.4. Voltage Sag Magnitude.....	84
4.4. Experimental Results.....	86
4.4.1. Measurement Methodology.....	91
4.4.2. Results.....	91
4.5. Conclusion.....	93
4.6. References.....	94
Chapter 5. Conclusions.....	95
5.1. Summary of Dissertation.....	96
5.2. Contributions.....	98
5.3. Future works	99

List of Figures

Fig.1.1 Various types of wind energy conversion system models.....	3
Fig.1.2 Basic scheme of DFIG.....	4
Fig.1.3 Electrical model of DFIG.....	5
Fig.1.4 Wind power generation for maximum power tracking.....	6
Fig 2.1.1. A Typical Grid Side Converter.....	12
Fig 2.2.1. Ideal structure of the new ac-dc rectification method.....	14
Fig 2.2.2. Selection of I_x and I_y (a) $I_{ave}>0$ (b) $I_{ave}<0$	15
Fig 2.2.3. Schematic for proposed DAPC method.....	17
Fig 2.2.4. Equivalent circuit of the proposed converter.....	17
Fig 2.2.5. Current and voltage vector at ac-side.....	21
Fig 2.2.6. Control block diagram for the proposed approach.....	23
Fig 2.2.7. Schematic diagram of DFIG-based wind generation systems.....	24
Fig 2.2.8. Simulation results for Case A.....	26
Fig 2.2.9. Simulation results for Case B.....	27
Fig 2.2.10. Simulation results for Case C.....	28
Fig 2.3.1. Block diagram of proposed controller.....	32
Fig 2.3.2. Steady-State Simulations: Three-phase input currents for (a) P-DPC, (b) proposed IP-DPC.....	33
Fig 2.3.3. Steady-State Simulations: input and reference voltage of converter in $\alpha - \beta$	34
Fig 2.3.4. Steady-State Simulations: input active and reactive power of converter.....	35
Fig 2.3.5. Transient simulations: Three-phase input currents for (a) P-DPC, (b) proposed IP-DPC method.....	36
Fig 2.3.6. Transient Simulations: input and reference voltage of converter in $\alpha - \beta$	37
Fig 2.3.7. Transient Simulations: input active and reactive power of converter	38
Fig 2.3.8. Transient Simulations: sampled active and reactive power bits.....	39
Fig 2.4.1. Membership functions for; (a) input error, (b) output signal.....	41
Fig 2.4.2. Graphical representation of the proposed Fuzzy signal conditioner module	42
Fig 2.4.3. Proposed rescaling fuzzy controller for; (a) active power (b) reactive power.....	43

Fig. 2.4.4. Overall block diagram of the converter with the proposed fuzzy predictive controller.....	43
Fig. 2.4.5. Total harmonic distortion of input current (THDi) for different estimation values of the inductor... ..	45
Fig. 2.4.6. Steady-state simulations: three-phase input currents for +45% estimation error of the inductor.....	45
Fig. 2.4.7. Steady-state simulations: input and reference voltage of the converter in $\alpha - \beta$	46
Fig 2.4.8. Steady-state simulations: input active and reactive powers of the converter.....	46
Fig 2.4.9. Transient simulations: Three phase input currents.....	47
Fig 2.4.10. Transient Simulations: input and reference voltage of converter.....	48
Fig 2.4.11. Transient Simulations: input active and reactive powers of converter.....	48
Fig 2.4.12. Laboratory setup.....	50
Fig 2.4.13. Experimental results: current waveforms for the P-DPC.....	50
Fig 2.4.14. Experimental results: current waveforms for the proposed FP-DPC.....	51
Fig 2.4.15. Experimental results: current waveforms for the P-DPC approach.....	51
Fig 2.4.16 Experimental results: current waveforms for the proposed FP-DPC.....	52
Fig 2.5.1. Reference current and possible actual current.....	53
Fig 2.5.2. Current controller for phase A.....	54
Fig 2.5.3. Graphical representation of the vector base ACC switching strategy.....	55
Fig 2.5.4. Three-phase input currents for SVM-based average current controller method.....	56
Fig 2.5.5. Input current and reference current for one phase in proposed method.....	56
Fig 3.1 Rotor side converter schematic diagram.....	60
Fig.3.2 The Control loop of the DFIG for CC based method.....	63
Fig 3.3 Schematic of the proposed Real Time Digital Simulation of DFIG WTG.....	64
Fig 3.4 Circuit diagram for (a) current (b) voltage measurements.....	66
Fig 3.5 Signal conditioner board.....	68
Fig 3.6. Data sample timing for variable switching frequency methods.....	69
Fig 3.7 The DFIG in the test bench.....	70
Fig 3.8 Steady-state experimental results: rotor currents.....	71
Fig 3.9 Steady-state experimental results: stator voltage and current waveforms.....	72
Fig 3.10 Transient experimental results: rotor currents.....	73
Fig 3.11 Transient experimental results: stator voltage and current waveforms.....	74
Fig 3.12 Reactive power generation.....	76

Fig 4.1. Fault ride-through capability of wind farms according to grid code.....	79
Fig 4.2. Schematics of three phase power supply fault emulator.....	82
Fig 4.3. Vector base representation of reference values for different components.....	82
Fig 4.4. Three-phase three-leg transformer representation depicting the electromagnetic couplings.....	86
Fig 4.5. Impact of three-phase symmetrical sag imposed upon transformer terminals.....	87
Fig 4.6. Impact of three-phase symmetrical sag imposed upon transformer terminals.....	88
Fig 4.7. Impact of three-phase symmetrical sag imposed upon transformer terminals.....	89
Fig 4.8. Impact of three-phase unsymmetrical sag imposed upon transformer terminals.....	90
Fig 4.9. Measured effects of different sag recovery angles ϕ_{end} (symmetrical sag conditions).....	90
Fig 4.10. Measured effects of different sag recovery angle ϕ_{end} in phase <i>a</i> only.....	91

List of Tables

TABLE 2.2.1 Operational modes the proposed ac-dc current converter.....	16
TABLE 2.3.1 Parameters used in simulations.....	32
TABLE 2.4.1 Three-phase rectifier parameters used in simulations.....	44
TABLE 2.4.2 Three-phase rectifier parameters used in Experimentations.....	49
TABLE 2.5.1 Switch selection table.....	54
TABLE 2.5.2 Parameters for the simulate system.....	55
TABLE 3.1 experimental results: harmonic content of Phase A stator current	75
TABLE 4.1Transformer Electric Circuit Test Data.....	93

Chapter 1

Introduction

1.1. Introduction

Future trend of energy production is moving towards a higher share of renewable energy sources driven by global warming issues and the desire to reduce dependence on fossil fuels. Between the possible renewable energy sources, wind power generation is one of the most attractive options. The availability in different areas and more favourable economics of generating large scale power from wind makes wind power generation a commercially viable option.

The Renewable Energy Target (RET) implemented by government in 2009 is designed to ensure that 20 per cent of Australia's electricity supply will come from renewable sources by 2020. This ambitious target can be met more realistically with wind power among other renewable sources, due to favourable wind profiles in many locations in Australia and the well matured technology of wind turbines that provide more reliable solution for grid integration.

Wind power generation operates on the principle of energy conversion in air mass particle movement with linear kinetic energy which is converted from mechanical energy into electrical energy using wind turbines and electrical generators. Wind power generators are mainly asynchronous machines which have the advantage of being cheaper, low maintenance, and is highly suitable for wind applications for its variable speed operation i.e. Doubly Fed Induction Generators (DFIGs)..

There are generally four accepted electrical configurations for wind energy conversion systems currently in use which are summarized in Fig 1.1. Among four major electrical configurations, Type 3 and Type 4 using induction generators are the most common configurations. Nevertheless, these configurations contribute reactive power generation as well as active power. For Type 4 the generated power at stator terminals converts to dc power and then it is injected to the grid using a DC/AC converter. In this case, the entire generated power passes through the switching components which typically results in approximately 10 percent power loss. However, Type 3 with doubly-fed induction generators (DFIG) using wound rotor type asynchronous machines offer a more efficient solution while only a small portion of total power passes through the rotor-side converter and the stator is directly connected to grid. Needless to say, as a result of less power delivery through power electronics devices the size and cost of converters would be much less than Type 4. Less power dissipation means less cooling expenses as well. So, it is more cost-effective to choose Type 3 configuration as the stator connects directly to the grid. However, there are concerns about operational difficulties of the machine in case of grid voltage disturbances.

In general, variety of control methods exist but due to importance and novelty of DFIG concept, different control methods in rotor-side and grid-side converter and their effects on performance of wind power generator needs to be investigated.

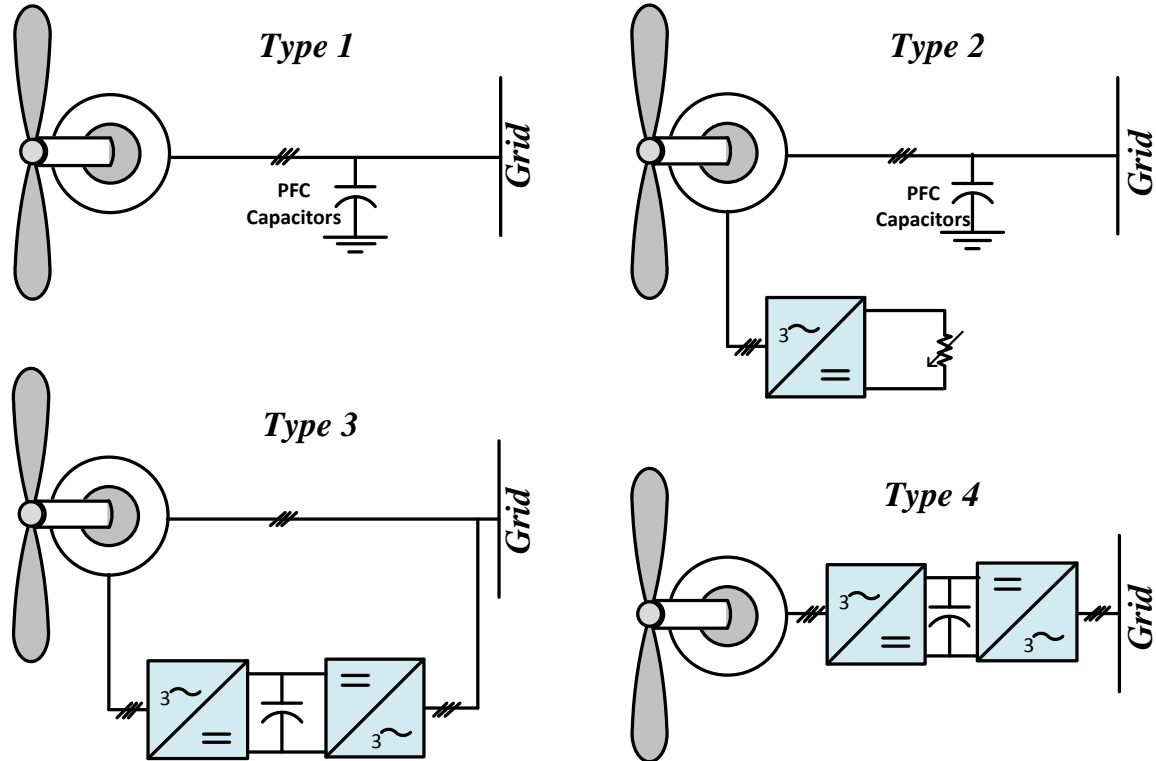


Fig.1.1 Various types of wind energy conversion system models

1.2. Thesis outline

The later part of this Chapter provides background and a brief literature review of the existing methods associated with the PWM converters that can possibly be adapted for DFIG based wind turbine generators.

In chapter two, some novel control methods have been presented and compared with some conventional methods for grid side converter (GSC). The methods include direct active power control, improved predictive direct power control, fuzzy predictive direct power control, and average current control. The new converters and control methods have been studied using simulations in Matlab Simulink. However, due to importance of the proposed fuzzy predictive method and the necessity to validate the control approach, the method has also been validated using experimental results. The prototype is based on TMS320F28335 DSP with intelligent power modules used for the switches. The prototype has been tested up to 8 KW and results are scalable.

Chapter 3 focuses on the development of the rotor side converter (RSC) and the digital control related issues of this converter. In this chapter the implementation details of the developed prototype is presented. For the implemented prototype the same DSP and intelligent power modules as for GSC

have been used. The RSC prototype is capable of generating up to 4KW active power and the results are scalable.

Chapter 4 presents a fault simulator device that can generate any type of grid faults such as the three phase faults on the generator terminals etc. The design details including the theoretical formulation of the controller and some experimental results are presented in this section. The device is useful in power component testing applications for generating voltage harmonics, unbalance grid voltages, DC bias, voltage sag, voltage swell, etc. In order to demonstrate the practical applications of this experimental prototype, a practical test of the device operation of the device for studying balanced and unbalanced voltage sags on a three leg three phase transformer has been performed.

The conclusions and summary of the work along with some future developments are discussed in chapter 5.

1.3. DFIG Structure and control

Fig.1.2 shows the basic scheme of a Doubly-fed wind turbine generator where the stator side connects directly to grid via a transformer. As there are reasonably large distances between each wind turbine in a wind farm, the transformer is usually placed to increase voltage level in order to have lower power dissipation in wind farm (Bogalecka E., 2008). The converter size depends on the machines slip and usually does not exceed 25-35% of the machine's nominal power, that makes the converter to be smaller in size compared to full converter wind power generator, and the whole system is made more cost effective. Different types of AC/AC or AC/DC/AC converters have been reported in literature (Hansen et al., 2001). But the most common topology for this application is using three phase voltage source back-to-back converter.

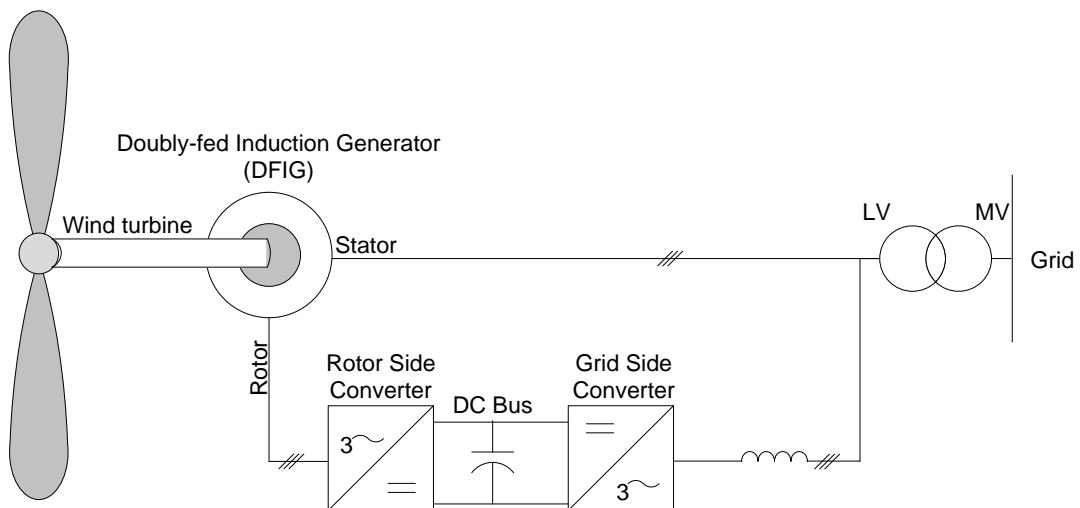


Fig.1.2 Basic scheme of DFIG

The back-to-back converter consists of two different parts, the Rectifier and the Inverter. The rectifier is to maintain DC bus voltage constant and the inverter connected to rotor side is to control the power generation. The electrical model for DFIG is shown in Fig.1.3.

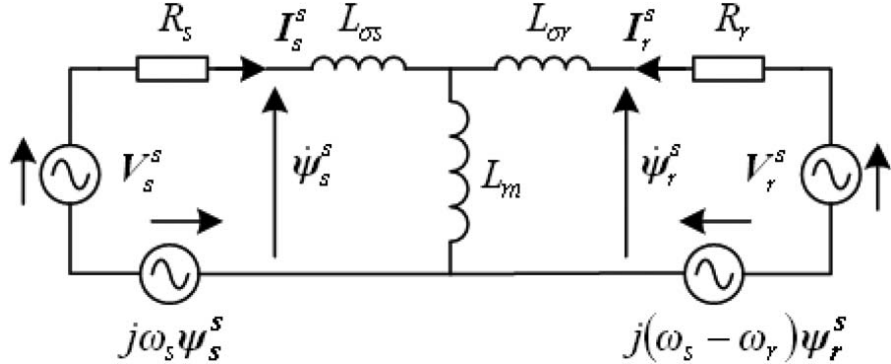


Fig.1.3 Electrical model of DFIG

The active and reactive power of stator could be calculated as follows:

$$P_s = \frac{3}{2} \frac{\omega_s}{L_s} \Psi_{sq} L_m I_{rd} \quad (1.1)$$

$$Q_s = \frac{3}{2} \frac{\omega_s}{L_s} \Psi_{sd} L_m I_{rq} \quad (1.2)$$

The equations (1.1), and (1.2) show that the output power of the system is dependent on the output of the rotor-side converter.

In normal operation mode where the supply voltage is balanced and the wind speed is at operational level, in order to have maximum power point tracking (MPPT) the reference power would be selected from power generation chart, which could be different for each generator based on ratings, mechanical considerations and other issues. Also the reactive power could be controlled as well. In most designs the reference reactive power would be set to zero, however, DFIG has the ability to contribute to reactive power production as well as active power. Once the reference active and reactive power is selected, one of many available control methods can be employed to achieve the reference values. Fig.1.4 shows a typical generation graph based on maximum power point tracking. It can be seen that for the wind turbine depicted here, above 12m/s wind speed, the shaft speed can be adjusted between 1pu and 1.2pu while the generated power is equal to the nominal value of the generator. So, for any wind speed the pitch angle should be adjusted to keep the mechanical shaft speed always less than 1.2pu. Also, in order to have maximum power point tracking the operating

point is to be found as mutual points between the MPPT curve (dashed red line) and the corresponding wind speed.

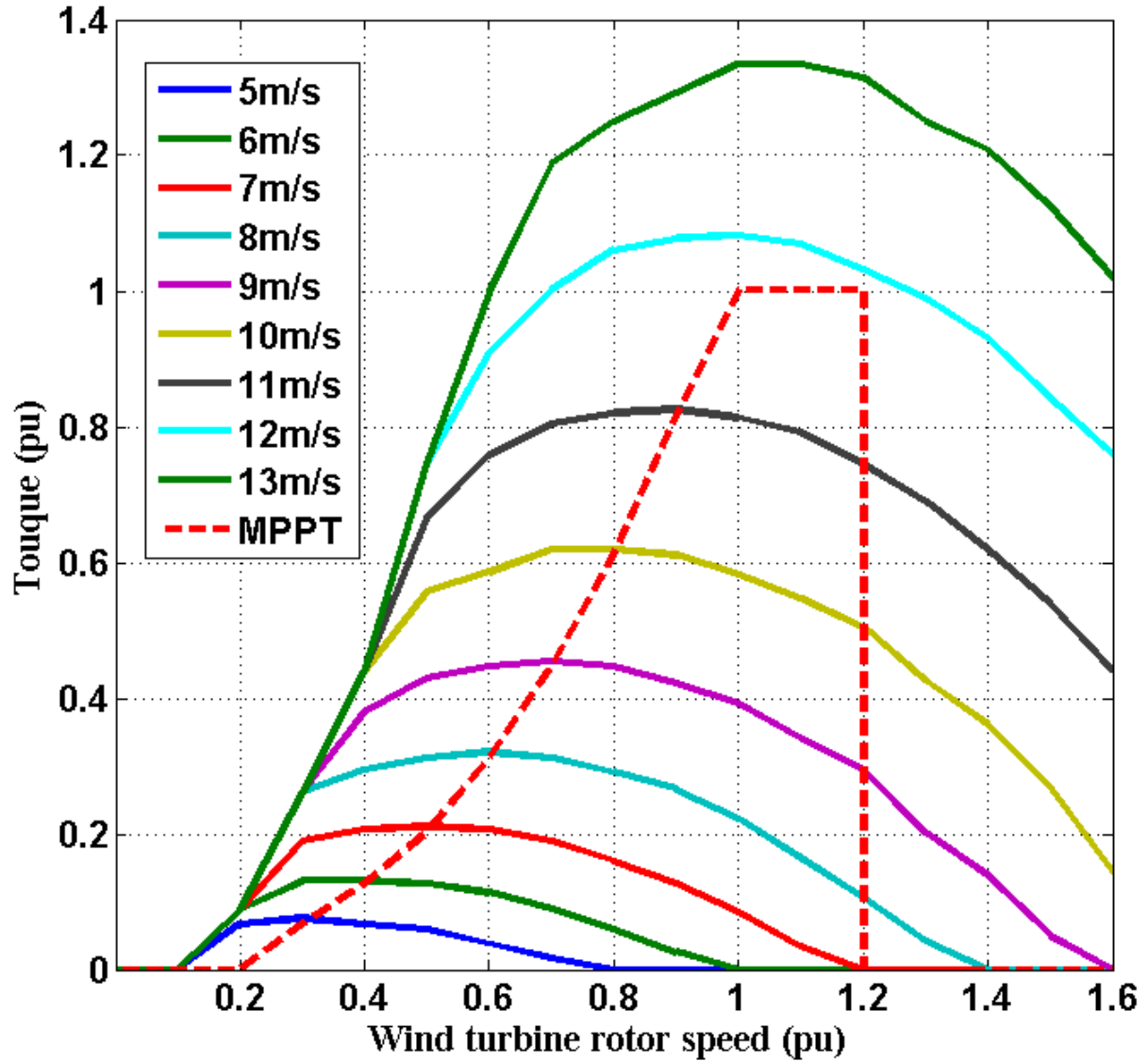


Fig.1.4 Wind power generation for maximum power tracking

1.4. Literature review

When the doubly fed generation method were introduced and implemented for reluctance machines (Brune et al., 1994, Liao and Sun, 1994, Tang and Xu, 1995) the idea led to early attempts of using wound rotor induction machines for such applications. The first implementation of DFIG is recorded in (Pena et al., 1996) where, the control strategy is based on PI controllers in conjunction with sinusoidal PWM that ends up with a constant switching frequency. The work is followed by more researches in control method. The detailed model based studies on DFIG are presented in (Cárdenas et

al., 2005) where the rotor position would be found through current and voltage models. Another important modelling research reported in (Petersson et al., 2005) where grid integration of DFIG and its operation under voltage sag is studied. Further studies on transient analysis of doubly fed induction generators followed in (Ledesma and Usaola, 2005). Implementation of current controlled methods on DFIG using hysteresis controller to achieve better dynamics was reported in (Chowdhury and Chellapilla, 2006).

In doubly-fed configuration two back-to-back connected converters provide the required magnetization current at rotor windings. In fact three phase power supply or grid connection to a three phase converter provides a stable DC voltage. This converter is usually called grid side converter (GSC). The DC voltage can be used for another voltage source three phase converter which is directly connected to terminals of rotor winding called rotor side converter (RSC). RSC normally has the same configuration and component as the GSC, the only difference is in the software program for the RSC.

Although, the main task of grid side converter (GSC) is to keep the dc bus voltage constant, GSC may also be used to compensate reactive power or in some cases to remove reactive power pulsation during unbalanced condition (Xu, 2008b). The RSC would provide the required magnetization current waveforms in rotor windings to generate required active and reactive power at stator terminals. However, as electrical torque is related to active power it is also reported in literature that in some control methods (Seman et al., 2006) the active and reactive reference values has been substituted with electrical torque and stator flux reference values.

To study the DFIG, RSC and GSC might be studied separately. In practice, as long as a stable dc bus voltage is provided by GSC, the RSC can operate totally isolated from the GSC. References (Mesbah et al., 2011) provide a GSC that is able to control DC even in unbalanced grid voltage source condition. However, the solution lacks the reactive power compensation. Also, in most methods RSC operates totally isolated from the GSC and a different controller would handle the operation of each converter. On the other hand, to deal with the active power pulsations in unbalance grid voltage there is a control method reported in literature that consider both converters (Xu, 2008a) in one control loop. Thus, the set points of GSC would be derived out of the RSC setpoints and turbine generator operating condition.

The need to improve the machine performance to meet the new grid codes for fault ride through performance led to more studies (Xiang et al., 2006, Jesús López, 2007). Some control methods have been proposed to improve fault ride capability of wind turbine generators and achieve better performance are also reported in literature such as Direct active control method (Xu and Cartwright, 2006), model based studies (Luna et al., 2011, Hu et al., 2011), PDPC (Zhi et al., 2010, Filho et al., 2011), Predictive DTC (Abad et al., 2008), Vector-Based Hysteresis (Mohseni et al., 2011b, Mohseni and Islam, 2010), and IVS-DTC(Chen et al., 2011) . Moreover, sensorless methods (Marques et al.,

2011, Mwinyiwiwa et al., 2009, Shen et al., 2009, Forchetti et al., 2009, Qiao et al., 2008) to have a more reliable, noise immune and less expensive system are also reported by previous researchers. A comparative study for some basic control approaches has been performed in (Tremblay et al., 2011).

Recently, studies in this area are mostly focused on new control strategies to improve the performance of DFIG and also fault ride through improvement (Meegahapola et al., 2010, Li and Zhang, 2010, Pannell et al., 2010, Rahimi and Parniani, 2010, Wang and Xu, 2010) which is a key concern for DFIG. For this reason, study of DFIG through practical implementation would help to justify various methods and ideas. Even though, practical results in previous researches have been offered including some useful hints for hardware setup, there is not enough detailed design are documented in literature.

1.5. Conclusions

Varieties of control methods are available to operate DFIG. Lots of these methods are developed to be suitable for unbalanced voltage conditions. Nevertheless, due to requirements of fault ride through and vulnerability of DFIG to voltage sags, new control methods have been developed to satisfy the new grid codes (Mohseni et al., 2011a). The simulations as well as practical implementation of the control methods would validate the methods to be used for wind power generation and also be capable of handling the faulty voltage conditions safely.

1.6. References

- ABAD, G., RODRÍGUEZ, M. Á. & POZA, J. (2008) Two-Level VSC Based Predictive Direct Torque Control of the Doubly Fed Induction Machine With Reduced Torque and Flux Ripples at Low Constant Switching Frequency. *IEEE Trans. on Power Electron.*, 23, NO. 3, 1050-1061.
- BOGALECKA E., A. K. M. (2008) Control of Reactive Power in Double-Fed Machine Based Wind Park. *Power Electronics and Motion Control Conference, EPE-PEMC 13th.*
- BRUNE, C. S., SPEE, R. & WALLACE, A. K. (1994) Experimental Evaluation of a Variable-Speed, Doubly-Fed Wind-Power Generation System. *IEEE Trans. on Ind. Applications*, 30, 648-655.
- CÁRDENAS, R., PEÑA, R., PROBOSTE, J., ASHER, G. & CLARE, J. (2005) MRAS Observer for Sensorless Control of Standalone Doubly Fed Induction Generators. *IEEE Trans. on Energy Conversion*, 20, NO. 4, 710-718.
- CHEN, S. Z., CHEUNG, N. C., WONG, K. C. & WU, J. (2011) Integral variable structure direct torque control of doubly fed induction generator. *IET Renew. Power Gener.*, 5, 18-25.
- CHOWDHURY, B. H. & CHELLAPILLA, S. (2006) Double-fed induction generator control for variable speed wind power generation. *Electric Power Systems Research*, 76, 786-800.
- FILHO, A. J. S., FILHO, M. E. D. O. & FILHO, E. R. (2011) A Predictive Power Control for Wind Energy. *IEEE Trans. on Sust. Energy*. , 2, NO. 1, 97-105.
- FORCHETTI, D. G., GARCÍA, G. O. & VALLA, M. I. (2009) Adaptive Observer for Sensorless Control of Stand-Alone Doubly Fed Induction Generator. *IEEE TRANSACTIONS ON INDUSTRIAL ELECTRONICS*, 56, NO. 10, 4174-4180.

- HANSEN, L. H., MADSEN, P. H., BLAABJERG, F., CHRISTENSEN, H. C., LINDHARD, U. & ESKILDSEN, K. (2001) Generators and power electronics technology for wind turbines. *IECON '01. The 27th Annual Conference of the IEEE*, 3, 2000 - 2005.
- HU, J., NIAN, H., XU, H. & HE, Y. (2011) Dynamic Modeling and Improved Control of DFIG Under Distorted Grid Voltage Conditions. *IEEE trans. on Energy Conversion*, 26, NO. 1, 163-175.
- JESÚS LÓPEZ, P. S., XAVIER ROBOAM, AND LUIS MARROYO (2007) Dynamic Behavior of the Doubly Fed Induction Generator During Three-Phase Voltage Dips. *IEEE Trans. on Energy Conversion*, 22, NO. 3, 709-717.
- LEDESMA, P. & USAOLA, J. (2005) Doubly Fed Induction Generator Model for Transient Stability Analysis. *IEEE Trans. on Energy Conversion*, 20, No. 2, 388-397.
- LI, D. & ZHANG, H. (2010) A combined protection and control strategy to enhance the LVRT capability of a wind turbine driven by DFIG. *IEEE International Symposium on Power Electronics for Distributed Generation Systems*.
- LIAO, L. & SUN, C. (1994) A Novel Position Sensorless Control Scheme for Doubly Fed Reluctance Motor Drives. *IEEE Trans. on Ind. Applications*, 30 No.5, 1210 - 1218
- LUNA, A., LIMA, F. K. D. A., SANTOS, D., RODRÍGUEZ, P., WATANABE, E. H. & ARNALTES, S. (2011) Simplified Modeling of a DFIG for Transient Studies in Wind Power Applications. *IEEE Trans. on Ind. Electron.*, 58, NO. 1.
- MARQUES, G. D., PIRES, V. F. A., SOUSA, S. E. & SOUSA, D. M. (2011) A DFIG Sensorless Rotor-Position Detector Based on a Hysteresis Controller. *IEEE Trans. on Energy Conversion*, 26, NO. 1, 9-17.
- MEEGAHAPOLA, L. G., LITTLER, T. & FLYNN, D. (2010) Decoupled-DFIG Fault Ride-Through Strategy for Enhanced Stability Performance During Grid Faults. *IEEE Trans. on sustainable Energy*, 1, NO. 3, 152-162.
- MESBAH, M., ISLAM, S. & MASOUM, M. A. S. (2011) A novel direct active power control method for DFIG wind turbine applications *IEEE PES ISGT*. USA.
- MOHSENI, M. & ISLAM, S. (2010) A New Vector-Based Hysteresis Current Control Scheme for Three-Phase PWM Voltage-Source Inverters. *IEEE Trans. On Power Electronics*, 25, no. 9, 2299-2309.
- MOHSENI, M., ISLAM, S. M. & MASOUM, M. A. S. (2011a) Enhanced Hysteresis-Based Current Regulators in Vector Control of DFIG Wind Turbines *IEEE Transactions on Power Electronics*, 26, no.1, 223-234.
- MOHSENI, M., MESBAH, M., ISLAM, S. & M.A.S. MASOUM (2011b) Vector-Based Hysteresis Current Regulator for DFIG Wind Turbines under Non-Ideal Supply Conditions. *Australian Journal of Electrical and Electronic Engineering (AJEEE)*, 8 , No.1 27-38.
- MWINYIWIWA, B., ZHANG, Y., SHEN, B. & OOI, B.-T. (2009) Rotor Position Phase-Locked Loop for Decoupled P-Q Control of DFIG for Wind Power Generation. *IEEE Trans. on Energy Conversion*, 24, NO. 3, 758-765.
- PANNELL, G., ATKINSON, D. J. & ZAHAWI, B. (2010) Minimum-Threshold Crowbar for a Fault-Ride-Through Grid-Code-Compliant DFIG Wind Turbine. *IEEE Trans. on Energy Conversion*, 25, NO. 3, 750-759.
- PENA, R., J.C.CLARE & ASHER, G. M. (1996) Doubly fed induction generator using back-to-back PWM converters and its application to variable-speed wind-energy generation. *IEE Proc.-Electr. Power Appl.*, 143, No.3, 231-241.
- PETERSSON, A., THIRINGER, T. O., HARNEFORS, L. & PETRU°, T. A. (2005) Modeling and Experimental Verification of Grid Interaction of a DFIG Wind Turbine. *IEEE Trans. on Energy Conversion*, 20, NO. 4, 878-886.
- QIAO, W., ZHOU, W., ALLER, J. M. & HARLEY, R. G. (2008) Wind Speed Estimation Based Sensorless Output Maximization Control for a Wind Turbine Driving a DFIG. *IEEE TRANSACTIONS ON POWER ELECTRONICS*, 23, NO. 3, 1156-1169.

- RAHIMI, M. & PARNIANI, M. (2010) Coordinated Control Approaches for Low-Voltage Ride-Through Enhancement in Wind Turbines With Doubly Fed Induction Generators. *IEEE Trans. on Energy Conversion*, 25, NO. 3, 873-883.
- SEMAN, S., NIIRANEN, J. & ARKKIO, A. (2006) Ride-Through Analysis of Doubly Fed Induction Wind-Power Generator Under Unsymmetrical Network Disturbance. *IEEE TRANSACTIONS ON POWER SYSTEMS*, 21, NO. 4, 1782-1789.
- SHEN, B., MWINYIWIWA, B., ZHANG, Y. & OOI, B.-T. (2009) Sensorless Maximum Power Point Tracking of Wind by DFIG Using Rotor Position Phase Lock Loop (PLL). *IEEE Trans. on Power Electron.*, 24, NO. 4, 942-951.
- TANG, Y. & XU, L. (1995) Vector Control and Fuzzy Logic Control of Doubly Fed Variable Speed Drives with DSP Implementation. *IEEE Transactions on Energy Conversion* 10, 661-668.
- TREMBLAY, E., ATAYDE, S. & CHANDRA, A. (2011) Comparative study of control strategies for the Doubly Fed Induction Generator in Wind Energy Conversion Systems: a DSP-based implementation approach. *IEEE Transactions on Sustainable Energy, early access*.
- WANG, Y. & XU, L. (2010) Coordinated Control of DFIG and FSIG-Based Wind Farms Under Unbalanced Grid Conditions. *IEEE Trans. on Power Delivery*, 25, No. 1, 367-377.
- XIANG, D., RAN, L., TAVNER, P. J. & YANG, S. (2006) Control of a Doubly Fed Induction Generator in a Wind Turbine During Grid Fault Ride-Through. *IEEE Trans. on Energy Conversion*, 21, NO. 3, 652-662.
- XU, L. (2008a) Coordinated Control of DFIG's Rotor and Grid Side Converters During Network Unbalance. *IEEE TRANSACTIONS ON POWER ELECTRONICS*, 23, NO. 3, 1041-1049.
- XU, L. (2008b) Enhanced Control and Operation of DFIG-Based Wind Farms During Network Unbalance. *IEEE TRANSACTIONS ON ENERGY CONVERSION*, 23, NO. 4, 1073-1081.
- XU, L. & CARTWRIGHT, P. (2006) Direct Active and Reactive Power Control of DFIG for Wind Energy Generation. *IEEE trans. on Energy Conversion*, 21, NO. 3, 750-758.
- ZHI, D., XU, L. & WILLIAMS, B. W. (2010) Model-Based Predictive Direct Power Control of Doubly Fed Induction Generators. *IEEE Trans. on Power Electron.*, 25, NO. 2, 341-351.

Chapter 2

Grid Side Converter (GSC)

2.1. Introduction

In DFIG, the primary role of the grid-side converter is to keep the dc-link voltage fixed. The power flow in rotor side converter is bidirectional and it must be supplied with the required power from DC link capacitor bank. As a result, to have a fixed DC bus voltage, the grid-side converter must be capable to supply a bidirectional power flow.

Fig 2.1.1 shows a typical GSC. The converter presented here is a three phase full bridge rectifier consisting of six switches.

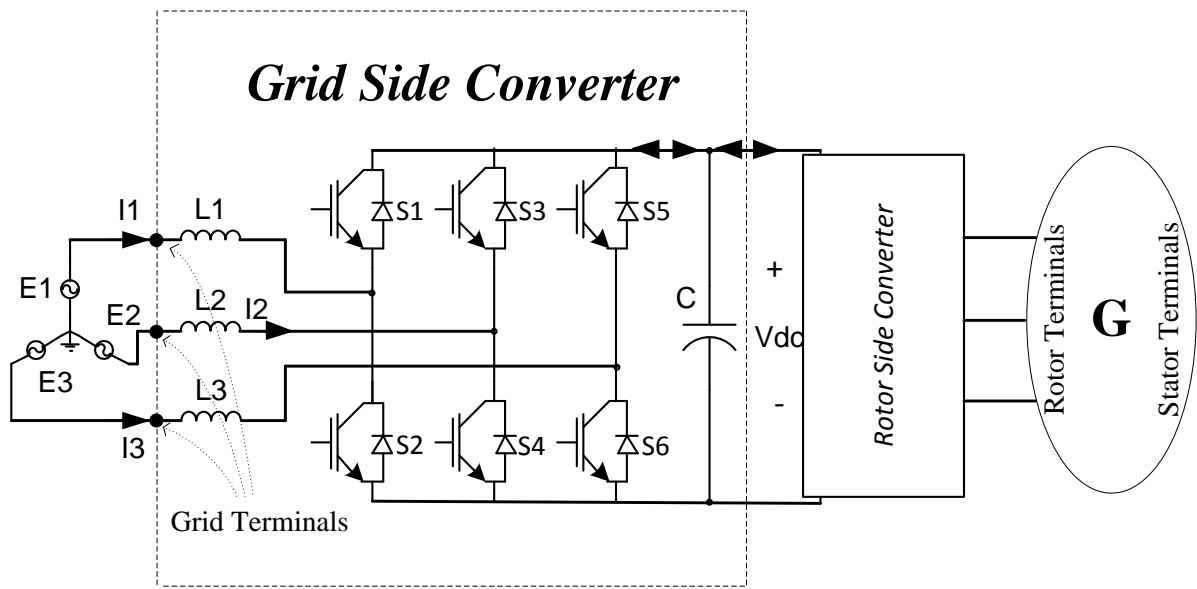


Fig 2.1.1. A Typical Grid Side Converter

There are three main approaches for three-phase power conversion; voltage vector control using space vector modulation (SVM), current control (CC), and direct power control (DPC).

For many years, voltage vector based control approaches using SVM (Broeck et al., 1988, Bowes and Mount, 1981, Youm and Kwon, 1999) have been utilized for three-phase power converters. These methods require few data samples, ensure smooth operation of the rectifier, and can be easily implemented using the older generations of digital signal processors (DSPs) or microcontrollers. However, they usually have slow transient responses to step current changes and high frequency reference current demands as the current regulator must filter the current signal to take out the fundamental component before applying it to a PI controller. In addition, the PI controller itself may also introduce undesired lag times in output response signals.

The conventional (Brod and Novotny, 1985) or vector based (Pan and Chang, 1994, Ambrožič et al., 2003) Current Control (CC) approaches normally use the actual current signal without filtering the switching related frequencies. Normally, these methods provide the reference current value in one switching cycle. However, the undesired variation in the switching frequency complicates the input filter design and increases the noise and power losses. Another practical issue, electromagnetic noise immunity, is a drawback for this method. The high frequency current signals are more vulnerable to high frequency noise generated by the electromagnetic interference that might be caused by input inductors, high frequency operated microcontrollers, and/or the neighbouring devices such as telecommunication systems and equipment. As a result, more components and considerations in the controller board design must be taken into account with the CC methods.

The Direct Power Control (DPC) based methods (Ohnishi, 1991, Hansen et al., 2000) use the reference voltage or virtual flux vectors (Malinowski et al., 2001) to generate the switching signals. However, they also suffer from the consequences associated with variable switching frequencies and require accurate and high resolution sampled signals. Reference (Malinowski et al., 2004) proposes a DPC-SVM rectification approach with constant switching frequency using PI controllers. Unfortunately, as with most SVM based approaches the DPC-SVM also has a relatively slow transient response.

Predictive solutions offer advantages like fast transient response and constant switching frequency. Some authors (Bouafia et al., 2010) has recently introduced a Predictive Direct Power Control (P-DPC) solution using SVM with a constant switching frequency pattern. In P-DPC, the converter shows fine dynamic performance similar to the CCs. The predictive method mathematically analyses the circuit and predicts which reference voltage vector can provide the desired power at the next switching cycle. However, the operation of the circuit and the quality of solution will strongly depend on the selected predictive approach and rules, as well as the correct estimation of parameters. Clearly, due to the system inefficiencies the controller output active and reactive powers will have deviations from the reference values that need to be compensated in the next switching cycle. The same scenario may occur in the next switching cycle resulting in oscillations and sub-harmonics at the circuit output terminals and preventing smooth operation of the rectifier.

To overcome the associated problems with existing control approaches, in this thesis a new method has been developed and would constitute as one of author's contribution.

2.2. Direct Active Power Control (Mesbah et al., 2011a)

2.2.1. Direct Active Power Control Principles

The ideal structure of the new ac-dc rectification method is shown in Fig 2.2.1. The output power depends on the output voltage and converter output current

$$P_c = V_{dc} I_{dc} \quad (2.2.1)$$

Where P_c is the converter's power, V_{dc} is the dc output voltage, and I_c is the converter instantaneous output current.

Although the ideal output current is a pure dc waveform, it is not possible to have a pure dc output current due to the sinusoidal nature of the source current and presence of the six switches. Therefore, the output current is a series of pulses and the only way to achieve constant power is to have a stable average output dc current.

Obviously the best solution is to have the average converter output current (I_{avg}) in each switching period (T_s) equal to the reference current (I_{ref}):

$$I_{ref} = I_{avg} = \frac{1}{T_s} \int_0^{T_s} I_c dt \quad (2.2.2)$$

There are eight possible operating modes and the corresponding output currents are listed in Table 2.2.1. The upper arm and lower arm switches in each phase work in opposite states. The output current is equal to zero during two switching states when all upper arm switches are simultaneously switched on or switched off.

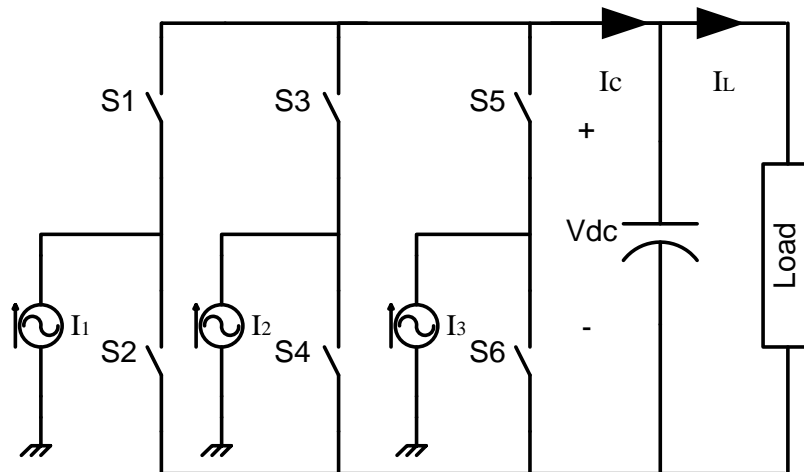


Fig 2.2.1. Ideal structure of the new ac-dc rectification method

In order to produce reference average current at dc-side, demanded dc current, shall be provided using proper switching states. Also, In order to have a smooth switching pattern the switching states shall be only 60 degrees apart during a whole 50 Hz power cycle. Selecting the two largest possible currents (as shown in Fig 2.2.2 as I_x and I_y) in the direction of reference current provides the above considerations.

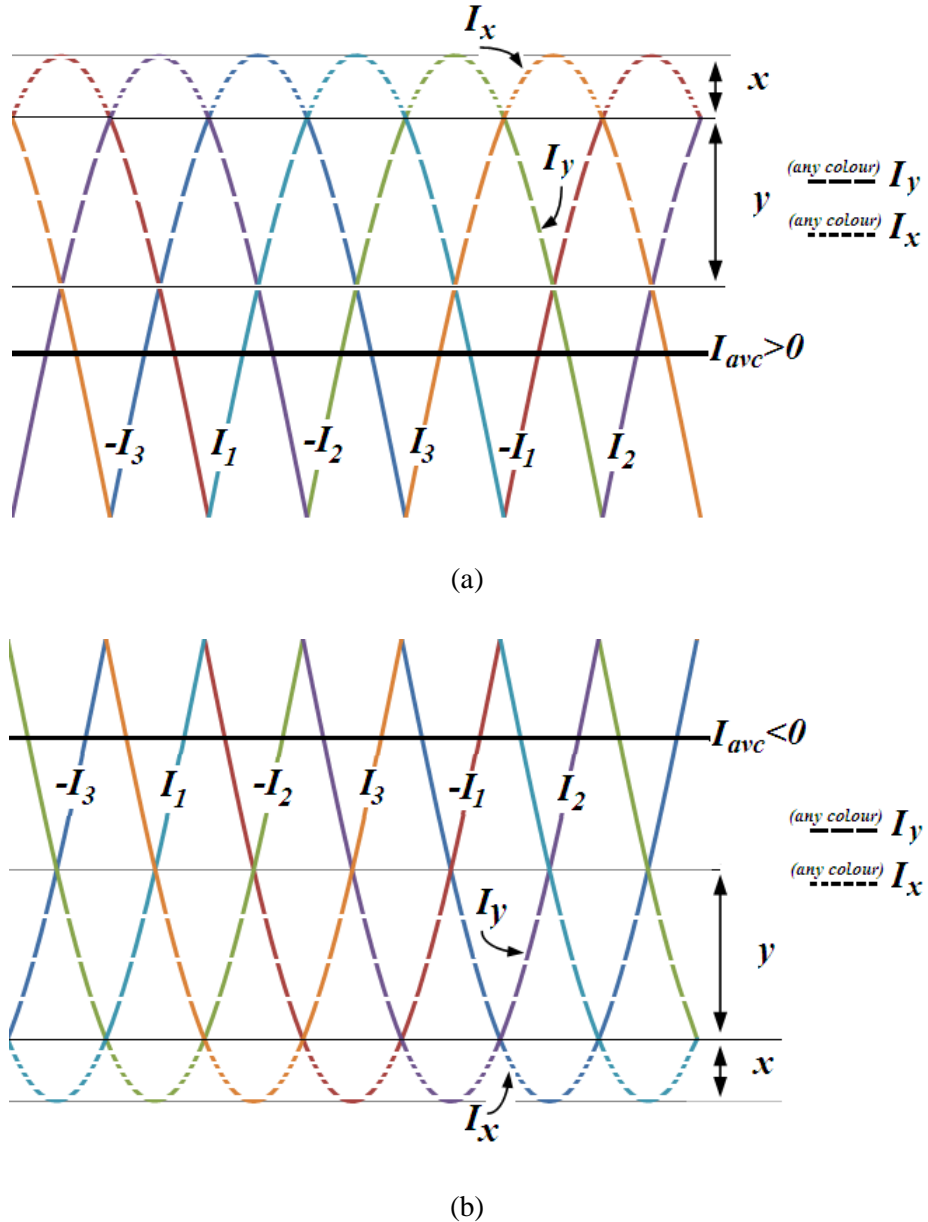


Fig 2.2.2. Selection of I_x and I_y (a) $I_{avec} > 0$ (b) $I_{avec} < 0$

Therefore, for a constant switching frequency with proper selection of duty cycle for each switching cycle any reference current value in range of $(\pm\sqrt{3}I_{max}/2)$ can be easily generated. In Fig 2.2.2 (a)

while the demanded dc current is greater than zero, and Fig 2.2.2 (b) while the demanded dc current is less than zero, the I_y and the I_x currents are shown with dashed lines respectively.

TABLE 2.2.1- Operational modes the proposed ac-dc current converter

Resulting Voltage Vector Type	Operation Mode	Output Current (\mathbf{I}_C)	State of Switches		
			S_1	S_3	S_5
Active Vectors	1	\mathbf{I}_1	1	0	0
	2	$\mathbf{I}_1 + \mathbf{I}_2 = -\mathbf{I}_3$	1	1	0
	3	\mathbf{I}_2	0	1	0
	4	$\mathbf{I}_2 + \mathbf{I}_3 = -\mathbf{I}_1$	0	1	1
	5	\mathbf{I}_3	0	0	1
	6	$\mathbf{I}_1 + \mathbf{I}_3 = -\mathbf{I}_2$	1	0	1
Null Vectors	7	$\mathbf{I}_1 + \mathbf{I}_2 + \mathbf{I}_3 = 0$	1	1	1
	8	0	0	0	0

If phase currents are considered constant in each switching period, the reference converter output current will be:

$$I_{avc}^* = D_x I_x + D_y I_y + D_z I_z \quad (2.2.3)$$

where, D_x , D_y and D_z are the duty cycles for I_x , I_y and I_z , respectively, and I_z occurs when all of the upper switches are simultaneously switched on or switched off. As $I_z=0$, then:

$$I_{avc}^* = D_x I_x + D_y I_y \quad (2.2.4)$$

Current Source Implementation

The easiest way to have a current source is to add large impedance in series with a voltage source. Furthermore, in order to have low power dissipation, an inductor should be selected as the series impedance. Very large values of the inductor results in low current values and no dc power transmission. Small inductor values will generate current harmonics due to the switching action and will be avoided in the proposed algorithm. The resulted converter is shown in Fig 2.2.3. Which resembles a conventional converter and the only physical difference is the magnitude of inductor.

Considering the converter generates no reactive power at ac side (which there is no need for reactive power generation when the power supply is current source) the converter model could be simplified to three resistors at ac-side as is shown in Fig 2.2.4.

In order to calculate the inductor value we should consider that reactive power is always greater than active power (i.e., power factor should always be less than $\sqrt{2}/2$). Therefore, to design a typical circuit, the nominal power should be considered as the maximum power which means the output

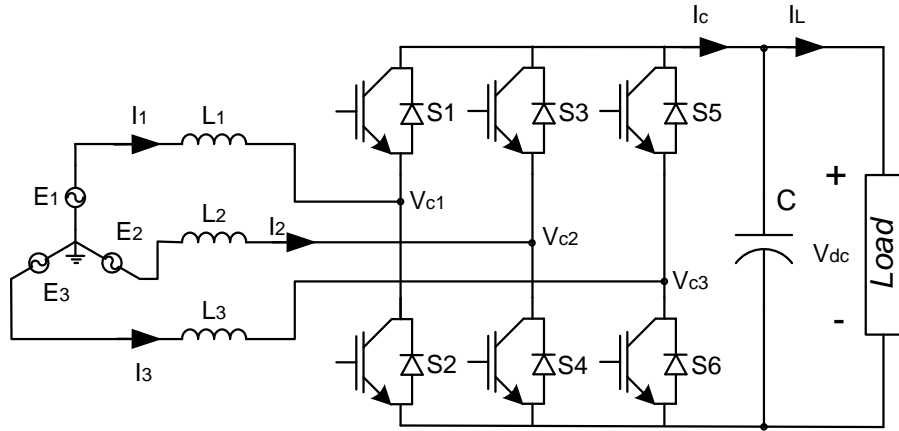


Fig 2.2.3. Schematic for proposed DAPC method

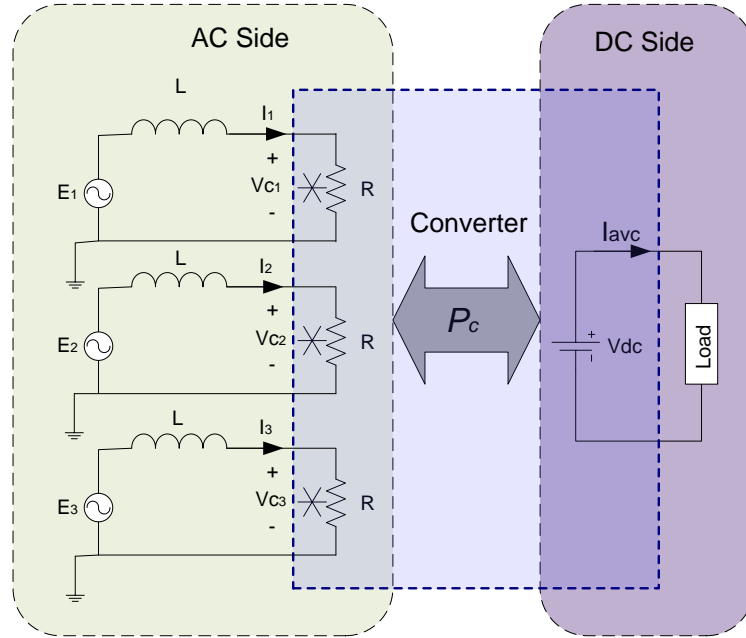


Fig 2.2.4. Equivalent circuit of the proposed converter

power will have a maximum value when the reactive power is at minimum. From definition of active and reactive power:

$$P_{c\max} = S(PF_m) \quad (2.2.5)$$

And,

$$Q_{min} = S \sqrt{1 - PF_m^2} \quad (2.2.6)$$

where, PF_m is the power factor under maximum output power condition, P_{cmax} and Q_{min} are the converter maximum active and minimum reactive power, respectively, and S is the apparent power.

Considering (2.2.5) and (2.2.6):

$$Q_{min} = \frac{\sqrt{1 - PF_m^2}}{PF_m} P_{cmax} \quad (2.2.7)$$

Also, PF_m can be calculated as follows:

$$PF_m = \frac{R}{\sqrt{R^2 + X^2}} \quad (2.2.8)$$

where, R and X are the resistive and the reactive components of load impedance, while maximum power is drawn at the dc side, respectively. Apparent power is the

$$S = \frac{3E^2}{\sqrt{R^2 + X^2}} \quad (2.2.9)$$

where, E is the RMS phase voltage of the supply.

The maximum possible reactive power (Q_{max}) will occur when there is no real power demand and its magnitude will be equal to the apparent power:

$$Q_{max} = \frac{3E^2}{X} \quad (2.2.10)$$

On the other hand, from (2.2.6), and (2.2.9):

$$Q_{min} = \frac{3E^2 X}{R^2 + X^2} = \frac{3E^2 \sqrt{1 - PF_m^2}}{\sqrt{R^2 + X^2}} \quad (2.2.11)$$

The maximum reactive power can also be calculated using Q_{min} . From (2.2.10) and (2.2.11):

$$Q_{max} = \frac{I}{I - PF_m^2} Q_{min} \quad (2.2.12)$$

Also, from (2.2.7) and (2.2.12):

$$Q_{max} = \frac{I}{PF_m \sqrt{1 - PF_m^2}} P_{cmax} \quad (2.2.13)$$

As the only consumers of reactive power are the three inductors and in this case the entire supply voltage drops across the inductors, the inductor value can be calculated as:

$$L = \frac{3E^2}{\omega Q_{max}} = \frac{3PF_m \sqrt{1 - PF_m^2} E^2}{\omega P_{cmax}} \quad (2.2.14)$$

where, ω is the source angular frequency (rad/s). Therefore, for given values of output power, power factor, supply voltage and frequency, the inductor value could be calculated.

Calculation of Duty Cycle

In order to calculate the correct values for the duty cycles for switching the generated active and reactive power play the key role.

As the converter structure has no difference to a three phase boost rectifier expect size of inductor, from (Malinowski et al., 2003) the driven active power for source is calculated as following:

$$P = P_L + P_c \quad (2.2.15)$$

$$P_L = L \left(\frac{dI_1}{dt} I_1 + \frac{dI_2}{dt} I_2 + \frac{dI_3}{dt} I_3 \right) \quad (2.2.16)$$

$$P_c = V_{dc} (S_1 I_1 + S_3 I_2 + S_5 I_3) \quad (2.2.17)$$

where, P is the Mains active power, P_L is the active power of inductors, P_c is the active power of converter, S_1 , S_3 , S_5 are switching signals for individual phases of the rectifier, I_1 , I_2 and I_3 are the three phase ac currents. As the inductor do not consume active power in steady state operation of converter, P_L is equal to zero. Reactive power also calculates by following formula (also deduced from (Malinowski et al., 2003)):

$$Q = Q_L + Q_c \quad (2.2.18)$$

$$Q_L = \frac{3L}{\sqrt{3}} \left(\frac{dI_1}{dt} I_3 - \frac{dI_3}{dt} I_1 \right) \quad (2.2.19)$$

$$Q_c = -V_{dc} (S_1 (I_3 - I_2) + S_3 (I_1 - I_3) + S_5 (I_2 - I_1)) \quad (2.2.20)$$

where, Q is the total reactive power Q_L is the inductor's reactive power and Q_c is the generated converter's reactive power.

Active power is the demanded power at dc-side; the converter should work like a resistor at ac-side, and the generated reactive power should be zero.

Considering $X \neq Y$ like X and Y axis which are shown in Fig 2.2.5. With a constant switching frequency, the D_x is the duty cycle for the time that only S_1 is turned on then from (2.2.20) converter's reactive power could be calculated as following:

$$Q_{cx} = -V_{dc}(I_3 - I_2) \quad (2.2.21)$$

where, Q_{cx} is the converter's reactive power during X switching period.

From Fig 2.2.5 we have $I_x = I_1$ and $I_y = -I_3$ then as a result:

$$Q_{cx} = -V_{dc}(-2I_y + I_x) \quad (2.2.22)$$

During Y switching condition, S_1 and S_3 are both turned on, and then the reactive power using the same approach is equal to:

$$Q_{cy} = -V_{dc}(-2I_x + I_y) \quad (2.2.23)$$

The total generated reactive power shall be equal to zero then

$$Q_c = Q_{cx}D_x + Q_{cy}D_y = 0 \quad (2.2.24)$$

So in order to calculate correct duty cycle from (2.2.4) & (2.2.24)

$$\begin{bmatrix} D_x \\ D_y \end{bmatrix} = \begin{bmatrix} I_x & I_y \\ -I_x + 2I_y & I_y - 2I_x \end{bmatrix}^{-1} \begin{bmatrix} I_{avc}^* \\ 0 \end{bmatrix} \quad (2.2.25)$$

Using the same calculation method if $X \neq Y$ then:

$$\begin{bmatrix} D_x \\ D_y \end{bmatrix} = \begin{bmatrix} I_x & I_y \\ I_x - 2I_y & -I_y + 2I_x \end{bmatrix}^{-1} \begin{bmatrix} I_{avc}^* \\ 0 \end{bmatrix} \quad (2.2.26)$$

Ac-side analysis

From the ac side of the converter, there will be an ac voltage generated at terminals of the full bridge during the switching conditions corresponding to the I_x and the I_y currents. As is shown in Fig.2.2.5 there is a 60° phase shift between voltage vectors during x and y switching states, the magnitude of the generated voltage can be calculated as:

$$|V_c| = \sqrt{(V_x + \frac{1}{2}V_y)^2 + (\frac{\sqrt{3}}{2}V_y)^2} \quad (2.2.27)$$

where, $|V_x| = 2D_x V_{dc}/3$, $|V_y| = 2 D_y V_{dc} / 3$ and V_c is the ac voltage of the converter.

From (2.2.4) and (2.2.27), we have

$$|V_c| = \frac{2}{3}V_{dc} \sqrt{\alpha^2 + (1-2\beta)\alpha D_y + (1-\beta+\beta^2)D_y^2} \quad (2.2.28)$$

where, $\alpha = \frac{I_{avg}^*}{I_x}$ and $\beta = \frac{I_y}{I_x}$.

As the converter neither generates nor consumes reactive power, the converter's ac current (i_c) is in the same phase as ac voltage of converter when $P_c > 0$ or the phase difference is 180° when $P_c < 0$ as is shown in Fig 2.2.5.

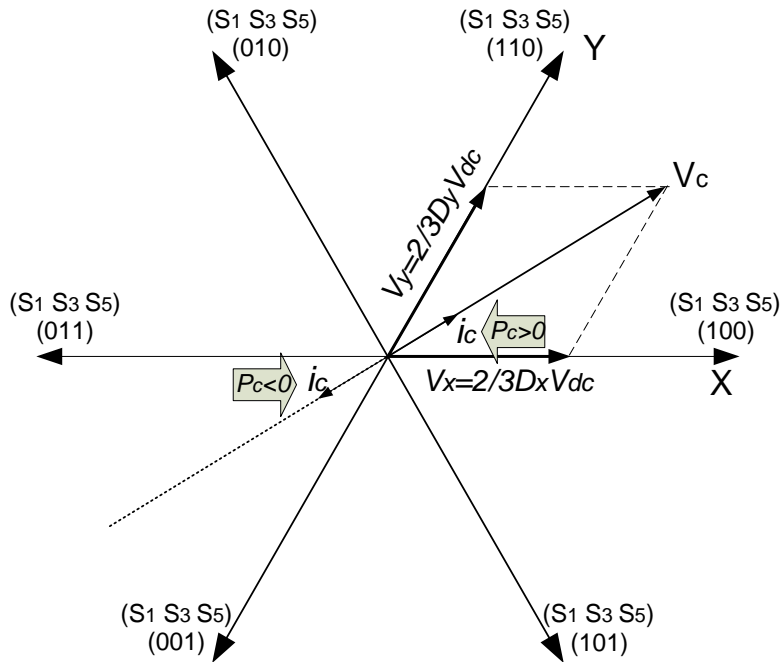


Fig 2.2.5. Current and voltage vector at ac-side

Output Voltage Selection

The output voltage depends on output dc current. It is possible to have a value between $\pm \frac{\sqrt{3}}{2} I_{max}$ for maximum output current, but selecting the largest possible values results in undesired operating conditions when the power supply is weak.

The output possible voltage range could be as follows:

$$\frac{2P_{cmax}}{\sqrt{3}I_{max}} \leq V_{dc} \leq \infty \quad (2.2.29)$$

Considering,

$$I_{max} = \sqrt{2}I_{rms} \quad (2.2.30)$$

where, I_{rms} is the RMS value of the line current, and

$$P_{cmax} = 3EI_{rms} PF_m \quad (2.2.31)$$

Then,

$$\sqrt{6}E PF_m \leq V_{dc} \leq \infty \quad (2.2.32)$$

Therefore, the output voltage can be higher or lower than the maximum voltage level of the power supply. In other words, the operation of the converter in either buck or boost mode is possible.

Output Capacitor Selection Criteria

The output capacitor should be large enough to maintain regulated output voltage for fast changes in power demand. In this part, design criteria are selected to maintain the output voltage around 2 percent of nominal dc voltage in one single switching cycle for the largest possible variations in demand power. Therefore, considering the largest power change as $2P_{max}$ (while the power changes from $-P_{cmax}$ to $+P_{cmax}$ or vice versa), then we have:

$$C \geq \frac{2 P_{cmax} T_s}{0.02 V_{dc}^2} \quad (2.2.33)$$

Equation (2.2.33) identifies dc capacitor values resulting in 2% voltage variation under all operating conditions.

DC Voltage Regulator

As the converter is fast enough to supply the load power demand in each switching cycle, it is recommended to use the filtered output load current as the feed forward parameter for the dc voltage

regulator, as shown in Fig 2.2.6. The low pass filter is to remove high frequency components of load current as the load may not be always a simple resistor. Therefore, with a nonlinear switching load, the low pass filter should be designed to remove the switching frequency components. The PI converter role is limited to steady state operation of converter and as a result the its output can be limited to smaller value to have a smooth start up.

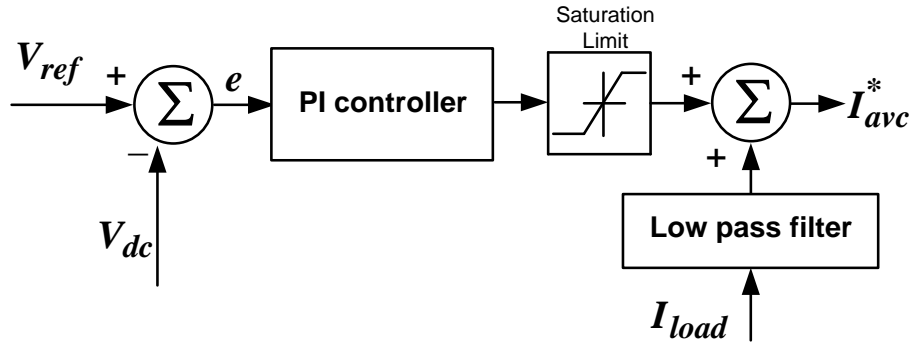


Fig 2.2.6. Control block diagram for the proposed approach

2.2.2. Application of AC-DC DAPC Converter in Wind Power Generation

Fig 2.2.7 shows the basic scheme of the doubly-fed induction generator used in wind power generation. There are a couple of reasons that make the proposed ac-dc current converter suitable for DFIG grid side rectification:

- The proposed converter requires reactive power that may be provided through extra capacitors at the ac side. However, in DFIG applications this compensation can be easily performed by the stator.
- The grid side converter in this application is mostly designed such that its maximum power rating is less than 30% of the generator power ratings. Assuming a power factor of 0.6 for the grid side converter, its reactive power will be around 40% of the generator power rating which can be easily compensated in stator side by controlling the q-axis current in rotor side converter. It means that in this application, there is no need to use extra capacitors to generate reactive power for the grid side converter.

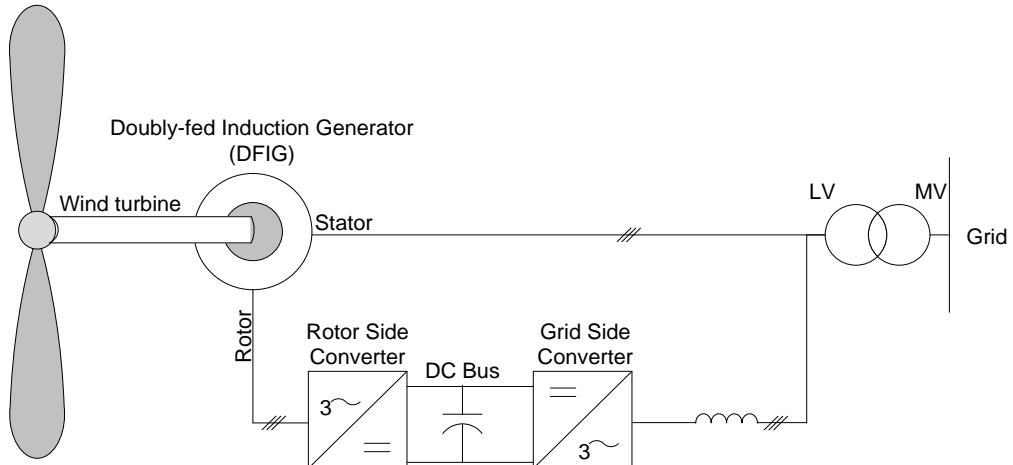


Fig 2.2.7. Schematic diagram of DFIG-based wind generation systems

- Also, As long as the reference current is less than I_x , it can be generated at output stage in a single switching period which results negligible dc-link voltage disturbance even with unbalanced three-phase source voltages. This characteristic is the unique feature of this approach.
- Considering buck operation mode, the bridge switches can operate at lower voltage levels. As the voltage ratings of industrial IGBTs are typically less than 6500V, application of MV motors in DFIG are usually subjected to some restrictions.

However, DFIGs in conjunction with the proposed converter can operate with IGBT modules in buck mode even for source voltages higher than 6500.

In addition, due to very fast traction of reference current, a small high voltage capacitor will be required and the combined system of DFIG and ac-dc current converter seems to be more very cost effective.

2.2.3. Simulation Results

Simulations are performed using MATLAB software to show the feasibility of the proposed approach as a power source converter. Three case studies are investigated including:

- Case A- Balance source voltages with a step change in the output power to show the inverter speed in supplying a variable dc load.
- Case B- Unbalance source voltages with a constant output power to demonstrate inverter ability in supplying the dc load (without any coordinated axis calculations) with no transient in the output voltage.

- Case C- Unbalance source voltages with a variable output power which has an offset and its frequency of variation is twice the line frequency.

Case C is very common in DFIG applications where both the source voltages and the rotor converter's current are unbalanced which results in a current waveform similar to this case study at the DC-side. Unlike the proposed converter, most conventional grid side converters cannot follow the reference current signal and result in some reference voltage deviations in dc bus.

The system is designed using typical parameters including: maximum power= 600KW, power factor= 0.6, $L=100\text{mH}$ (using equation (2.2.14)), $C=830\mu\text{F}$ (using equation (2.2.33)), input line voltage= 6600V, output voltage= 5000Vdc (which is in the range of (2.2.29) and ensures the operation in buck mode), switching frequency= 2 KHz.

Case A: Balance source voltages with constant output power

The output load is constant and suddenly changes from 200KW to -200KW at $t=0.3\text{sec}$. The output voltage is shown in Fig 2.2.8a with very small variations due to the fast compensated in about four switching cycle. The reason of this four cycle delay is mainly the low-pass filter's lag in control loop. In Fig 2.2.8b it can be seen that the load is fully supplied by the converter even during the transient time while there is a step change in demanded load. Fig 2.2.8c shows the three-phase currents and the reference or demanded converter's output current. There is a transient time associated with the ac current waveforms; however, it does not affect the dc output power. In fact, regardless of input current waveform the average output current is equal to the reference current. The THD of current waveform is 1.9% which is considerably small in compared with the conventional switching converters.

Case B: Unbalance source voltages with constant output power

In this case, a specific amount of unbalance is enforced on the source voltages while I_x is keep larger than I_{avg} to insure normal operating condition of the converter. At $t= 0.3\text{sec}$, the voltage magnitude of Phase A is reduced by 10%.

Fig 2.2.9a shows the output dc voltage indicating that the unbalanced voltage conditions have no effect on the output voltage.

The converter output and reference currents are shown in Fig 2.2.9b. It can be seen that the load is fully supplied by the converter. Fig 2.2.9c shows three-phase currents and the reference or demanded converter's output current.

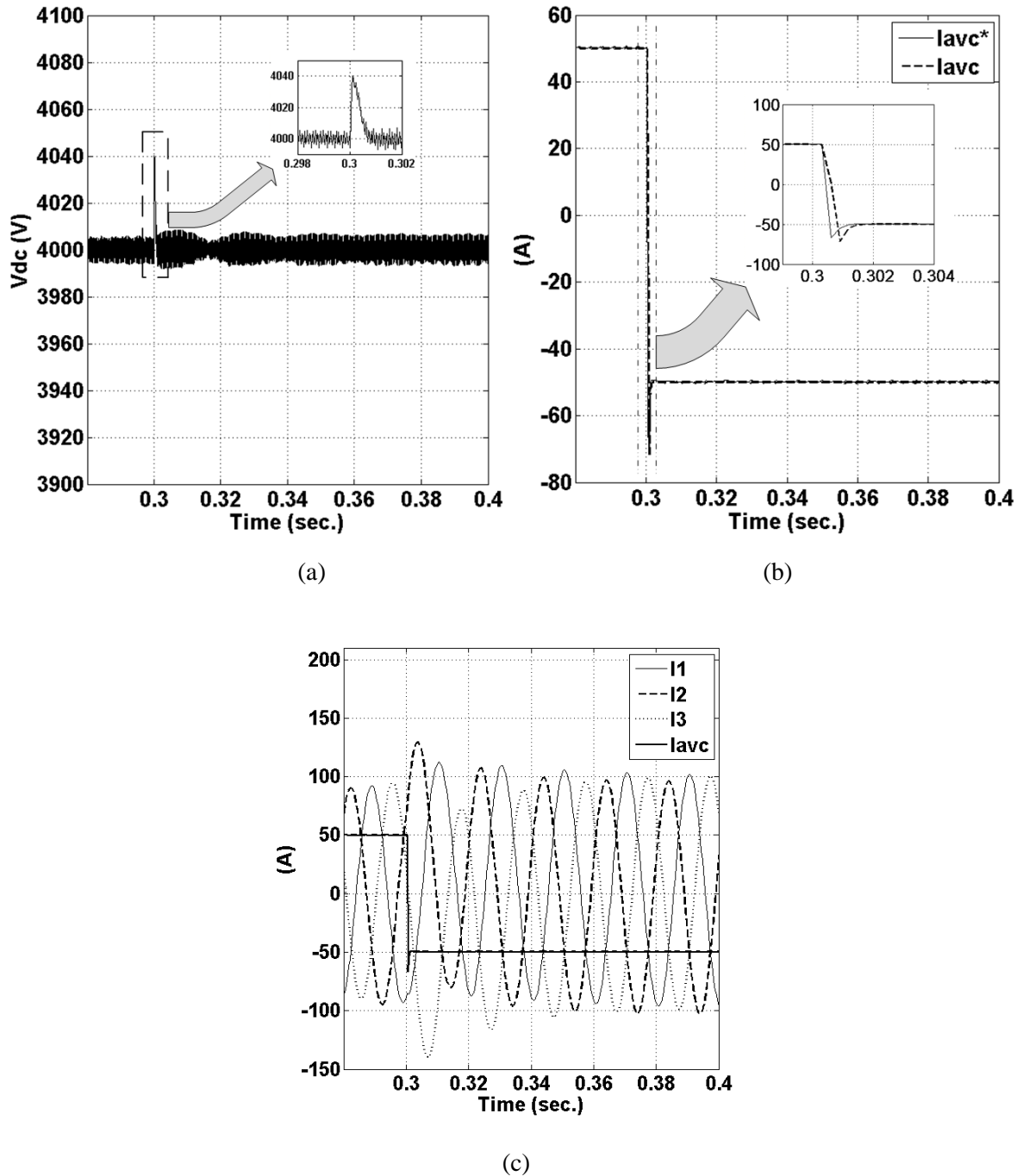
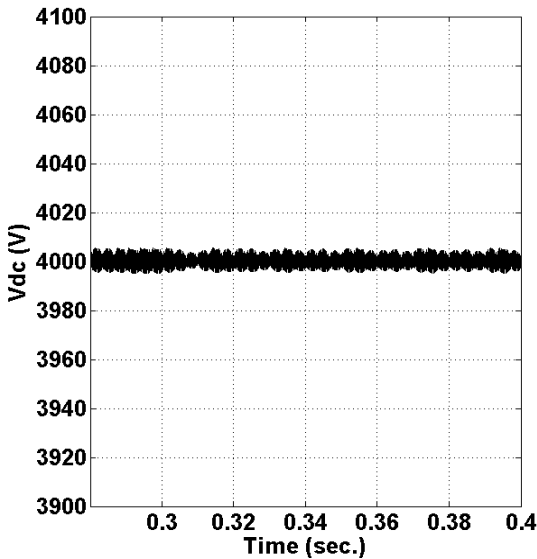
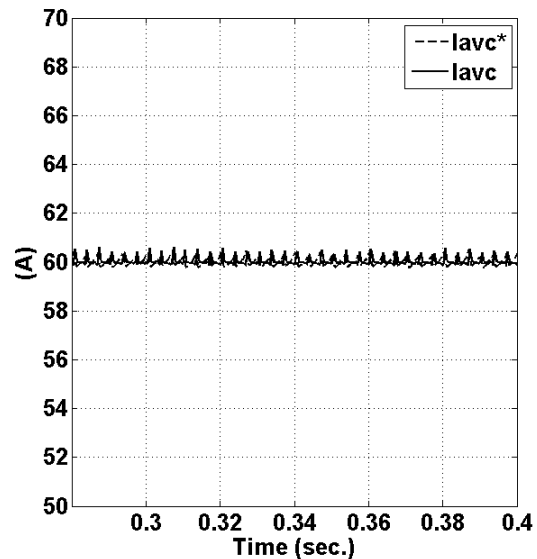


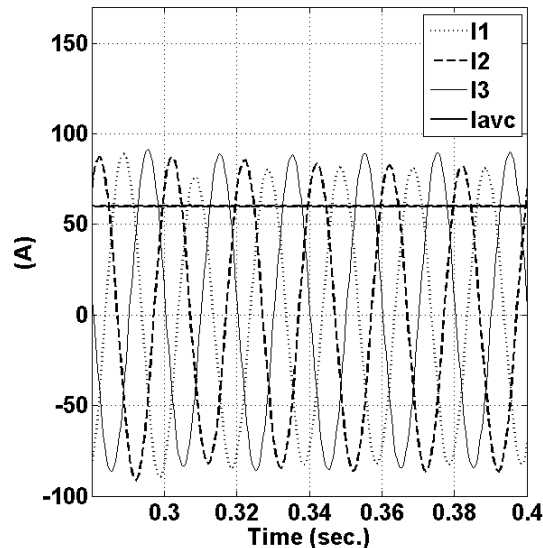
Fig 2.2.8. Simulation results for Case A; (a) output voltage (V), (b) converter output (I_{avc}) and reference (I_{avc}^*) currents (A), (c) three-phase currents and converter reference output current (A)



(a)



(b)



(c)

Fig 2.2.9. Simulation results for Case B; (a) output voltage (V), (b) converter output (I_{avc}) and reference (I_{avc}^*) currents (A), (c) three-phase currents and converter reference output current (A)

Case C: Unbalance source voltages with variable output power

The unbalanced source voltage conditions of Case B are considered and at $t=0.3$ sec, the output power is drawn with an ac frequency of 100 Hz. The average power is 120KW and varies between 0 and 240KW. Fig 2.2.10a, shows the effect of unbalanced source voltages and sinusoidal load on the output voltage. The average dc voltage does not vary; however, the voltage ripples become zero when the converter's current as well as the load current are zero. Then, as there is no input and output current to dc-bus capacitor, it is clear that the voltage ripples should be zero. The highest voltage

ripples for dc voltage appear when the load current reaches its maximum and the converter's current is also high.

Fig 2.2.10b shows the converter output power and the load power. Like Cases A and B, it can be seen that the load is fully supplied by the converter. Fig 2.2.10c shows the three-phase currents, as well as, the reference or demanded converter's output current.

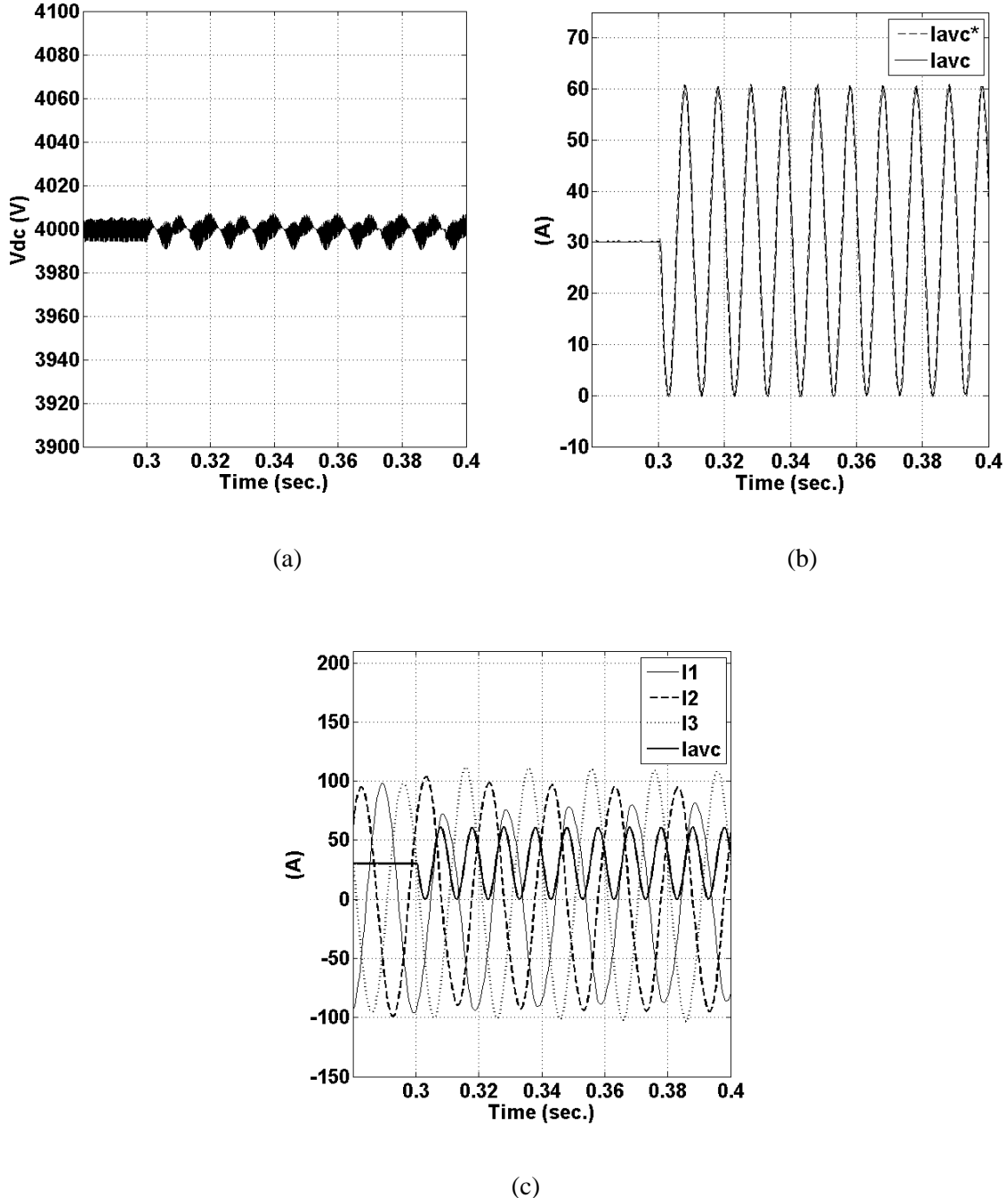


Fig 2.2.10. Simulation results for Case C; (a) output voltage (V), (b) converter output (I_{avc}) and reference (I_{avc}^*) currents (A), (c) three-phase currents and converter reference output current (A)

2.2.4. Conclusion

A new approach for three-phase rectification based on instantaneous dc-side current demand is proposed and simulated. The main features of the ac-dc current-based converter are:

- As the only measurements in the ac side are the three phase currents, the PLL circuit is eliminated, computation time is reduced and high sampling rates are not required.
- It has fast dynamic response and negligible transient distortions with balanced and unbalanced source voltages.
- High frequency current harmonics are minimal and there is no need for ferrite cores or high frequency inductors.
- The reference signal can be generated in a single switching cycle and there is negligible dc voltage disturbance.
- Unlike conventional ac-dc systems the output dc voltage can be higher or lower than the maximum value of input voltage.
- In the buck operating mode, smaller voltage rating of switches can be selected and high voltage supplies can operate with low voltage switches.

Simulations results are presented to highlight the unique features of this new approach which make it a viable solution for the grid side converter in doubly-fed induction generators for wind power applications.

2.3. Improved Predictive Direct Power Control (Mesbah et al., 2011b)

2.3.1. Principles of operation

The P-DPC rectification approach (Bouafia et al., 2010) offers the advantages of the conventional SVM, uses a constant switching frequency and provides single cycle response to support any load demand. This is very much desirable from the grid compatibility of DFIG point of view. The main disadvantage of this high performance power conversion technique is its dependency on the circuit parameters and requiring precisely timed and accurate measurements. Approximations may be made but approximations in mathematical model would degrade the operation of converter especially in high power applications with low switching frequencies.

In the stationary reference frame active (P) and reactive (Q) powers can be calculated using:

$$\begin{bmatrix} P \\ Q \end{bmatrix} = \begin{bmatrix} e_\alpha & e_\beta \\ -e_\beta & e_\alpha \end{bmatrix} \begin{bmatrix} i_\alpha \\ i_\beta \end{bmatrix} \quad (2.3.1)$$

where, P and Q are input active and reactive powers, e_α , e_β , i_α , and i_β are voltages and currents of the three-phase power supply in the stationary frame, respectively.

In (Bouafia et al., 2010) the variation of active and reactive powers using the above equation is presented by approximating the voltage to be constant at two successive switching states. This assumption is true in low voltage and low power applications. However, the assumption is not valid in high power applications where the switching frequency is low and the current is large. We may have a more accurate scenario by considering that the voltage slope is constant between two successive samples, then:

$$\begin{bmatrix} \Delta e_\alpha(k+1) \\ \Delta e_\beta(k+1) \end{bmatrix} = \begin{bmatrix} \Delta e_\alpha(k) \\ \Delta e_\beta(k) \end{bmatrix} = \begin{bmatrix} e_\alpha(k) - e_\alpha(k-1) \\ e_\beta(k) - e_\beta(k-1) \end{bmatrix} \quad (2.3.2)$$

where, $\Delta X(k)$ represents subtraction of kth sample of X from the previous sample, and k is the current sample. The difference of active and reactive powers between two successive sampling instants can be computed using the time domain derivative of (2.3.1):

$$\frac{d}{dt} \begin{bmatrix} P \\ Q \end{bmatrix} = \frac{d}{dt} \begin{bmatrix} e_\alpha & e_\beta \\ -e_\beta & e_\alpha \end{bmatrix} \times \begin{bmatrix} i_\alpha \\ i_\beta \end{bmatrix} + \begin{bmatrix} e_\alpha & e_\beta \\ -e_\beta & e_\alpha \end{bmatrix} \times \frac{d}{dt} \begin{bmatrix} i_\alpha \\ i_\beta \end{bmatrix} \quad (2.3.3)$$

Then by approximation we have:

$$\begin{aligned} \begin{bmatrix} \Delta P(k+1) \\ \Delta Q(k+1) \end{bmatrix} &= \begin{bmatrix} P(k+1) - P(k) \\ Q(k+1) - Q(k) \end{bmatrix} = \\ &\begin{bmatrix} \Delta e_\alpha(k) & \Delta e_\beta(k) \\ -\Delta e_\beta(k) & \Delta e_\alpha(k) \end{bmatrix} \begin{bmatrix} i_\alpha(k) \\ i_\beta(k) \end{bmatrix} + \begin{bmatrix} e_\alpha(k) & e_\beta(k) \\ -e_\beta(k) & e_\alpha(k) \end{bmatrix} \begin{bmatrix} \Delta i_\alpha(k+1) \\ \Delta i_\beta(k+1) \end{bmatrix} \end{aligned} \quad (2.3.4)$$

Consider $P^*(k)$ and $Q^*(k)$ to be the current reference active and reactive powers. As we hope to have the current reference value at the end of the switching cycle, we need to replace $P(k+1)$ and $Q(k+1)$ with $P^*(k)$ and $Q^*(k)$, respectively. Furthermore, for simplicity, we define active and reactive power bits as $\{\delta P = P^*(k) - P(k)\}$ and $\{\delta Q = Q^*(k) - Q(k)\}$, respectively.

In order to have the correct system response, the reference values of PWM for each phase shall be set right before the beginning of the switching cycle. In other words, we need to know the reference voltage vector before going through a switching cycle because in most cases it is not practically possible to change the reference during a cycle. Therefore, detailed analysis of the system would help to find the required reference voltage vector. Neglecting the effect of winding resistance and looking at the inductor, we have:

$$\begin{cases} e_\alpha - v_\alpha = L \frac{di_\alpha}{dt} \\ e_\beta - v_\beta = L \frac{di_\beta}{dt} \end{cases} \quad (2.3.5)$$

where, L is the inductor value.

To find the total current variation within one switching cycle, the average values of power supply and converter voltages are required. The reference voltage of the converter is not determined yet, but we know that it would be constant during the switching cycle, and the average voltage of the power supply with a very good approximation is the power supply voltage at midpoint of the cycle under consideration. No need to say, the midpoint voltage cannot be measured right before starting of the switching cycle and a predictive tool may help to determine this value. This prediction is done by second order extrapolation of Taylor series. Therefore, the midpoint of mains voltages can be predicted as following:

$$\begin{cases} e_\alpha\left(k + \frac{1}{2}\right) = 1.75e_\alpha(k) - e_\alpha(k-1) + 0.25e_\alpha(k-2) \\ e_\beta\left(k + \frac{1}{2}\right) = 1.75e_\beta(k) - e_\beta(k-1) + 0.25e_\beta(k-2) \end{cases} \quad (2.3.6)$$

where $(k + \frac{1}{2})$ represents the midpoint in the upcoming switching cycle. So, by approximating (2.3.5) during the next switching cycle we have:

$$\begin{cases} e_\alpha\left(k + \frac{1}{2}\right) - v_\alpha(k) = L \frac{i_\alpha(k+1) - i_\alpha(k)}{T_s} \\ e_\beta\left(k + \frac{1}{2}\right) - v_\beta(k) = L \frac{i_\beta(k+1) - i_\beta(k)}{T_s} \end{cases} \quad (2.3.7)$$

where, T_s and L are the switching period and the inductor value, respectively.

From (2.3.7) and (2.3.4), the reference voltage vectors for the upcoming cycle are calculated as:

$$\begin{bmatrix} V_\alpha(k) \\ V_\beta(k) \end{bmatrix} = \begin{bmatrix} e_\alpha(k + \frac{1}{2}) \\ e_\beta(k + \frac{1}{2}) \end{bmatrix} - \begin{bmatrix} e_\alpha(k) & e_\beta(k) \\ -e_\beta(k) & e_\alpha(k) \end{bmatrix}^{-1} \left(\begin{bmatrix} \delta P \\ \delta Q \end{bmatrix} - \begin{bmatrix} \Delta e_\alpha(k) & \Delta e_\beta(k) \\ -\Delta e_\beta(k) & \Delta e_\alpha(k) \end{bmatrix} \begin{bmatrix} i_\alpha(k) \\ i_\beta(k) \end{bmatrix} \right) \frac{L}{T_s} \quad (2.3.8)$$

Block diagram of the resulting system is shown in Fig 2.3.1.

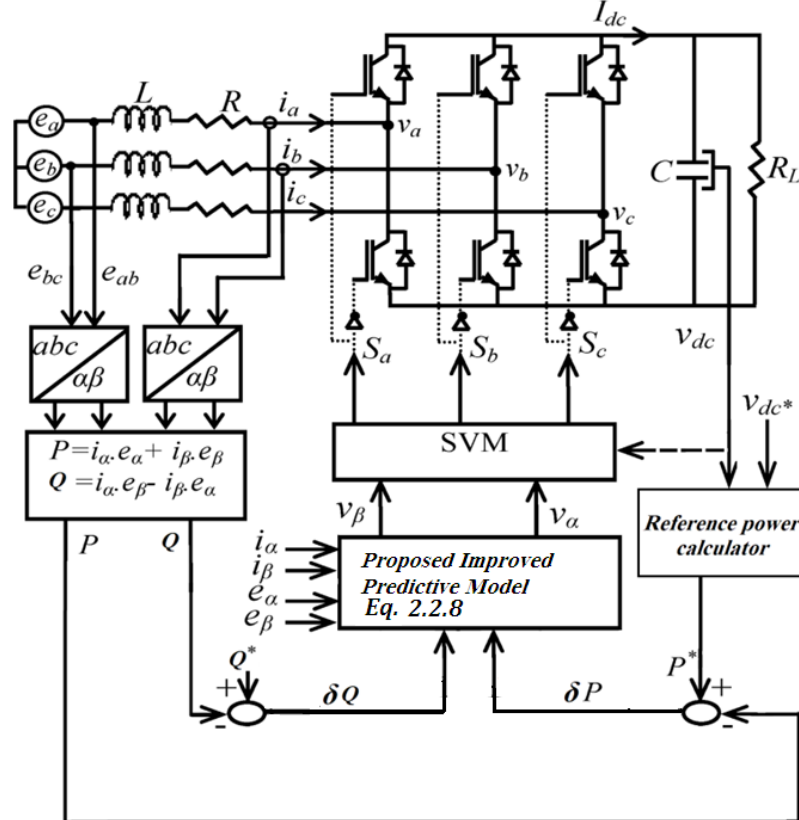


Fig 2.3.1. Block diagram of proposed controller

2.3.2. Simulation Results

To verify the viability of the proposed improved predictive solution (IP-DPC), the method is simulated and compared with the recently presented P-DPC (Bouafia et al., 2010). Simulations are performed under steady-state and transient conditions. Parameters of the simulated three-phase rectifier are listed in table 2.3.1.

TABLE 2.3.1- Parameters used in simulations

Parameter	Value
Input line to line voltage	240 V/ 50Hz
Input inductors	80 mH
Dc bus voltage	350 V
Switching and sampling frequencies	2 KHz

a. Steady-State Simulations

Fig 2.3.2 a and b show the three-phase input current waveforms of P-DPC and IP-DPC, respectively. The total harmonic distortion (THDi) for P-DPC is recorded as 6.1% whereas this is 6.2% for proposed method. One can say the THD is almost the same for both methods. Fig 2.3.3 a and b show the power supply and reference voltages of converter in $\alpha - \beta$ axis for P-DPC and proposed methods, respectively.

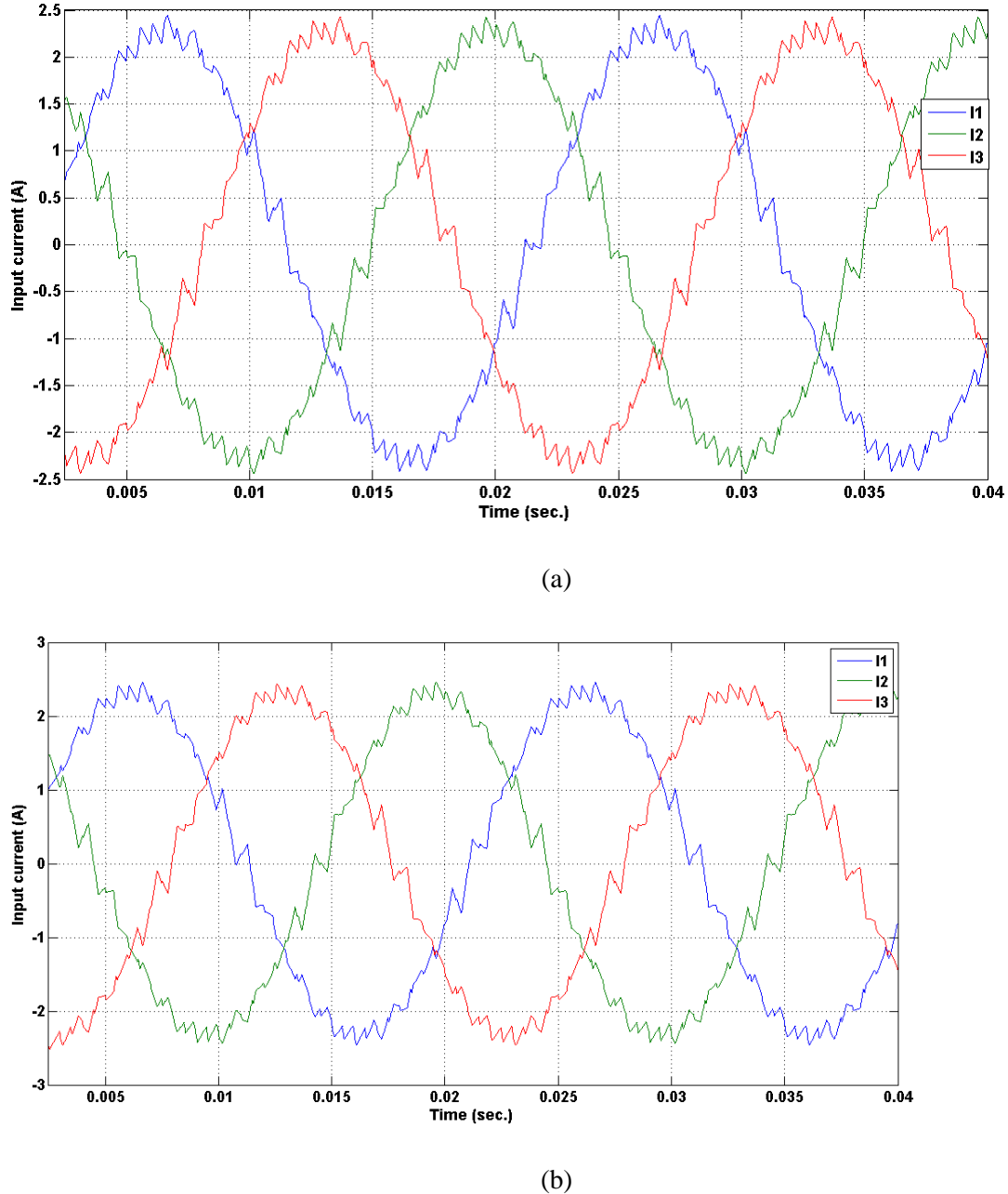
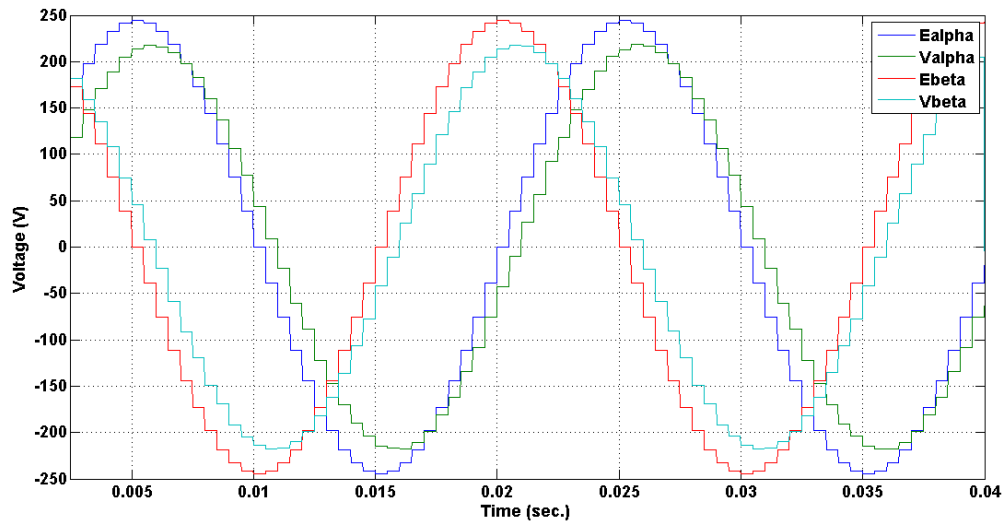
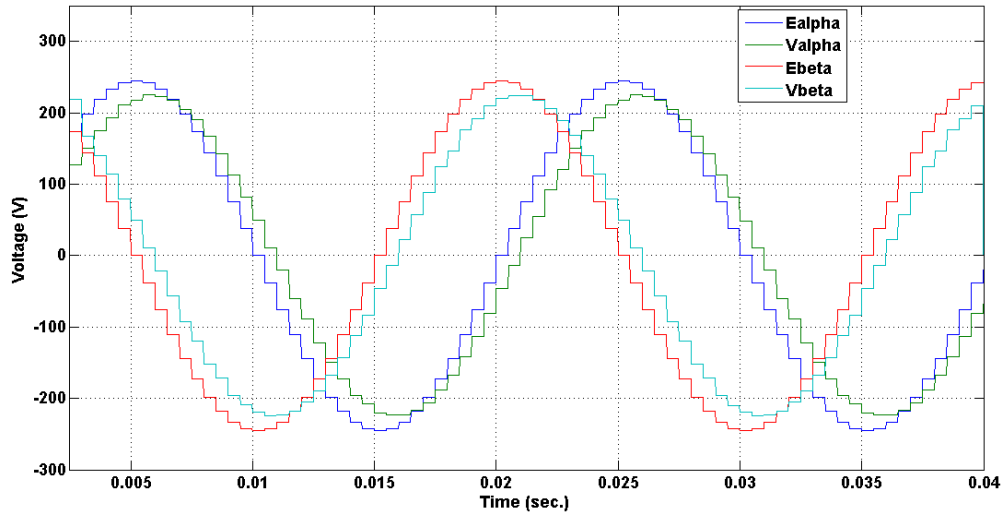


Fig 2.3.2. Steady-State Simulations: Three-phase input currents for (a) P-DPC, (b) proposed IP-DPC method



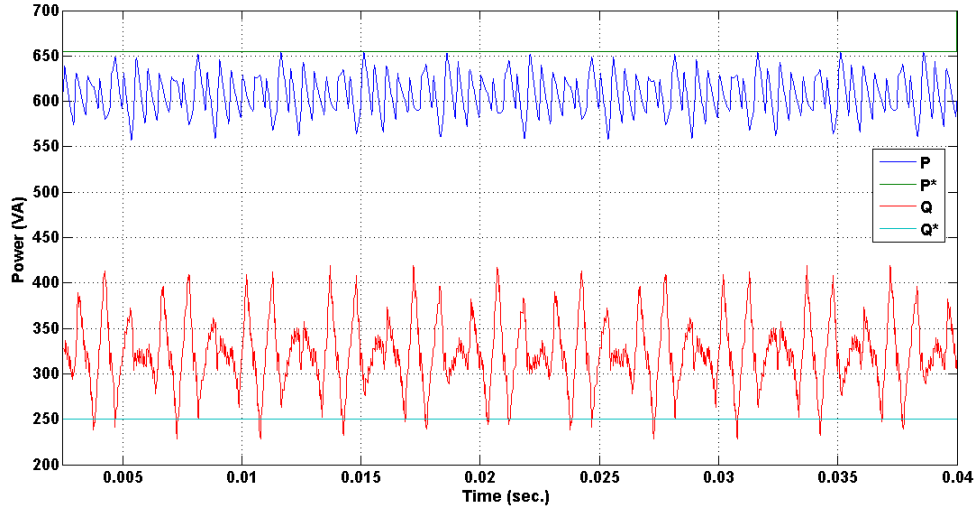
(a)



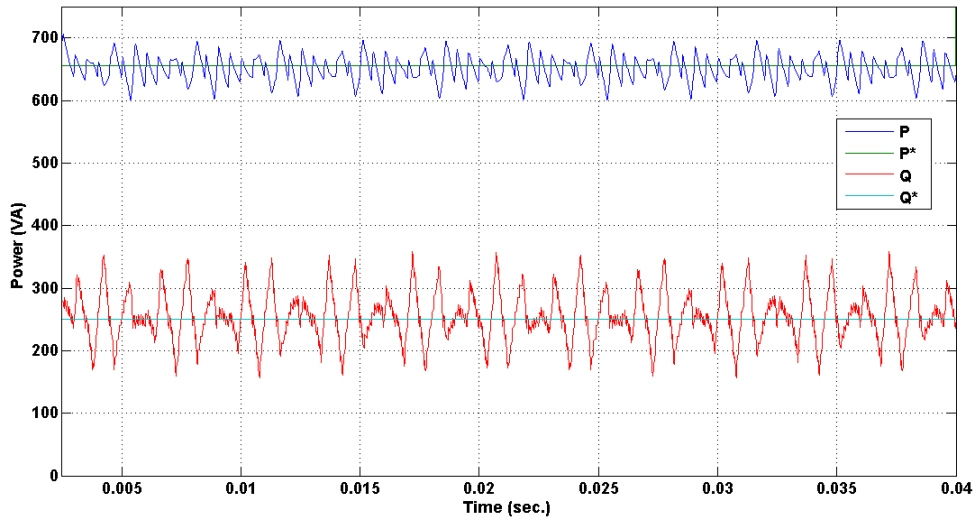
(b)

Fig 2.3.3. Steady-State Simulations: input and reference voltage of converter in $\alpha - \beta$ axis for (a) P-DPC, (b) proposed IP-DPC method

Fig 2.3.4 a and b show the input active and reactive power for the two controllers. As demonstrated in Fig 2.3.4a for the P-DPC, there is an offset error associated with both active and reactive powers, whereas for proposed IP-DPC the average active and reactive power is equal to the reference values. This is one of the advantages of the proposed controller and proves that the mathematical model improves the accuracy of the P-DPC method.



(a)



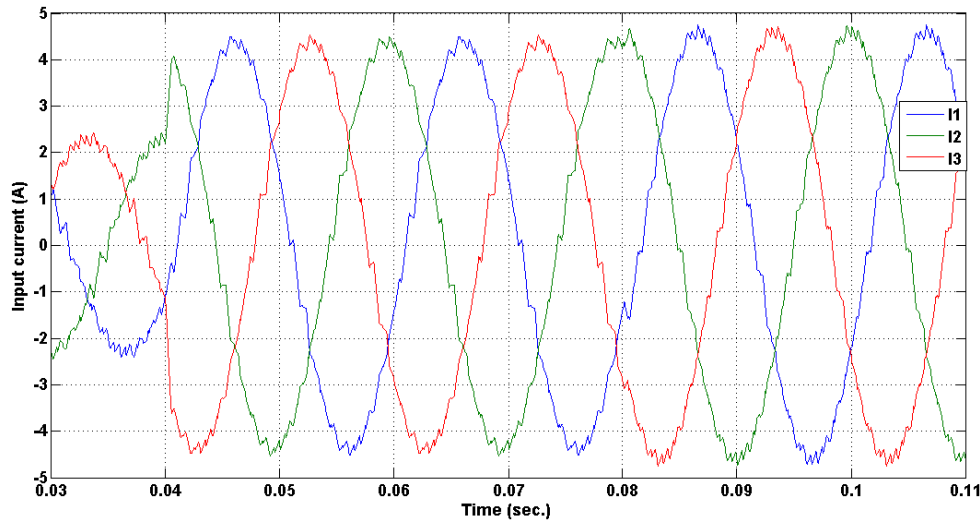
(b)

Fig 2.3.4. Steady-State Simulations: input active and reactive power of converter for (a) P-DPC, (b) proposed IP-DPC method

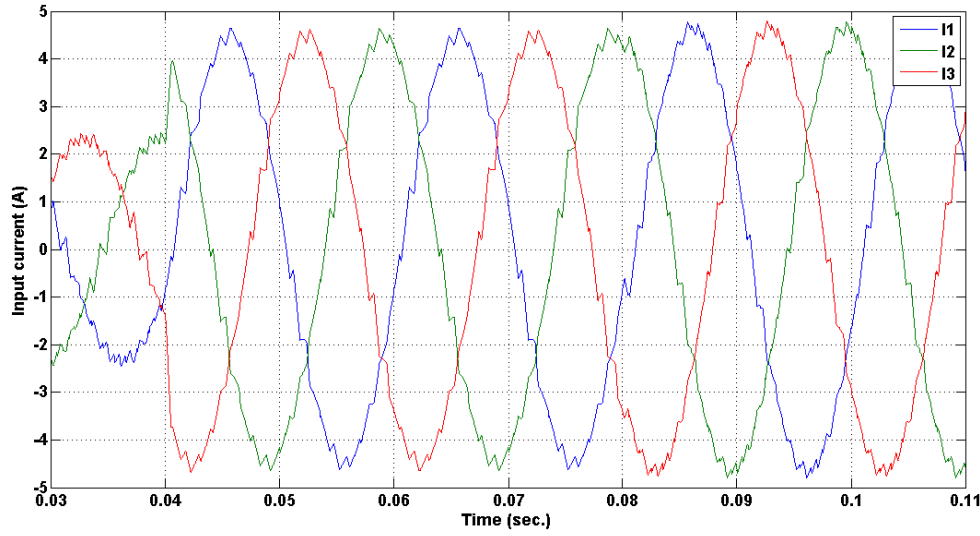
b. Transient Simulations

Transient simulations are performed considering step changes in active power reference values at $t=0.04$ s. The reference active power is changed from 650W to 1300W. The reactive power reference value also changes at $t=0.08$ from 250 VAR to 500VAR. Fig 2.3.5 a and b show the three-phase input current waveforms of P-DPC and proposed methods, respectively. It is observed that, for both methods the system has responded to the setpoint change very quickly. Fig 2.3.6 a and b show the power supply and reference voltage of converter in $\alpha - \beta$ axis for P-DPC and proposed methods, respectively. Also, the input active and reactive power for P-DPC and proposed methods are shown in Fig 2.3.7 a and b respectively. As with the steady-state waveforms, P-DPC introduces an offset in

both active and reactive powers for new power setpoint. Clearly, there will be undesired cross-coupling effects due to these offsets. That is the offset in the active (reactive) power will have a negative impact on the reactive (active) power waveform. However according to Fig 2.3.7b, the proposed IP-DPC overcomes this deficiency such that average active and reactive powers are equal to their reference values. In addition, the sampled active and reactive power bits that fed into the predictive controller for P-DPC and proposed methods are shown in Fig 2.3.8 a and b respectively. In order to have minimum deviation error from the reference values they should be very close to zero except at very moment of step change in the reference. However, for P-DPC the active and reactive power bits have an offset error whereas for IP-DPC the values are very close to zero.

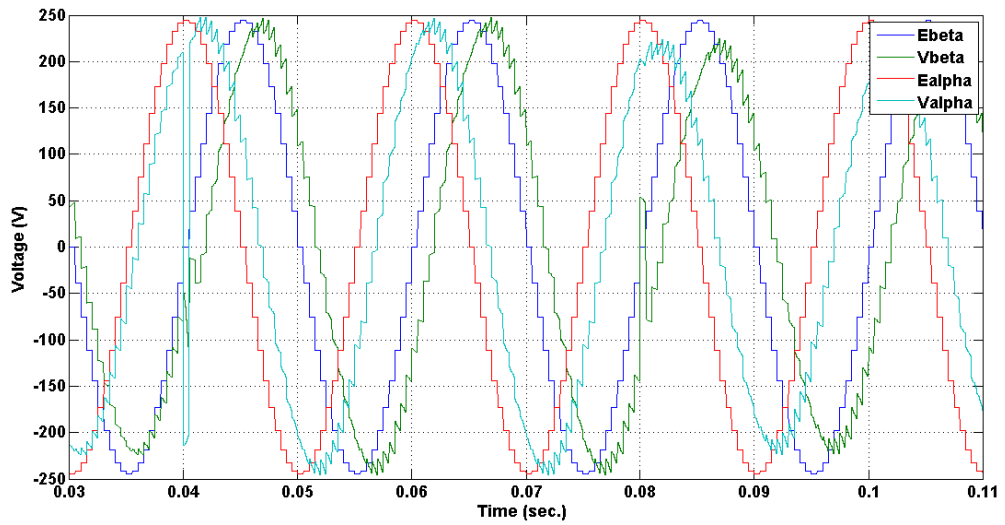


(a)

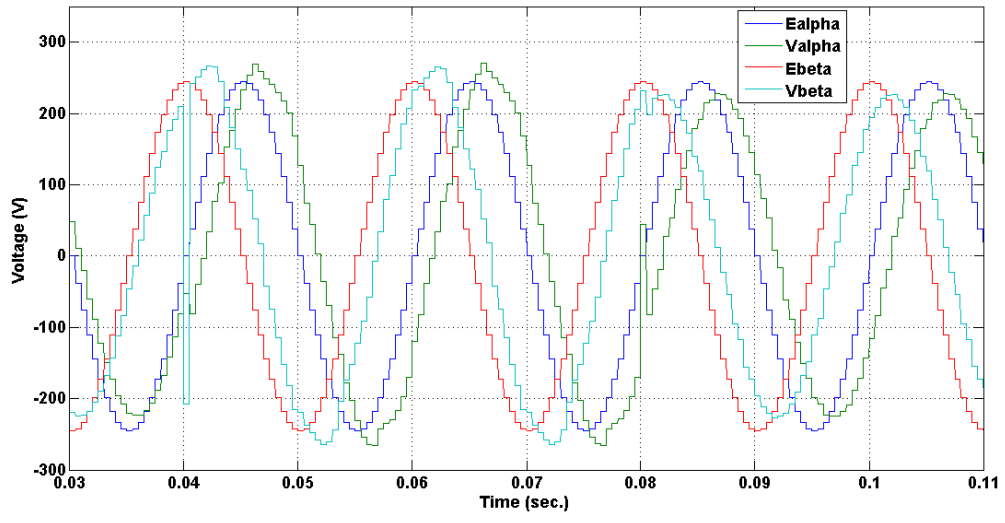


(b)

Fig 2.3.5. Transient simulations: Three-phase input currents for (a) P-DPC, (b) proposed IP-DPC method

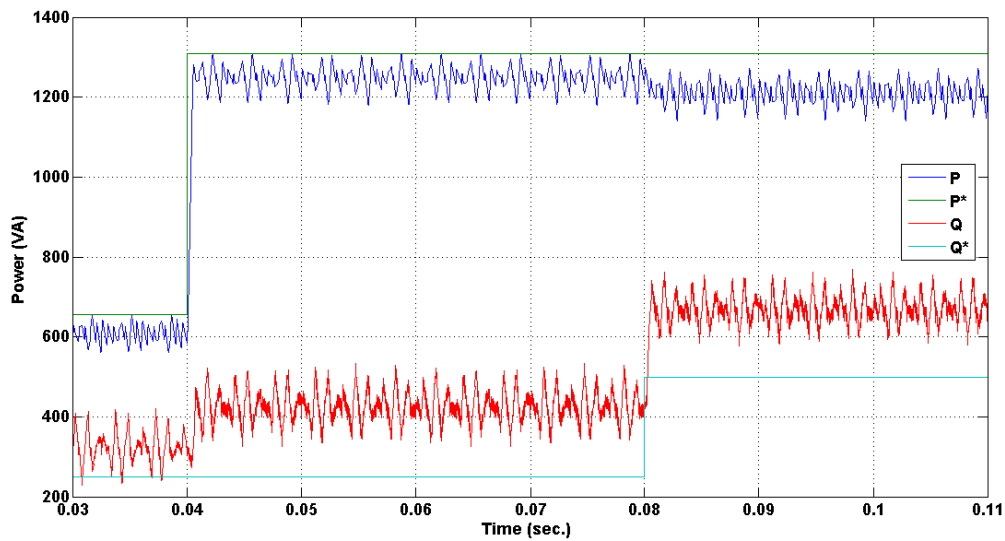


(a)

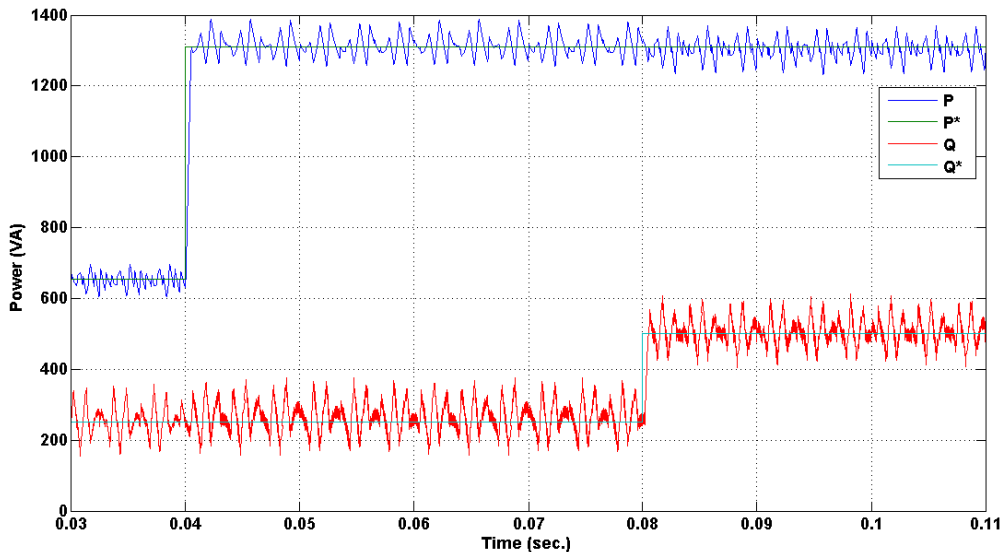


(b)

Fig 2.3.6. Transient Simulations: input and reference voltage of converter in $\alpha - \beta$ axis for (a) P-DPC, (b) proposed IP-DPC method

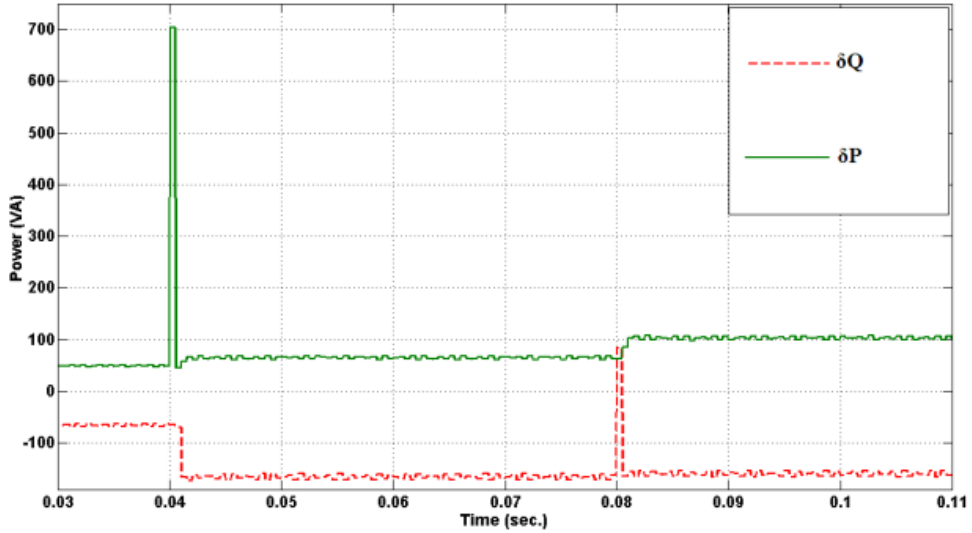


(a)

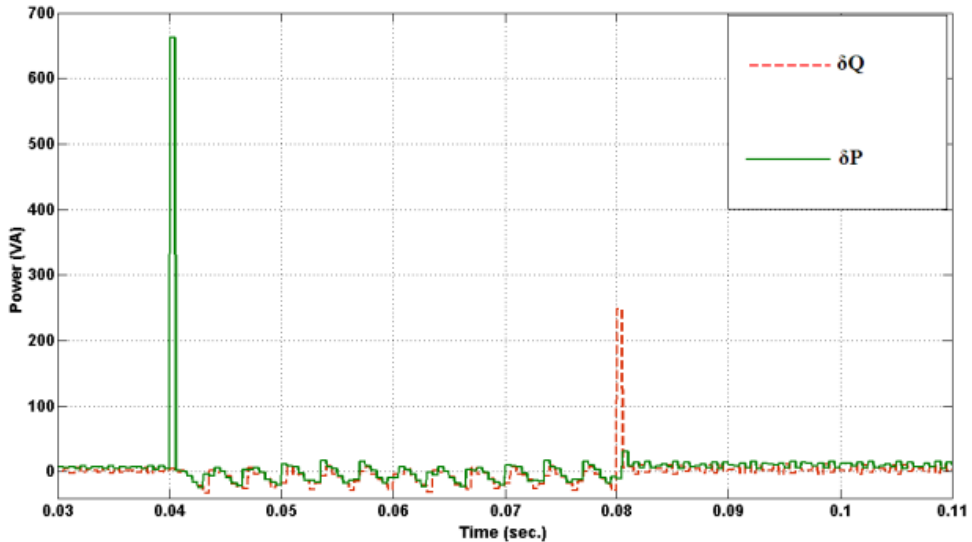


(b)

Fig 2.3.7. Transient Simulations: input active and reactive power of converter for (a) P-DPC, (b) proposed IP-DPC method



(a)



(b)

Fig 2.3.8. Transient Simulations: sampled active and reactive power bits for (a) P-DPC, (b) proposed IP-DPC method

2.3.3. Conclusions

In IP-DPC system a more accurate mathematical model is employed to improve the performance of a recently introduced predictive direct power controller (P-DPC). The method uses a constant switching frequency and can very precisely follow the active and reactive power references. The proposed controller is very fast with no steady state error which makes it especially suitable for high power applications with low switching frequencies. Detailed simulation results and their comparisons with P-DPC prove the feasibility of the proposed solution.

2.4. Fuzzy Predictive Direct Power Control (FP-DPC)

2.4.1. Principles of operation

In order to have a predictive direct power controller (P-DPC) it is sufficient to apply the reference voltage vectors of (2.3.8) to the SVM module. However, the system would operate as anticipated and provide the required active and reactive powers in next switching cycle, if parameters are estimated correctly, measurements are done accurately with no time delay, and also no filters are employed. This is not usually the case since the estimated inductor value may not be very accurate, the measurements are not done precisely, and some sort of filtering are required to have more stable signals and more realistic measurements. As a result, in practice the active and reactive powers at the end of the upcoming switching cycle are different from the expected values, and the errors must be compensated in next switching cycle. However due to the above-mentioned reasons, the error may not totally disappear in next switching cycle and stay within the system in form of unwanted oscillations.

The power feedback loop plays a main role in the outcome of the rectifier. This is because in case of any inaccuracies the resulting active and reactive powers are not equal to the predicted values. If active and reactive powers are less than the predicted values, the remaining amount of power demand would be responded in future switching cycles. It may not affect the steady-state operation of the system, but as it takes more than a switching cycle to provide the reference power it will degrade system dynamics. On the other hand, when the output powers are larger than the predicted values, the system will have an error which disturbs the steady-state operation. However, discarding unwanted oscillations, the system responds to the setpoint very quickly.

The author of this thesis proposes a Fuzzy signal conditioner module to improve the performance of the power feedback loop by rescaling the error. Downscaling the error signal results in smoother operation but poor transient performance, while magnifying it, will lead to faster transient performance but poor steady state responses. Therefore, a signal conditioner system will be employed to ensure acceptable transient and steady state responses even with inaccuracies in circuit parameter estimations. The main task of the signal conditioner module is to effectively increase (magnify) and decrease (downscale) the error signal for large and small levels of the error, respectively. Since the time is limited to one switching cycle, the module should respond to input very quickly. Also, the only control parameter is the amplitude of error in every switching cycle, no historical information is required. Considering these requirements, fuzzy logic (Zadeh, 1965) is one of most appropriate solutions for this application as it can be designed to provide variable rescaling factors in respect to the magnitude of error.

The proposed input and output membership functions are shown in Fig 2.4.1 (a) and (b), respectively. Input membership functions are selected in order to have the algebraic sum (Zadeh, 1965) of all memberships to be equal to one for any particular input. Also widely used triangular membership functions would help to reduce the calculation time. Output of fuzzy module will be used as a rescaling factor that will be multiplied by the error. Consequently, the output functions are selected such that the maximum output magnitudes of fuzzy module are limited to two. That is in case of maximum magnification, the signal is twice of the measured error.

Consider μ as the input membership matrix which is sorted as:

$$\mu = [NVB, NB, NS, ZE, PS, PB, PVB] \quad (2.4.1)$$

where, the abbreviations *PVB*, *PB*, *PS*, *ZE*, *NS*, *NB*, and *NVB* stand for *positive very big*, *positive big*, *positive small*, *equal to zero*, *negative small*, *negative big*, and *negative very big*, respectively.

Also, output membership function γ can be represented as set of coefficients that are arranged as:

$$\gamma = \left[-2, -\frac{4}{3}, -\frac{2}{3}, 0, \frac{2}{3}, \frac{4}{3}, 2 \right] \quad (2.4.2)$$

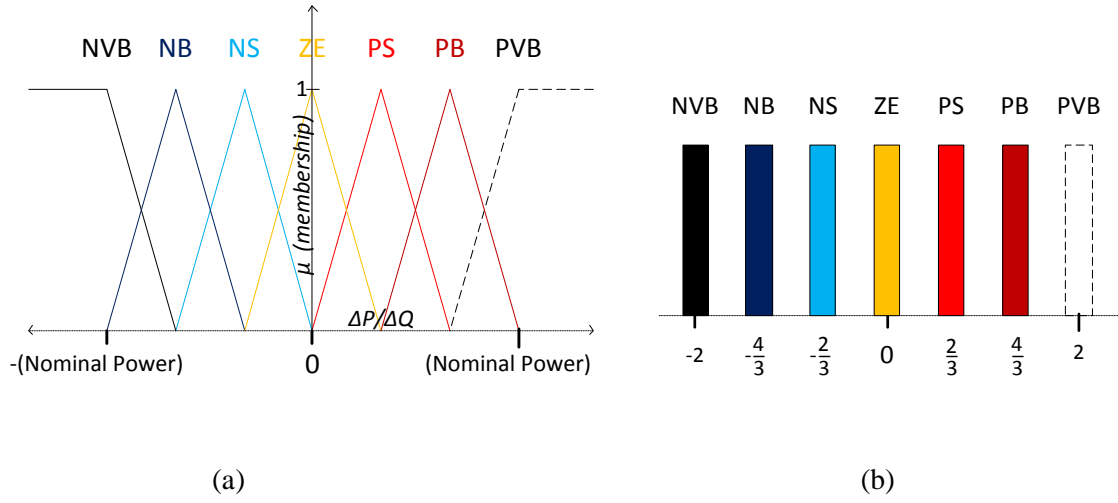


Fig 2.4.1. Membership functions for; (a) input error, (b) output signal

Since there is only one input, no fuzzy inference rule is required. In practice, this will also help to perform the calculations very quickly. As the algebraic sum of all input membership functions is one, no inference rule is defined, and considering the fact that rescaling factor must be a positive value (e.g., the sign of error signal cannot be changed), using centroid defuzzification method the rescaling factor can be easily calculated as:

$$\begin{cases} R_P = \left| \sum_{i=1}^7 (\mu_i(\Delta P) \times \gamma_i) \right| \\ R_Q = \left| \sum_{i=1}^7 (\mu_i(\Delta Q) \times \gamma_i) \right| \end{cases} \quad (2.4.3)$$

where, R_P and R_Q are the rescaling factors for active and reactive power errors, respectively. The resulting fuzzy signal conditioner module is graphically presented at Fig 2.4.2.

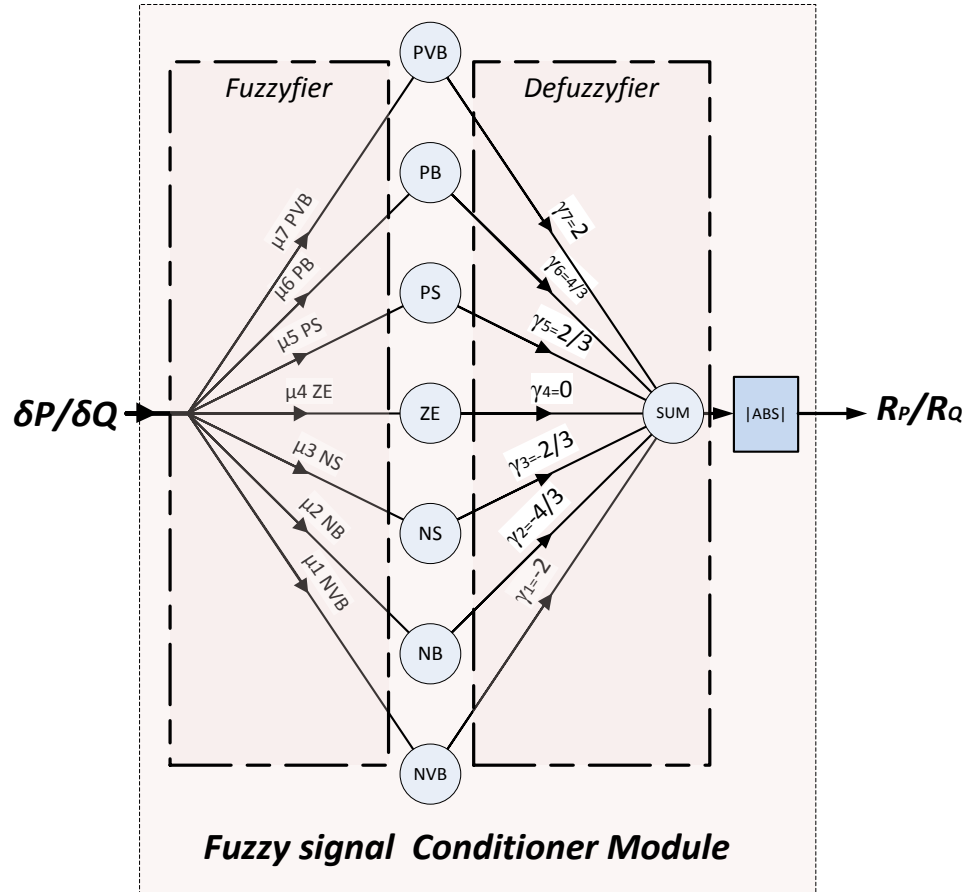


Fig 2.4.2. Graphical representation of the proposed Fuzzy signal conditioner module

The output of the rescaling module (R_P or R_Q) is the rescaling factor of error and shall be multiplied with the actual error to get the rescaled error signals:

$$\begin{cases} \Delta P_r = \delta P \times R_P \\ \Delta Q_r = \delta Q \times R_Q \end{cases} \quad (2.4.4)$$

where, ΔP_r and ΔQ_r are the rescaled error signals for active and reactive powers, respectively. The resulting system to modify error signal is shown in Fig 2.4.3 a and b for active and reactive powers, respectively. The block diagram of the converter with the proposed controller is shown in Fig 2.4.4.

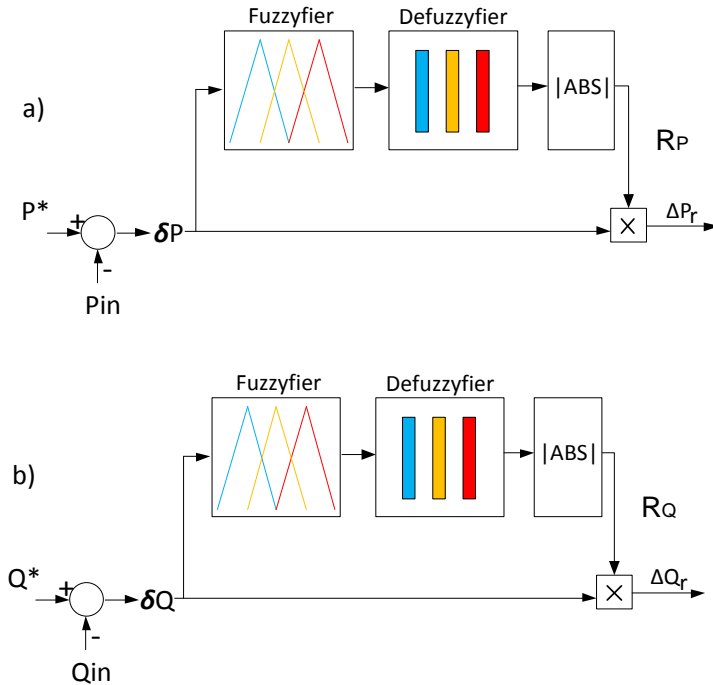


Fig 2.4.3. Proposed rescaling fuzzy controller for; (a) active power (b) reactive power

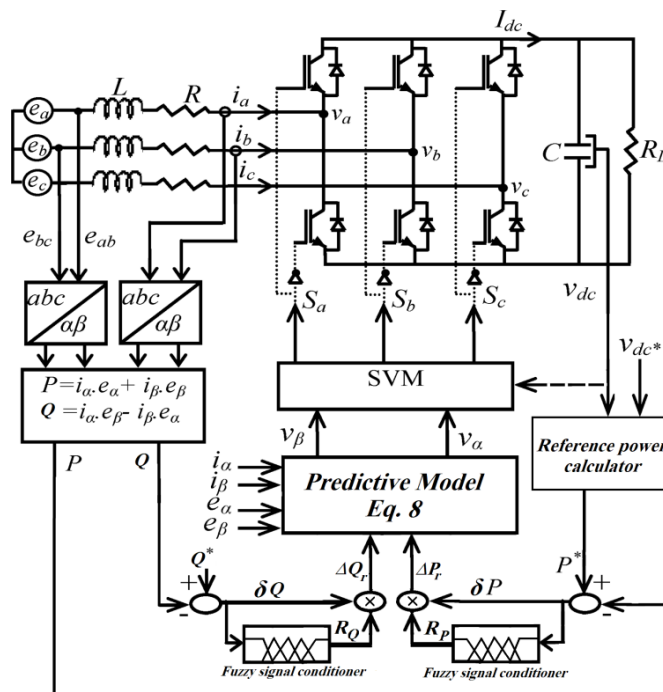


Fig. 2.4.4. Overall block diagram of the converter with the proposed fuzzy predictive controller

2.4.2. Simulation Results

Two conversion approaches are simulated and compared; the P-DPC introduced in (Bouafia et al., 2010) and the proposed FP-DPC. Parameters of the simulated three-phase rectifier are listed in Table

2.4.1. Also, due effectiveness of filtration in practice, to have more stable measurements, a low-pass filter with cutoff frequency at 3 KHz is employed to remove high frequency ripples of current signal.

TABLE 2.4.1 - Three-phase rectifier parameters used in simulations

Parameter	Value
Input line to line voltage	240 V/ 50Hz
Input inductors	8 mH
Resistive load	187Ω
DC capacitor	300μF
Switching frequency	10 Hz

a. Steady-State Simulations

To compare the steady-state performances of the P-DPC and proposed FP-DPC controllers and their sensitivities and dependencies on parameter variations, detailed simulations are performed for a wide range of error in the inductor estimation. Fig 2.4.5 compares the total harmonic distortion of input current (THDi) for different estimation of the inductor. The proposed FP-DPC shows a relatively low THD of about 7.5% for a wide range (from -100% to +100%) of parameter estimation error. However with the P-DPC, the error increases exponentially for overestimated values above 30%.

An inductor estimation error of +45% is selected as a sample operating point to show detailed simulated time domain waveforms of both controllers. This operating point is selected to show the appearance of sub-harmonic components in converter waveforms due to inductor estimation error in P-DPC method. Fig 2.4.6 a and b show the three-phase input current waveforms of P-DPC and FP-DPC, respectively. Fig 2.4.6a clearly displays the undesired sub-harmonic components of input currents (with frequencies below the switching frequency) caused by P-DPC, while using the proposed FP-DPC, current waveforms are moderately sinusoidal (Fig. 2.4.6b).

Figs 2.4.7 a and b show the power supply and reference voltage of the converter in $\alpha - \beta$ axis for P-DPC and FP-DPC methods, respectively. It can be seen that the parameter estimation error would lead to have a wrong reference voltage in every switching state, and the system is unable in damping the corresponding error. This will eventually introduce oscillations in the input current waveforms. The input active and reactive powers for P-DPC and proposed FP-DPC methods are shown in Figs 2.4.8a and b, respectively. As with the current waveforms, there are considerable oscillations with the P-DPC whereas in FP-DPC there is no sign of oscillations.

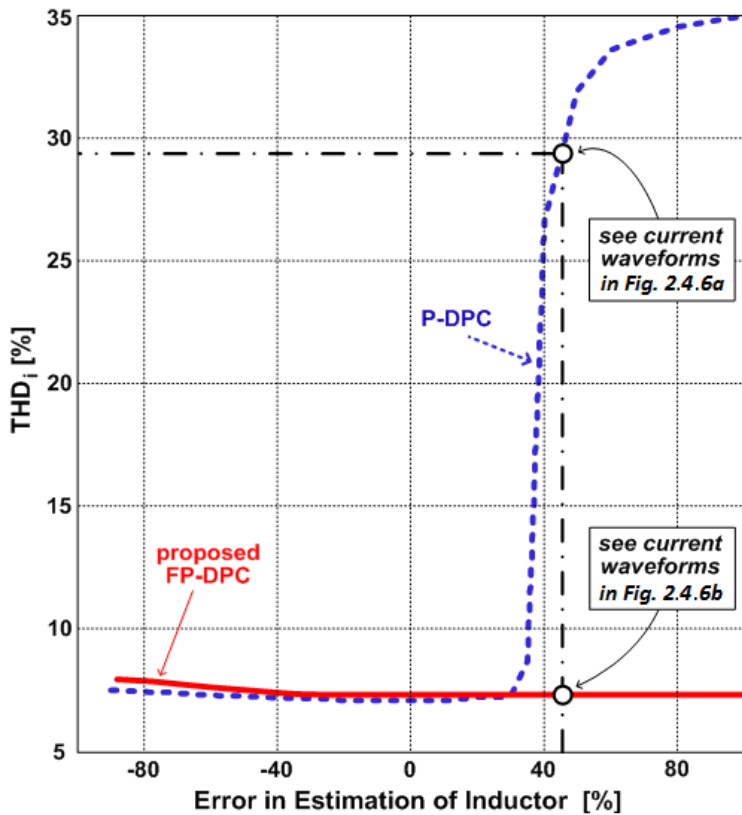


Fig. 2.4.5. Total harmonic distortion of input current (THDi) for different estimation values of the inductor

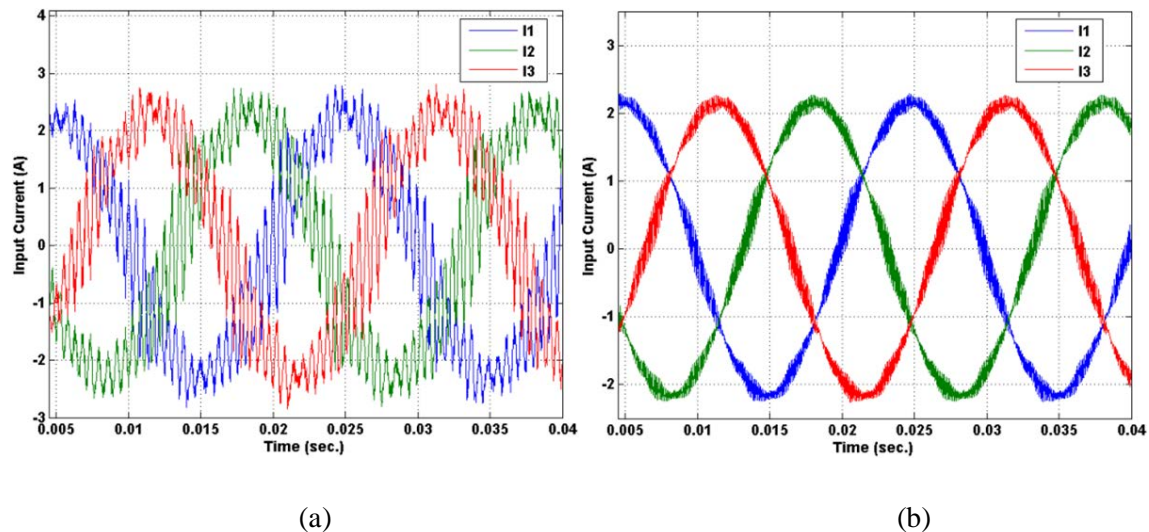


Fig. 2.4.6. Steady-state simulations: three-phase input currents for +45% estimation error of the inductor; (a) P-DPC, (b) proposed FP-DPC

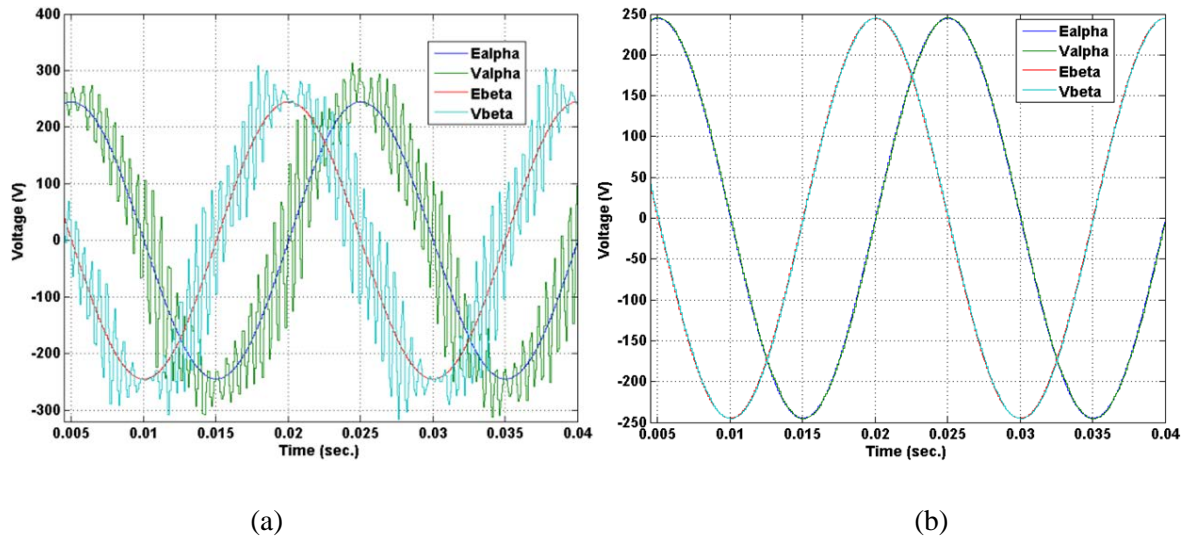


Fig. 2.4.7. Steady-state simulations: input and reference voltage of the converter in $\alpha - \beta$ axis for +45% estimation error of the inductor; (a) P-DPC, (b) proposed FP-DPC

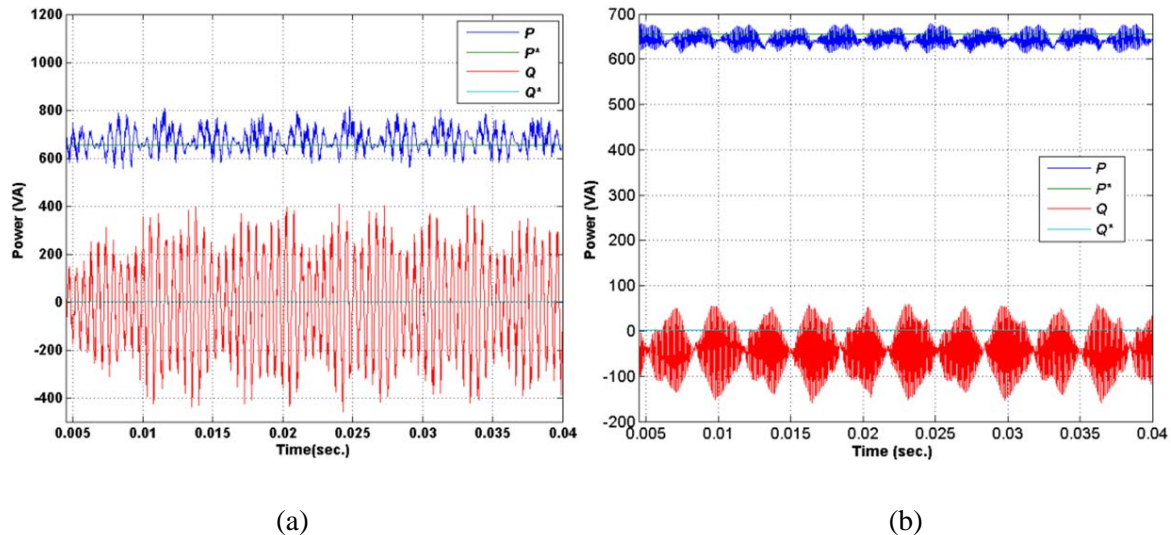


Fig 2.4.8. Steady-state simulations: input active and reactive powers of the converter for +45% estimation error of the inductor; (a) P-DPC, (b) proposed FP-DPC

b. Transient Simulations

Transient simulations are performed considering a moderated step change in active power reference value at $t=0.06\text{s}$. The reference active power is changed from 650W to 1300W while the reactive power reference value is set to zero. The estimation error of inductor is considered to be +45%.

Fig 2.4.9a and b show the three-phase input current waveforms of P-DPC and FP-DPC, respectively. Both controllers have very quick transient responses and oscillations in current waveform have no major change in magnitude due to the step change. However with the proposed FP-DPC, current waveforms for new power level are still clean with no significant oscillations.

Fig 2.4.10a and b show the power supply and reference voltage of converter in $\alpha - \beta$ axis for P-DPC and FP-DPC methods, respectively. It can be seen that the parameter estimation error before and after $t=0.06$ has the same effect on reference voltage in causing undesired oscillations. However with FP-DPC, the reference vectors are pure sinusoidal waveforms at the new power level. For a couple of switching cycles after the step change (at $t=0.06$), the reference voltages have transient distortions to compensate for the new reference power. Note that transients damp out very quickly.

The input active and reactive powers for P-DPC and proposed FP-DPC methods are shown in Fig 2.311a and b, respectively. For P-DPC, the oscillations also exist for input active and reactive power waveforms before and after the change in reference power. Because of these oscillations, the overshoot of tracking the reference power is higher. However, the proposed FP-DPC is capable of tracking the reference power very quickly and forcing the error close to zero at all the times. According to these simulations, the proposed FP-DPC has faster transient response even with large parameter estimation errors.

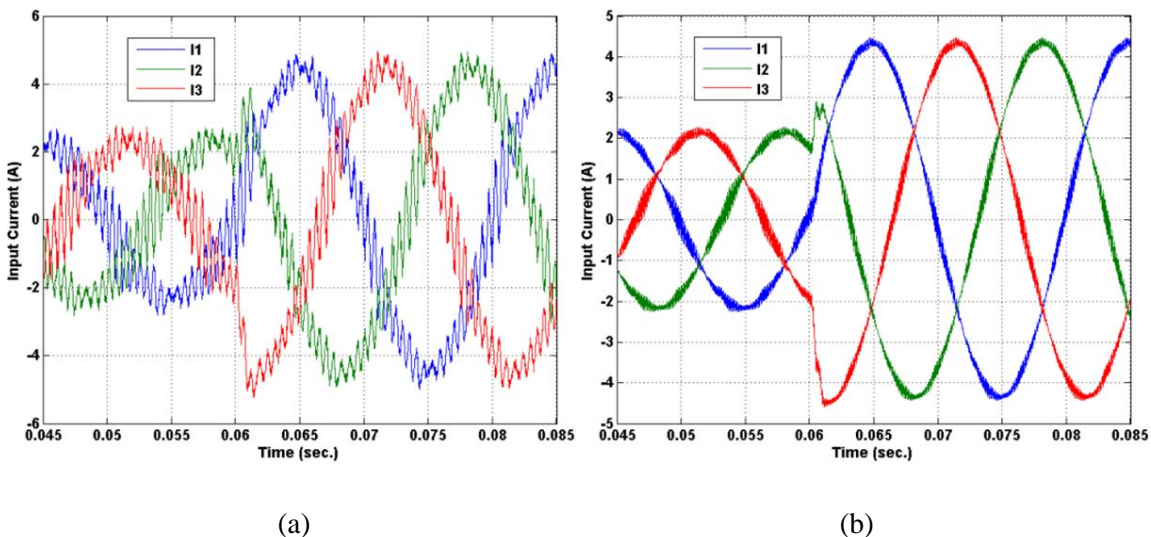


Fig 2.4.9. Transient simulations: Three phase input currents for +45% estimation values of the inductor; (a) P-DPC, (b) proposed FP-DPC

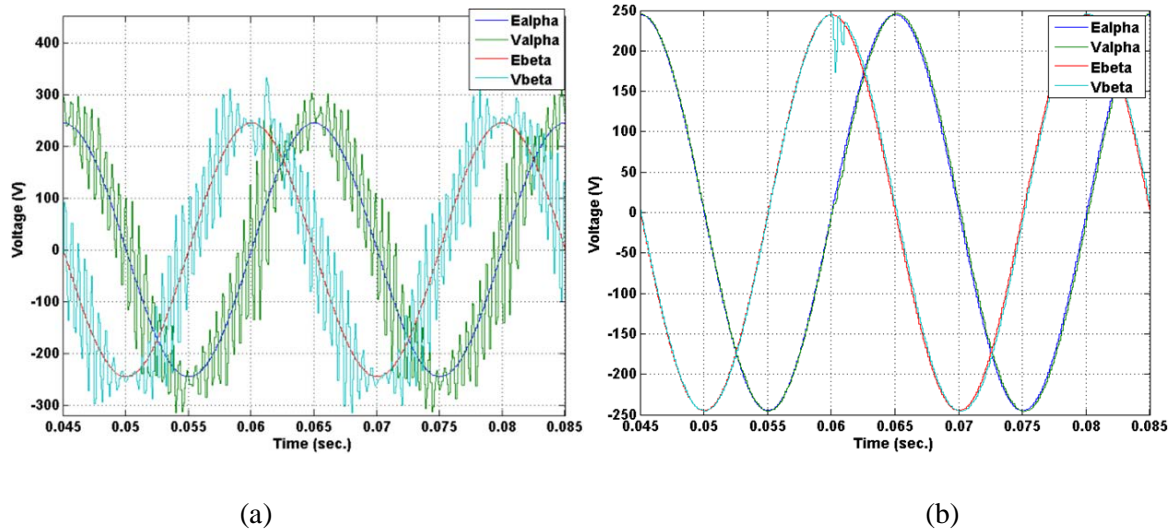


Fig 2.4.10. Transient Simulations: input and reference voltage of converter in $\alpha - \beta$ axis for +45% estimation error of the inductor; (a) P-DPC, (b) proposed FP-DPC

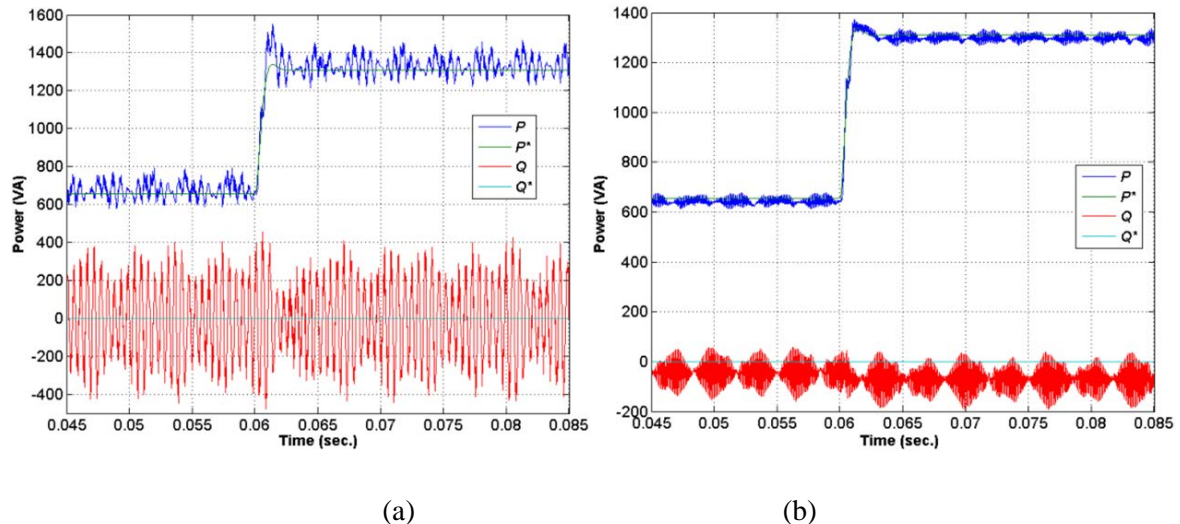


Fig 2.4.11. Transient Simulations: input active and reactive powers of converter considering +45% estimation error of the inductor for; (a) P-DPC, (b) proposed FP-DPC

2.4.3. Experimental Results

Fig 2.4.12 shows the experimental setup, the main controller is implemented by the Texas Instrument TMS320F28335 processor. This is a floating point DSP operating with a 150MHz clock. It can have upto16 analog measurements at 12.5 million samples per second (MSPS). However for the experimental setup, the current and voltage signals are measured at 100KSPS; this high sampling rate is used to record very clear signals using oversampling techniques. For this reason, an infinite impulse response (IIR) filter with a cut-off frequency of 3KHz is used to make a digital low pass filter. This

will prevent switching ripples in the measurements. The power measurements are recorded by a power quality analyser HIOKI 3196, which will provide instantaneous data in csv format to be used by computer. The system parameters are listed in Table 2.4.2.

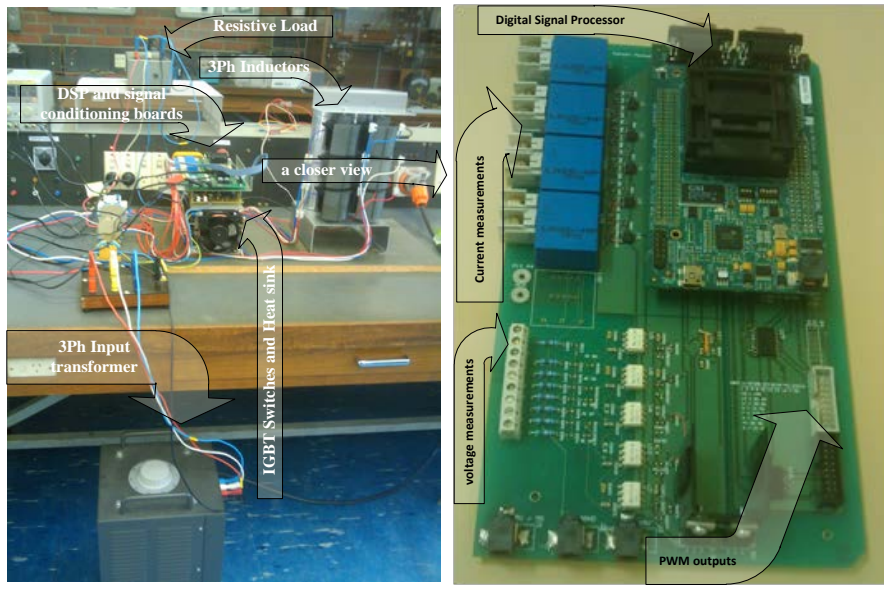
TABLE 2.4.2- Three-phase rectifier parameters used in Experimentations

Parameter	Value
Input voltage magnitude (line to line) and frequency	100 V/ 50Hz
Input inductors	8 mH
Resistive load	187Ω
DC capacitor	300μF
Switching frequency	10 KHz

Extensive measurements are performed to investigate the validity of the proposed FP-DPC approach and the accuracy of simulations, as well as the impact of parameter estimation error.

Fig 2.4.13 and 2.4.14 show the current waveforms with a step change in the reference power from 100W to 200W for the P-DPC and FP-DPC methods, respectively. These measurements are similar and confirm the simulation results presented in Section IV. However, there are some traces of sub switching oscillations in the measured waveforms of PDPC due to inaccuracies in practical implementation of the method. As expected, there are no significant oscillations with the proposed FP-DPC approach.

To investigate the effect of inductor estimation error on the system output, a number of measurements are performed. Figs 2.4.15 and 2.4.16 show the current waveforms for a step change in the reference power from 150W to 100W and with +35% error in the inductor estimation, for the P-DPC and FP-DPC methods, respectively. As previously explored (Fig. 2.4.15), P-DPC method creates substantial sub-switching oscillations in the waveform while there are no significant oscillations associated with the proposed FPDPC approach.



(a)

(b)

Fig 2.4.12. Laboratory setup; (a) test bench used for measurements, (b) designed and constructed control board of power electronics converter

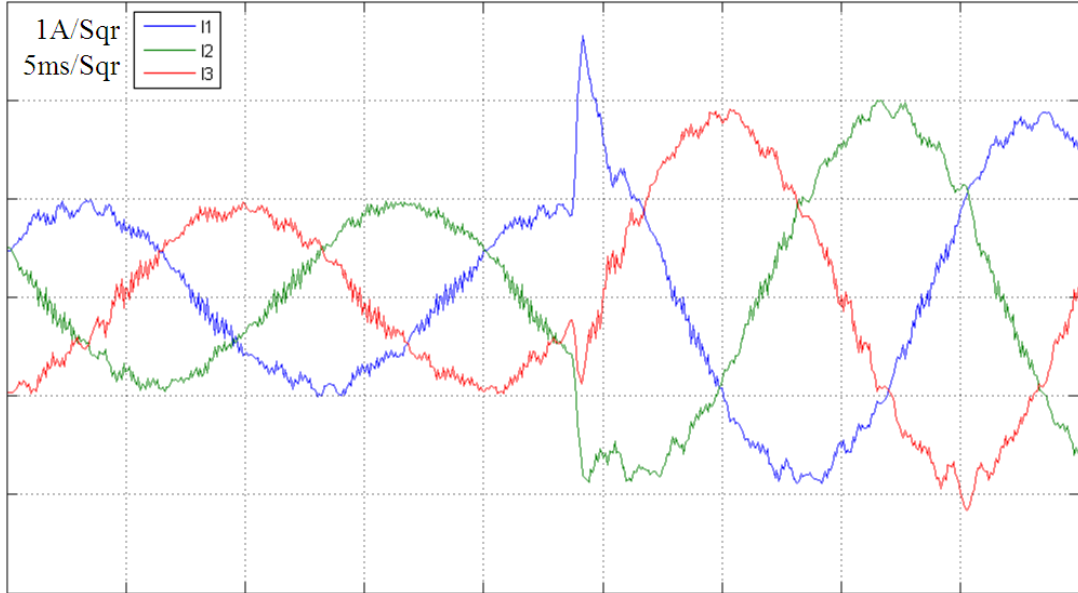


Fig 2.4.13. Experimental results: current waveforms for the P-DPC

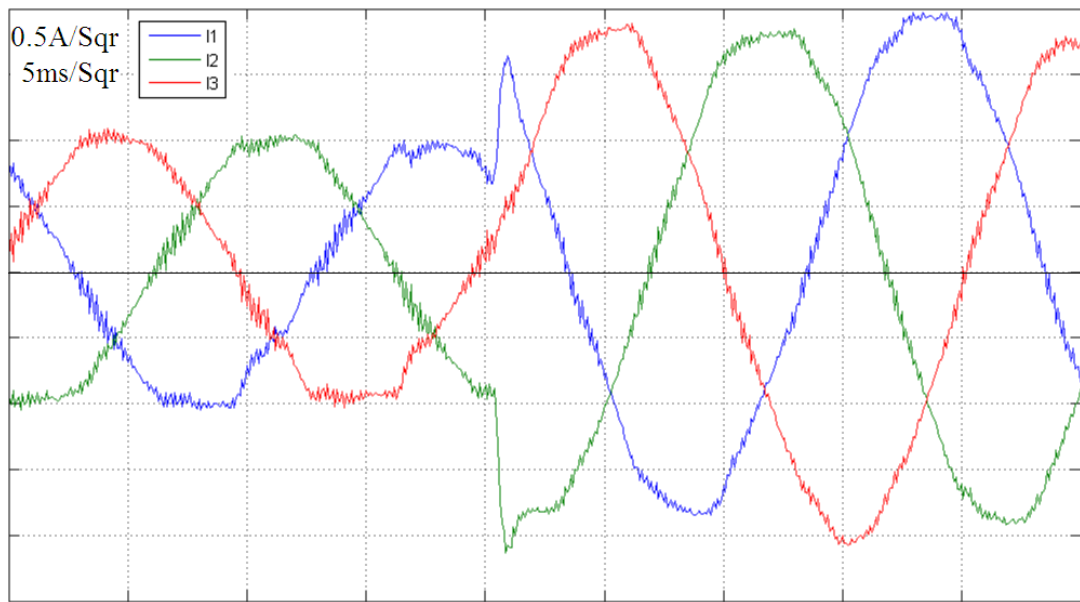


Fig 2.4.14. Experimental results: current waveforms for the proposed FP-DPC

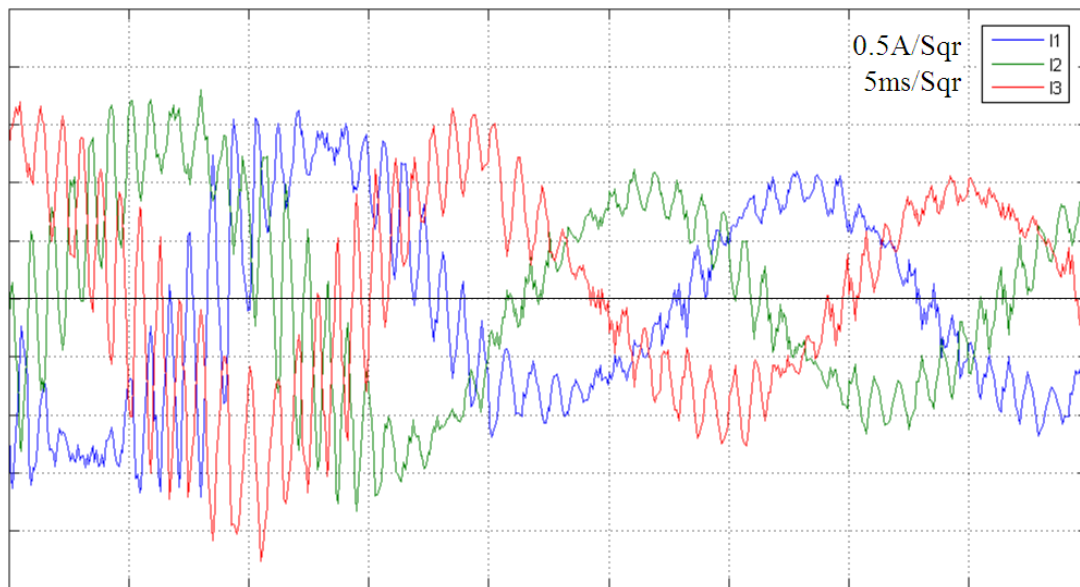


Fig 2.4.15. Experimental results: current waveforms for the P-DPC approach with +35% error in the inductor estimation

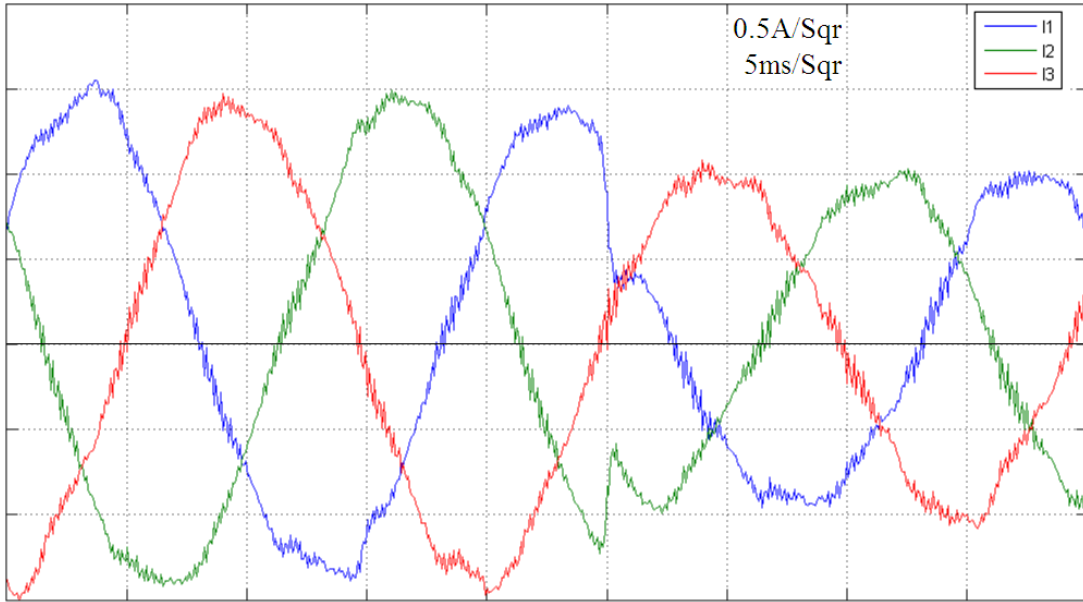


Fig 2.4.16 Experimental results: current waveforms for the proposed FP-DPC approach with +35% error in the inductor estimation

2.4.4. Conclusions

A fuzzy predictive direct power control (FP-DPC) strategy is proposed, simulated and implemented using a Texas Instrument microprocessor. Two separate fuzzy blocks modify the active and reactive power error signals before applying it to P-DPC module. The idea behind this new strategy is to reduce the stress on the control system in steady state condition and also to obtain faster transient response. The resulting controller benefits from the smoothness of vector based solutions and the natural quick response of P-DPC methods. The simulations and experimental results prove the feasibility of the proposed solution.

Based on simulation and experimental results, the proposed method has the following advantages:

- It uses a vector base switching pattern with a constant switching frequency.
- It utilizes an accurate converter model that ensures better operation in low switching or high power applications without substantial sub-switching oscillations.
- Due to the application of a simple fuzzy signal conditioner block, the new controller is less sensitive to parameter variations i.e. input inductor estimation errors.

2.5. Average Current Control Strategy

2.5.1. Principles of operation

The goal of the control system is to keep the output DC voltage constant and also to maintain the input currents similar to a sinusoidal waveform to limit the harmonic content of current waveforms.

Average, current mode control (ACC) is well known method for dc-dc applications. It provides reference current in a few switching cycles, while the switching frequency is constant. It has been used for single-phase rectifiers. Three-phase unidirectional power flow rectifiers are also presented. However, bi-directional power flow three phase application of this method is not supported with enough documents in previous researches.

The basic of average current controller is to keep average of current near reference current value in each switching cycle. So, to achieve this, it is ideal to have integration of error during the whole switching cycle. Fig.2.5.1 shows the reference current and possible actual current, the error signal and switching states of one single phase of rectifier which work with this strategy. In every switching cycle the correspondent switch would be turned on and the opposite switch of the same phase would be off. This will result in increase the actual current. After awhile the actual current would be more than reference so that the integration of error becomes zero. In the other words, the positive and negative area would be the same as each other. Then it is the time to turn the switch off until next switching cycle. It ensures having the average current equal to reference value at any switching step.

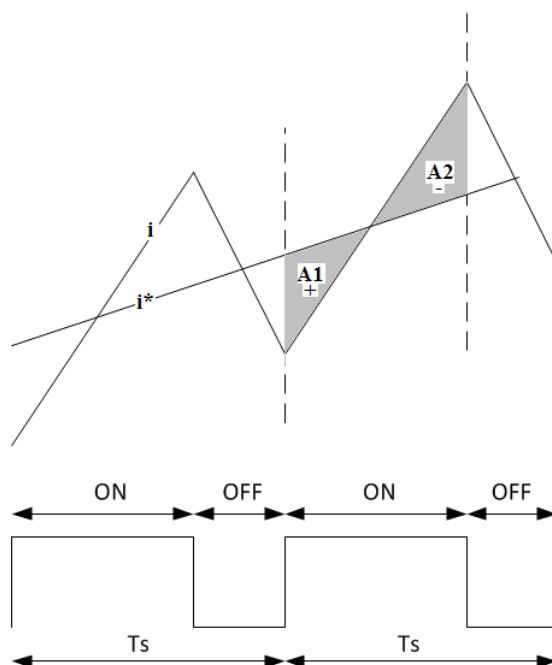


Fig 2.5.1. Reference current and possible actual current.

Three Phase four wire-rectifiers can work without any interaction between phases. However, in three wire three phase rectifier applications, just like the single phase approach, the switches would be on at the beginning of switching cycle, however putting all three phase at the same switching state may not result in the acceptable outcome. Consequently, we must only turn on two correspondent switches from two proper phases at the beginning of the switching cycle. By considering:

$$V_c = E - j\omega L I_c^* \quad (2.5.1)$$

where, V_c is the converter's voltage, E is the supply voltage, L is the inductor value, ω is the angular speed of power supply, and I_c^* is the reference current of converter. The angle of converter's voltage would be found out with straightforward calculations. Using converter's voltage angle the two proper switches might be selected from Table 2.5.1.

TABLE 2.5.1 - Switch selection table

$\angle V_c$	0-120	120-240	240-360
Sa	1	0	1
Sb	1	1	0
Sc	0	1	1

As an example, the resulting controller for phase A is shown in Fig 2.5.2.

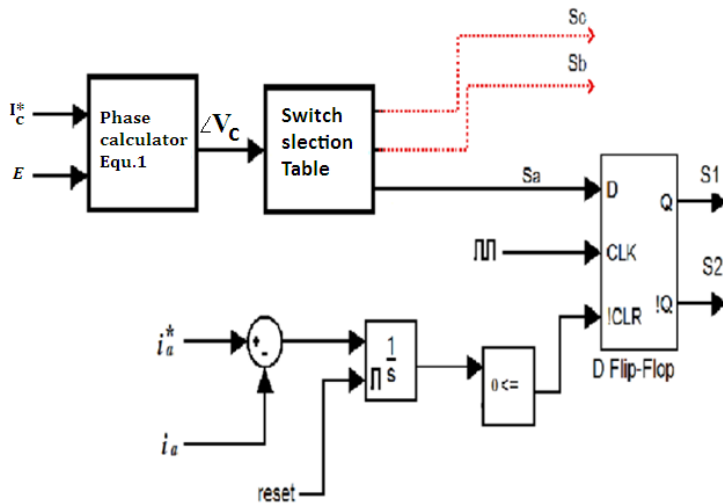


Fig 2.5.2. Current controller for phase A

To demonstrate the operation of the controller, suppose the reference vector angle is at 30 degrees. Then it lies on 0-120 degree region. As a result only S_a and S_b would be activated for the following

switching cycle. So the switching cycle starts with V_2 vector. After a short while, it is expected that current error in phase b would reach zero before phase a. So, S_3 would be off before S_1 . Then in this case the next voltage vector would be V_1 and not V_3 . After current error in phase a reaches zero S_1 would be off as well then the switching cycle ends with a null vector. The next switching cycle according to reference voltage vector a similar scenario would happen. Fig 2.5.3 graphically demonstrates the switching states during one switching cycle.

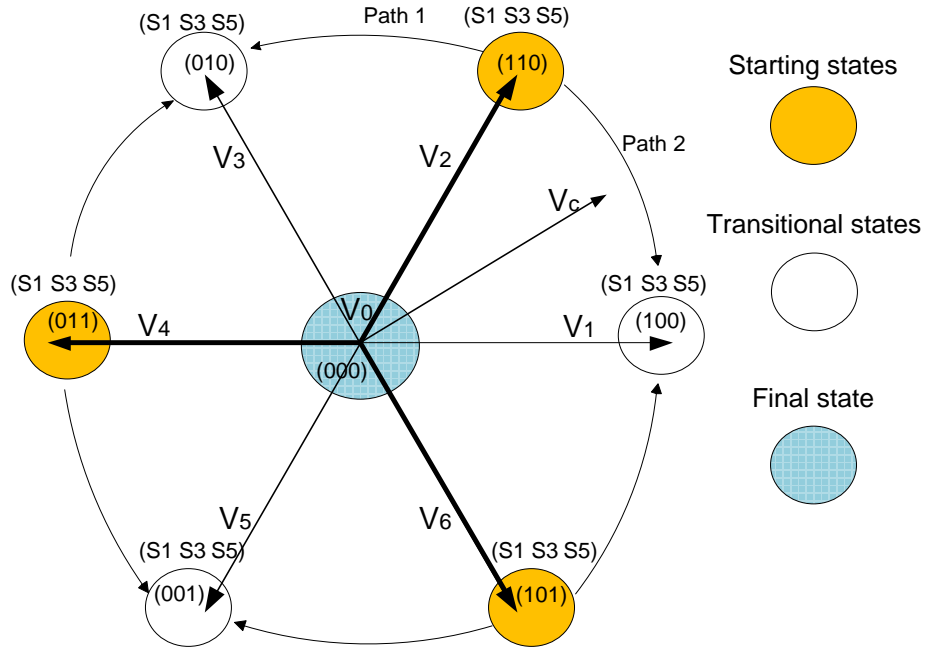


Fig 2.5.3. Graphical representation of the vector base ACC switching strategy

2.5.2. Simulation Results

Simulation has been performed to verify the validity of the proposed vector based current controller for rectifier applications.

Parameters of the simulated three-phase rectifier are listed in Table 2.5.2.

TABLE 2.5.2 - Parameters for the simulate system

Parameter	Value
Input line to line voltage	360 V/ 50Hz
Input inductors	10 mH
Dc bus voltage	600V
Switching and sampling frequencies	10 KHz

The reference current changes by a step at $t=0.03s$. Fig 2.5.4 shows the three phase currents while at $t=0.03$ there is a very short transient to reach the stable condition. Fig 2.5.5 also shows the reference and actual current of phase A. it can be seen that the actual current is very similar to reference value.

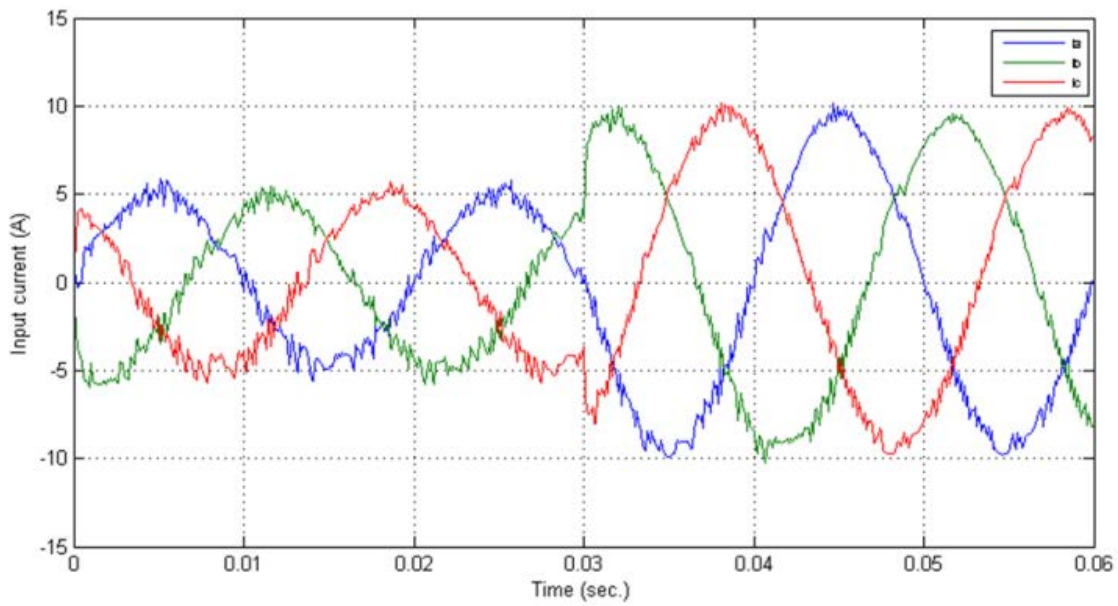


Fig 2.5.4. Three-phase input currents for SVM-based average current controller method

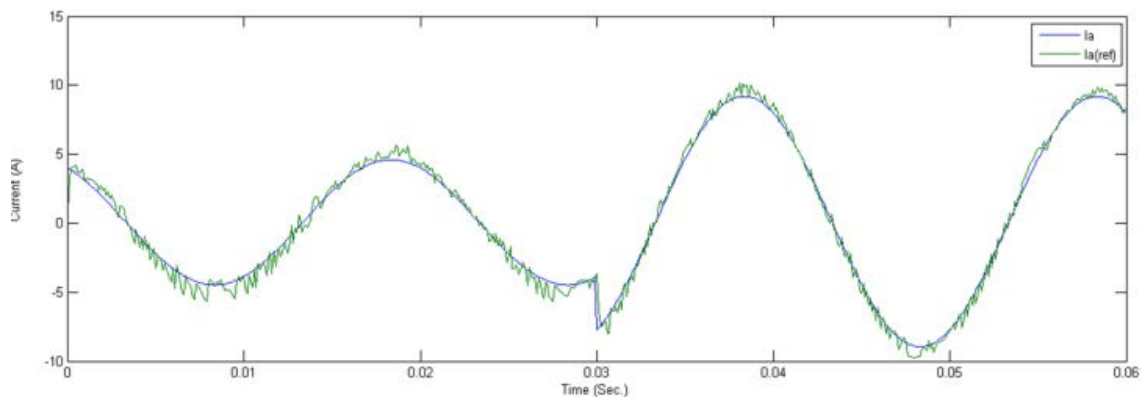


Fig 2.5.5. Input current and reference current for one phase in proposed method

2.5.3. Conclusions

In this part a new current control method with constant frequency for three-phase rectifier is presented. This controller advantages from both space vector modulation technique and average current control (ACC) strategy. The advantages are as follows:

1. This method decrease switching losses in system by keeping the switching frequency constant.
2. Its implementation is relatively simple.
3. The proposed vector-based method exhibit a very fast transient response similar to the conventional HCC.

Due to above the mentioned advantages, the method is especially suitable for high power applications with low switching frequencies i.g. input rectifier electric vehicle chargers. Simulation results show the feasibility of the purposed current controller.

2.6. Conclusions

In this chapter, GSC studied and four novel converter/ control strategies for GSC were presented. The first proposed method, *direct active power control*, is based on instantaneous dc-side current demand. In the provided solution, PLL circuit is eliminated. Computation time is reduced and high sampling rates are not required. The dynamic response is fast and transient distortions with balanced and unbalanced source voltages are negligible. High frequency current harmonics are minimal and there is no need for ferrite cores or high frequency inductors. The reference signal can be generated in a single switching cycle and there is negligible dc voltage disturbance. In this converter, unlike conventional ac-dc systems the output dc voltage can be higher or lower than the maximum value of input voltage. In the buck operating mode, smaller voltage rating of switches can be selected and high voltage supplies can operate with low voltage switches.

The second proposed method is *Improved Predictive Direct Power Control*, which offers a more accurate mathematical model to improve the performance of a recently introduced predictive direct power controller (P-DPC). The method provides a constant switching frequency and can effectively follow the active and reactive power references. The proposed controller is very fast with no steady state error which makes it especially suitable for high power applications with low switching frequencies e.g. working as GSC.

The third method is a new *fuzzy predictive direct power control (FP-DPC)* strategy, simulated and implemented using a Texas Instrument digital signal processor. While on the control loop, two separate fuzzy blocks modify the active and reactive power error signals before applying it to an improved predictive direct power control module. The idea behind this new strategy is to reduce the stress on the control system in steady state condition and also to obtain a faster transient response. The resulting controller benefits from the smoothness of conventional vector based solutions and the natural quick response of predictive methods.

The fourth method is the proposed *Average Current Control* strategy, which has a constant frequency. This controller benefits from both space vector modulation technique and average current control (ACC) strategy. The method is especially suitable for high power applications with low switching frequencies e.g. grid side converters, and rectifier of electric vehicles.

All the proposed methods have been verified by simulations or experimental results.

2.7. References

- AMBROŽIČ, V., FIŠER, R. & NEDELJKOVIĆ, D. (2003) Direct Current Control—A New Current Regulation Principle. *IEEE Trans. on Power Electronics*, 18, No. 1, 495-503.
- BOUAFIA, A., GAUBERT, J.-P. & KRIM, F. (2010) Predictive Direct Power Control of Three-Phase Pulsewidth Modulation (PWM) Rectifier Using Space-Vector Modulation (SVM). *IEEE Trans. on Power Electron.*, 25, No. 1, 228-236.
- BOWES, S. R. & MOUNT, M. J. (1981) Microprocessor control of PWM inverters. *Elec. Power Applications, IEE Proceedings*, 128 No.6, 293 - 305
- BROD, D. M. & NOVOTNY, D. W. (1985) Current Control of VSI-PWM Inverters. *IEEE Trans. on Ind. Applications*, IA-21, 562 - 570
- BROECK, H. W. V. D., SKUDELNY, H. C. & STANKE, G. (1988) Analysis and Realization of a Pulsewidth Modulator Based on Voltage - Space Vectors. *IEEE Trans. on Industry Applications*, 24 No.1, 142-150.
- HANSEN, S., MALINOWSKI, M., BLAABJERG, F. & KAZMIERKOWSKI, M. P. (2000) Sensorless Control strategies for PWM Rectifier. *IEEE APEC*.
- MALINOWSKI, M., JASIŃSKI, M. & KAZMIERKOWSKI, M. P. (2004) Simple Direct Power Control of Three-Phase PWM Rectifier Using Space-Vector Modulation (DPC-SVM). *IEEE Trans. on Ind. Electron.*, 51, No. 2 447-454.
- MALINOWSKI, M., KAZMIERKOWSKI, M. P., HANSEN, S., BLAABJERG, F. & MARQUES, G. D. (2001) Virtual-Flux-Based Direct Power Control of Three-Phase PWM Rectifiers. *IEEE TRANSACTIONS ON INDUSTRY APPLICATIONS*, 37, NO. 4, 1019-1027.
- MALINOWSKI, M., KAZMIERKOWSKI, M. P. & TRZYNADLOWSKI, A. M. (2003) A Comparative Study of Control Techniques for PWM Rectifiers in AC Adjustable Speed Drives. *IEEE Trans. on Power Electron.*, 18, No. 6, 1390-1396.
- MESBAH, M., ISLAM, S. & MASOUM, M. A. S. (2011a) A novel direct active power control method for DFIG wind turbine applications *IEEE PES ISGT*. USA.
- MESBAH, M., MASOUM, M. A. S. & ISLAM, S. (2011b) Improved Predictive Direct Power Control *Australasian Universities Power Engineering Conference (AUPEC)*. Brisbane, Australia.
- OHNISHI, T. (1991) Three Phase PWM Converter/Inverter by means of Instantaneous Active and Reactive Power Control. *IEEE IECON Proc.*
- PAN, C.-T. & CHANG, T.-Y. (1994) An Improved Hysteresis Current Controller for Reducing Switching Frequency. *IEEE Trans. on Power Electronics*, 9 No.1, 97-104.
- SUH, Y., TIJERAS, V. & LIPO, T. A. (2002) A Control Method in dq Synchronous Frame for PWM Boost Rectifier under Generalized Unbalanced Operating Conditions. *IEEE PESC Proc.*, 1425-1430.
- WU, X. H., PANDA, S. K. & XU, J. X. (2008) Analysis of the Instantaneous Power Flow for Three-Phase PWM Boost Rectifier Under Unbalanced Supply Voltage Conditions. *IEEE TRANSACTIONS ON POWER ELECTRONICS*, 23, NO. 4, 1679-1691.
- YOUN, J.-H. & KWON, B.-H. (1999) An Effective Software Implementation of the Space-Vector Modulation. *IEEE Trans. on Ind. Electron.* , 46, No. 4, 866-868.
- ZADEH, L. A. (1965) Fuzzy Sets. *Information and Control*, 8, 338-353.

Chapter 3

Rotor Side Converter (RSC)

3.1. Introduction

In DFIG, the Rotor Side Converter (RSC) is to control generated active and reactive power by generating magnetization current in the rotor windings. As shown in Fig 3.1, the RSC is a three phase full bridge inverter consists of six switches.

There are different approaches for RSC to control the DFIG. The control method for early attempts in implementation of DFIG (Pena et al., 1996) was so that the RSC would operate as a controlled voltage source and, it would regulate the current waveforms in the rotor to reach the reference active and reactive power values. For that reason, the measured three phase currents using Clarke and Park transforms would be converted to the rotating frame currents to form the actual d-q axis current signals. Then, by comparing to the respective reference values, the generated error would be applied to the PI controllers and the resulting signals would be regarded as the reference voltage values. Before applying the signal to the sinusoidal PWM module, the inverse Clarke and inverse Park transforms using mechanical position of the rotor and phase angle of the supply would be performed. The resulting system would have a constant switching frequency. However, due to use of filters in current measurements, and the time lag associated with the PI controllers it would not have a quick dynamic response.

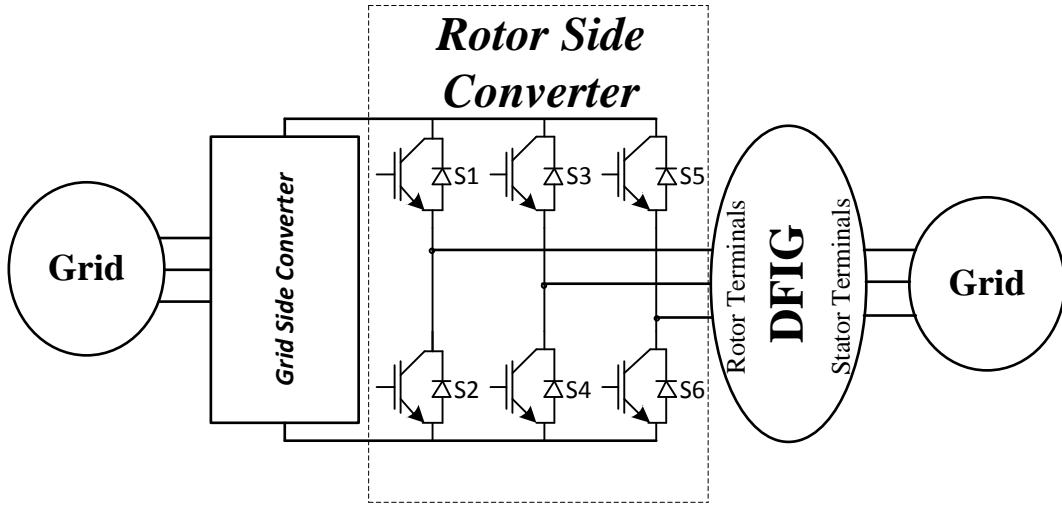


Fig 3.1 Rotor side converter schematic diagram

Direct Power Control (DPC) based methods like (Xu and Cartwright, 2006, Zhi and Xu, 2007) would provide the reference active and reactive powers at stator terminals using a proper switching table or would find the best voltage vector to be applied according to the error signal. Direct Torque Control (DTC) based methods like (Chen et al., 2011, Tremblay et al., 2011) would perform a similar task but the objective of the method is to keep the flux and electromagnetic torque at their reference

values. Nevertheless, the generated power is directly related to the mechanical speed and electromagnetic torque.

Current Control (CC) methods such as (Mohseni and Islam, 2010) normally provide a fast dynamic response. In these methods, the required reference currents would be generated without using PI controllers. For these methods, the current has to be monitored continuously. However, using micro controllers this is not practically possible. Therefore, high sampling rates are required to achieve a result similar to continuous monitoring condition. Another issue is that the samples must not be taken at switching time.

In this chapter, design and implementation of a DFIG test bench is presented. The test bench is designed such that any control strategy can be tested for comparative studies. The design is such that in measurements and data samplings, the filtering requirement is minimal. For that reason, it is possible to implement some methods that require continuous data monitoring like CC, DTC, and DPC. In addition, to verify the validity of the design and hardware setup, implementation of a CC method into the main digital controller is achieved and a number of tests are performed and the experimental results are presented.

3.2. Control Loop Design of DFIG (based on CC)

The current controlled methods inherit many advantages including fast transients. However, using microcontrollers these methods are not easy to implement. In fact high sampling rate requirements and noise interferences are the most important burdens against implementation of these methods. However improvements in Microcontrollers and DSP systems enable us to have high sampling rates and short processing time.

To generate the reference values, analysis of the electrical model of the system is required. The machine model might be expressed as:

$$V_s = j\omega\Psi_s + \dot{\Psi}_s + I_s R_s \quad (3.1)$$

$$V_r = j(\omega - \omega_r)\Psi_r + \dot{\Psi}_r + I_r R_r \quad (3.2)$$

Also, the flux might be approximated by:

$$\psi_s = \int v_s dt \quad (3.3)$$

$$\psi_r = \int v_r dt \quad (3.4)$$

And, from the currents:

$$\psi_r = L_r I_r + L_m I_m \quad (3.5)$$

$$\psi_s = L_s I_s + L_m I_m \quad (3.6)$$

According to (3.3) the stator flux is related to stator voltage and not the stator current.

Also:

$$I_s = I_m - I_r \quad (3.7)$$

In stator frame d-q axis, by neglecting the effect of resistors in the model will cause to have all magnetization current in q-axis then:

$$I_{sd} = -I_{rd} \quad (3.8)$$

$$I_{sq} = I_{mq} - I_{rq} \quad (3.9)$$

As it stated earlier the stator magnetization is directly related to stator voltage so it is fair to consider that I_r will not affect magnetization current significantly. Then:

$$I_{mq} = \frac{E_{sd}}{L_s \omega} \quad (3.10)$$

In the current control approaches the reference active and reactive powers would form the reference currents. The active and reactive output power might be calculated as:

$$P_s = E_{sd} I_{sd} \quad (3.11)$$

$$Q_s = E_{sd} I_{sq} \quad (3.12)$$

From (3.8) and (3.11)

$$P_s = -E_{sd} I_{rd} \quad (3.13)$$

And from (3.9), (3.10) and (3.12)

$$Q_s = \frac{E_{sd}^2}{L_s \omega} - E_{sd} I_{rq} \quad (3.14)$$

So, using (3.13) and (3.14) the reference rotor currents might be found from the reference active and reactive powers:

$$I_{rd}^* = \frac{-P^*}{E_{sd}} \quad (3.15)$$

$$I_{rq}^* = \frac{-Q^*}{E_{sd}} + \frac{E_{sd}}{L_s \omega} \quad (3.16)$$

From (3.15) and (3.16) any reference power value would project its equivalent reference rotor current. However, this reference is in stator axis frame to find the reference values in rotor frame:

$$\begin{bmatrix} i_{rd} \\ i_{rq} \end{bmatrix} = n \begin{bmatrix} I_{rd} \\ I_{rq} \end{bmatrix} \quad (3.17)$$

where, n is the turn ratio of the stator to rotor windings and might be measured when the rotor is open-circuit and the

$$\begin{bmatrix} i_{rd} \\ i_{rq} \end{bmatrix} = \begin{bmatrix} \sin(\theta - \theta_r) & \cos(\theta - \theta_r) \\ \cos(\theta - \theta_r) & -\sin(\theta - \theta_r) \end{bmatrix} \begin{bmatrix} i_{r\alpha} \\ i_{r\beta} \end{bmatrix} \quad (3.18)$$

From (3.17) and (3.18):

$$\begin{bmatrix} i_{r\alpha}^* \\ i_{r\beta}^* \end{bmatrix} = n \begin{bmatrix} \sin(\theta - \theta_r) & \cos(\theta - \theta_r) \\ \cos(\theta - \theta_r) & -\sin(\theta - \theta_r) \end{bmatrix} \begin{bmatrix} I_{rd}^* \\ I_{rq}^* \end{bmatrix} \quad (3.19)$$

and,

$$\begin{bmatrix} i_{ra}^* \\ i_{rb}^* \\ i_{rc}^* \end{bmatrix} = \sqrt{\frac{2}{3}} \begin{bmatrix} 1 & 0 \\ -\frac{1}{2} & \frac{\sqrt{3}}{2} \\ -\frac{1}{2} & -\frac{\sqrt{3}}{2} \end{bmatrix} \begin{bmatrix} i_{r\alpha}^* \\ i_{r\beta}^* \end{bmatrix} \quad (3.20)$$

The resulting reference currents and usage of a hysteresis controller could generate the required switching pulses. However to avoid DC-bus short circuit a dead band is required to switch off both switches of one arm in transition from one state to another. Due to importance of the dead band it is better to implement it in hardware. Fig.3.2 shows the control loop of the resulting system.

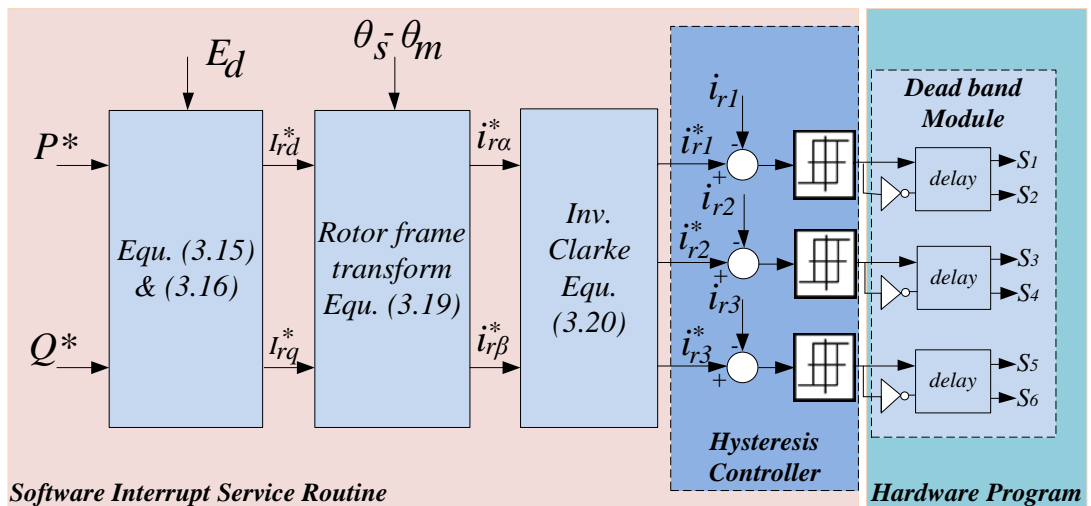


Fig.3.2 The Control loop of the DFIG for CC based method

3.3. Hardware Requirements and Solutions

3.3.1 Overall system structure

Fig 3.3 shows the schematic of the proposed real time digital simulation system. In the speed range up to the synchronous speed, the power delivery is from the dc bus to the rotor. To simplify the circuit the Grid-side converter can be replaced by an H-bridge diode rectifier. So, the design work focus on rotor side converter. The idea is to design the system so that any control method can be easily tested and verified. As it is shown in Fig 3.3 there are seven analog signals plus the position must be acquired and processed for control purposes. The variable nature of the wind is simulated through a

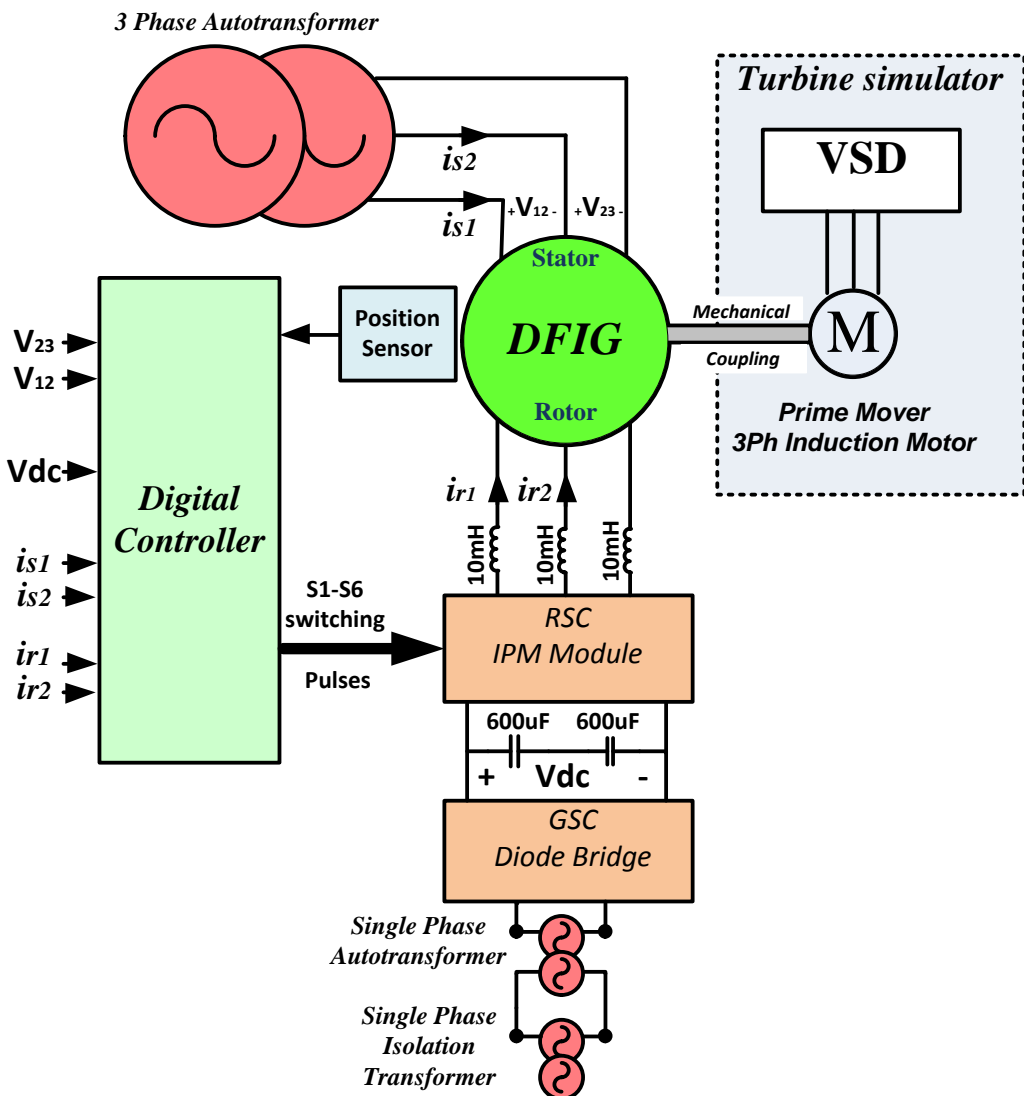


Fig 3.3 Schematic of the proposed Real Time Digital Simulation of DFIG WTG

variable speed drive Micro Master 440 in conjunction with an induction motor. The system is aimed to operate at sub-synchronous speeds. At sub-synchronous speeds the direction of power delivery in steady state is always from the DC bus to the rotor. As the main or in some cases the only purpose of

the grid side converter is to provide DC bus voltage for this operating condition the GSC is in this case is replaced with a simple diode bridge rectifier. A similar approach has also been previously reported in (Lipo, 2009) while replacing rotor side converter with a diode bridge in super synchronous speeds for laboratory testing purposes. However, the aim of our approach is to have a simple system focusing on the rotor side converter control to evaluate the performance of the machine in different operating condition rather than analysing overall output power and power quality.

3.3.2 Controller selection

In order to implement any control algorithm, employment of a digital controller is a must. Based on complexity of the control system the required controller will need to be selected appropriately. Needless to say, most of the companies who are involved in manufacturing the semiconductors, they all provide similar products to respond to the high volume of demand to motor control or power electronics related application market. Regardless of architectural differences, Digital Signal Processors (DSP) are CPU based chips doing similar job as microcontrollers. The difference is that they normally operate with a faster system clock and also they may have dedicated hardware for a specific application. These modules would operate separately from the main processor of DSP. As a result, it helps to have less programming code size to improve overall system performance. To find the right DSP, one has the choice of the floating point DSPs as well as fixed point options. Fixed point DSPs are normally cheaper but they need more code size and more time when dealing with float point numbers. However, considering the cost of the overall system design for motor control applications the extra cost of floating point DSPs is negligible. TMS320F28335 is a floating point digital signal processor from Texas Instruments which is suitable for implementation of most of the control methods. This DSP provide 16 channels of 12-bit analog to digital converter. However, the input signals must be within the measuring range of 0V-3V. So, taking 1.5V as offset makes it possible to measure the negative signals as well as positive signals. Moreover, the current and voltage signals must be converted so that they fit within the measuring range. For this reason the current and voltage sensor circuits should be designed to meet the requirements.

3.3.3 Current Measurement Circuit

For current measurements the Hall Effect current transducers using a 100Ω resistor would make it possible to sense voltage within the range of (-3V to +3V) for currents up to 30 Ampere. To be able to sense negative signals as well as positive ones, a level shifter circuit is required to fit the signal into measuring range of the DSP. The level shifter circuit also can remove very high frequency signals or noises that are not welcomed in a power electronic circuit. The ADC module of DSP generates high frequency switching noises that may affect the operation of a level shifter. So to feed the resulting signal to DSP, analog inputs are passed through a low-pass filter and high Frequency buffer circuit is

placed after the level shifter circuit. The detailed circuit diagram for current measurements is shown in Fig 3.4(a).

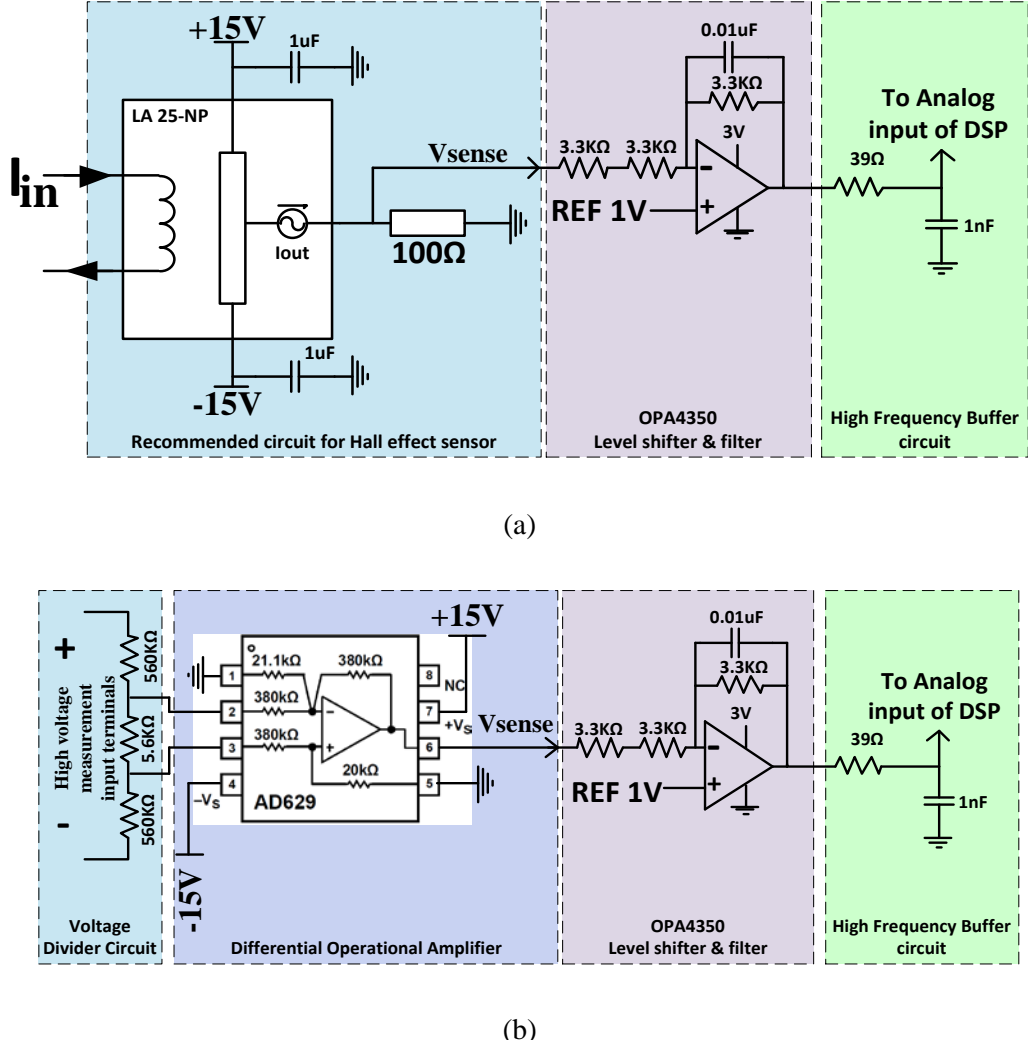


Fig 3.4 Circuit diagram for (a) current (b) voltage measurements

3.3.4 Voltage Measurement Circuit

The same level shifter and buffer circuit shall be employed to get voltage measurements. However, the voltage measurement is better to detect a voltage between two terminals rather than comparing one terminal to a reference value. As a result the detector circuit is to be designed based on a differential operational amplifier. Moreover, the high voltage should be stepped down using a voltage divider circuit. This way the high voltages cannot appear at chip terminals in case of device failure. The voltage divider circuit brings the actual voltage within the range of (-3V to +3V). Also using a symmetrical design for the configuration of the resistors, high common-mode voltages could not affect circuit operation. For this design application voltage divider values are required to measure the

line to line voltages up to 425V or DC-bus voltage up to 600 volts. The detailed circuit diagram for voltage measurements is shown in Fig 3.4(b).

3.3.5 Digital IOs

The digital input/outputs of this particular DSP are 3.3V and are not 5 V tolerant. However, 5V IOs are required for communication to Intelligent Power Modules (IPMs). For this reason to increase the high level voltage of the DSP from 3.3V to 5V a simple digital buffer that accept 2V as high would be employed to convert output signals. Also for digital inputs the 5V signals would be stepped down using a resistive voltage divider. A key to design digital circuit is that, to have a more reliable system the PWM digital outputs shall turn the switches off in the case of a low output signal. This helps not to lose the switches in the case of programming faults or controller's power failure.

3.3.6 Resulting Designed Board

The manufactured board is also shown in the Fig 3.5. As it is clear in the figure the power terminals for current and voltage are located at left hand side of the board, which helps to have separation of high voltage side and low voltage side, plus easy and safe access to the circuit terminals. The PWM outputs are located at right hand side of the board. This makes it possible to have an acceptable clearance between low voltage and high voltage circuits.

3.3.7 Intelligent Power Modules

The rotor side converter (RSC) is implemented using PM75CL1A120 Mitsubishi IPM modules. These modules provide detection, protection and status indication circuits for short-circuit, over-temperature and under-voltage. Also the related interface modules provide the optical isolation which allows a safe connection to the digital controller.

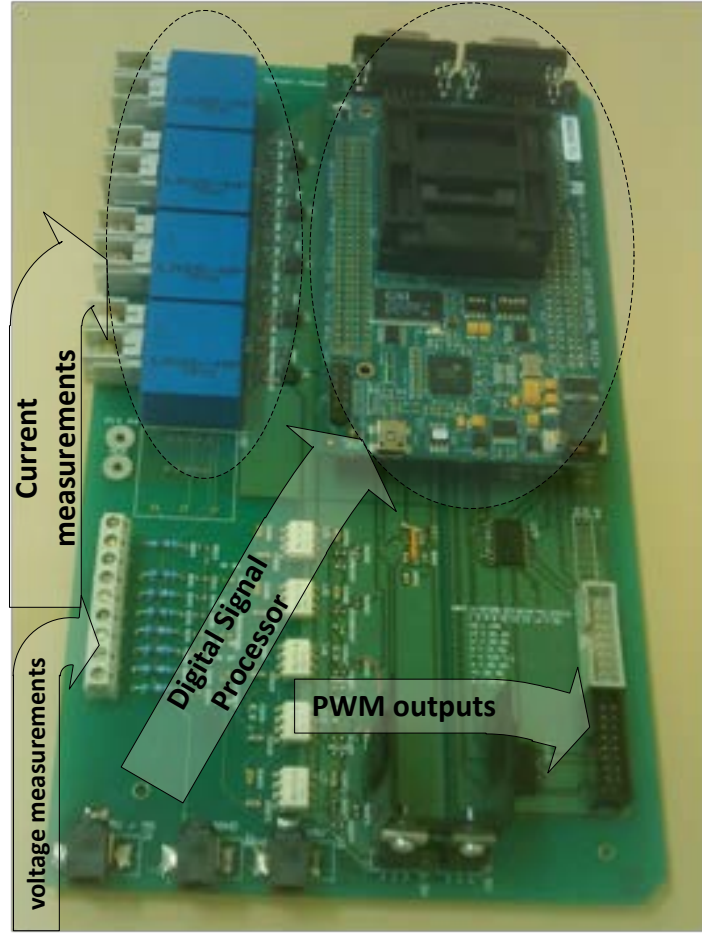


Fig 3.5 Signal conditioner board

3.4. Some Practical Considerations

3.4.1 Data samples

Samples must be captured with a specific period and not at the very moments of switching to avoid electromagnetic noise that would cause false readings. In DSP used here, ADC module runs separately from the main CPU. It might be adjusted either to run continuously without considering the circuit condition or wait for the PWM module to generate the start of conversion (SOC) signal. Theoretically, the sampling rate of signal may go up to 25MHz for a single channel. However, due to the limitations of most control programs the sampled data update cannot be done faster than 125 kHz. In the case of continuous run using high sampling rates in conjunction with implementation of software, finite impulse response (FIR) filters, there is always a time delay involved in the readings that may affect the control loop. In addition, noisy samples that are taken at the very moments of state change of power switches will decrease the accuracy of data and these will affect the operation of the system in general. In fact, the results of such measurements are not acceptable for most of control methods. As an experience the best way of performing measurements is to set PWM modules to

generate the SOC pulses when the PWM timer is reset. This will result in precisely timed data samples.

3.4.2 Switching when using variable frequency switching methods

Switching frequency in some control methods like hysteresis and DPC is not constant but it is necessary to limit the maximum switching frequency under 20kHz for the sake of safe operation of IPM modules. As a result the sampling frequency must not exceed 40 kHz. Moreover, in order to suppress the effect of electromagnetic noise in the readings, the switching must not happen at very moments of ADC conversion.

Due to the above mentioned requirements, it is better to preset the PWM interrupts to update the switching states when the PWM timer is at the half way through timing period. Fig.3.6 shows the possible solution while using variable frequency switching methods.

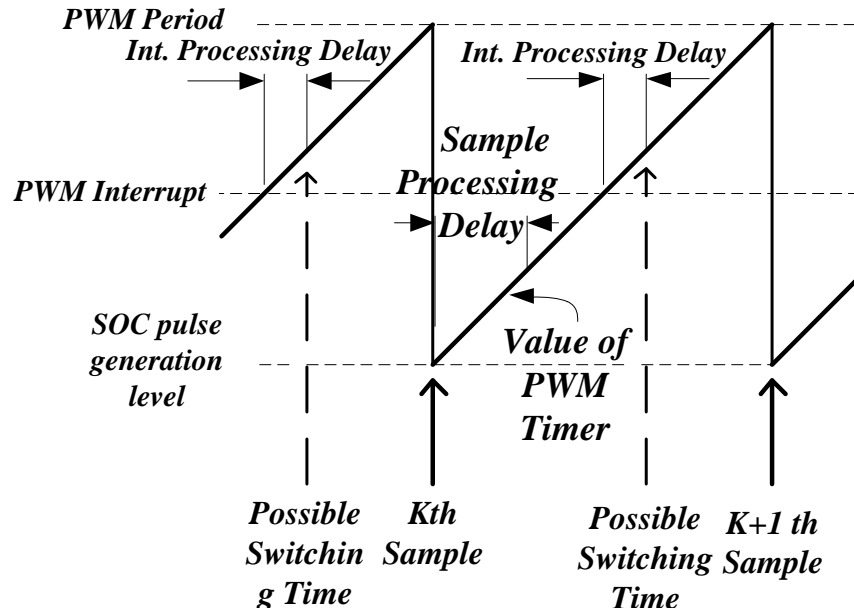


Fig 3.6. Data sample timing for variable switching frequency methods

3.5. Experimental Results

The system is assembled as shown in Fig 3.3. The DFIG test bench is shown in Fig 3.7. Due to relatively high turn ratio of the rotor the DC bus voltage is adjusted approximately around 60 volts. The shaft speed is controlled by the AC drive and it is kept constant at 1470 rpm to provide a 1Hz slip.

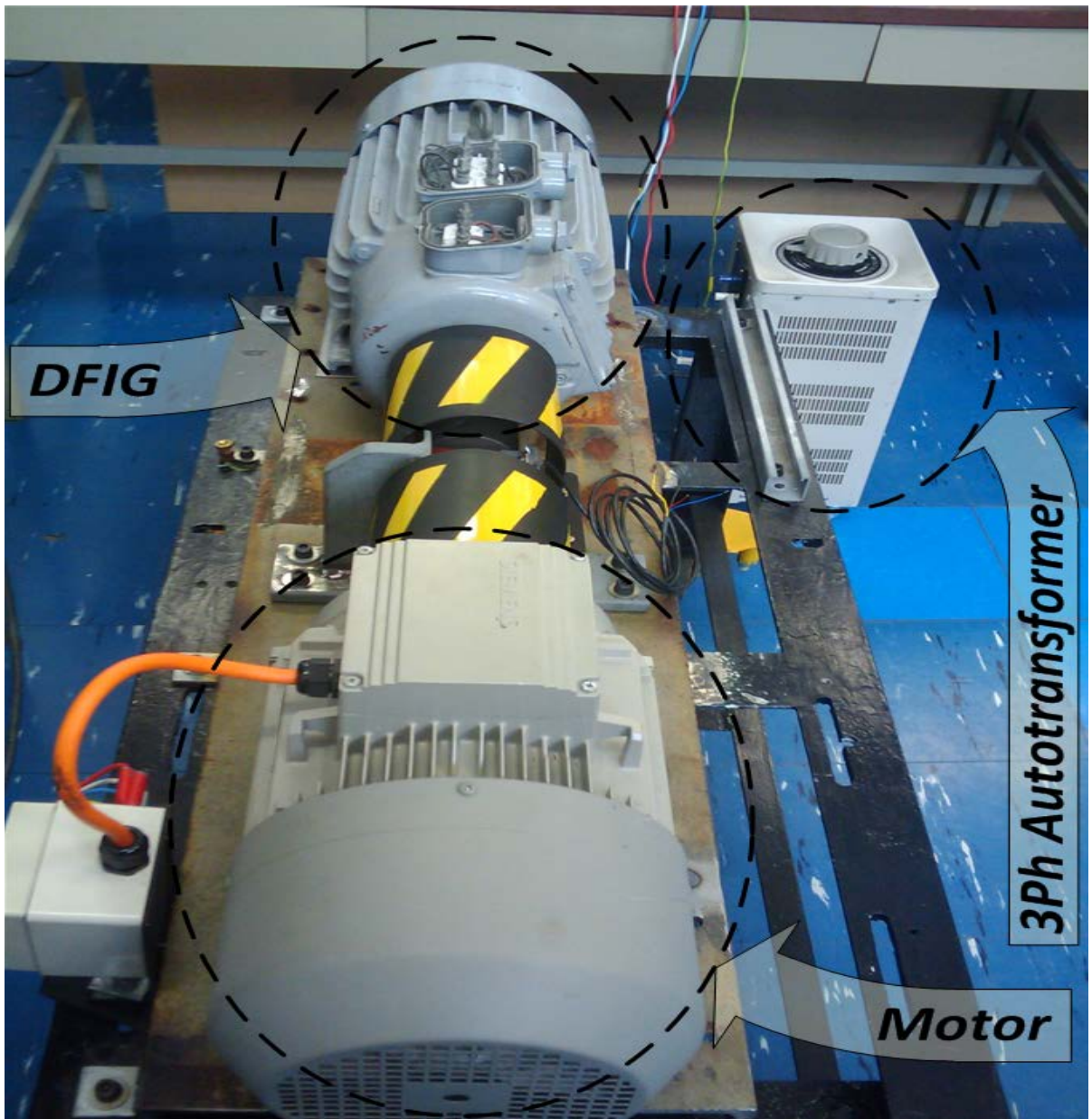


Fig 3.7 The DFIG in the test bench

The tests are performed so that steady-state response and transient response of DFIG could be verified.

For steady-state reference the generated active and reactive power are kept constant at 300W and “0”VAR respectively. The rotor currents are shown in Fig 3.8 and the stator voltage and current waveforms are shown in the Fig 3.9. Table 3.1 shows the harmonic content of phase A of the stator. The THD is recorded as 3.8%. The operation of the generator using the CC technique was flawless.

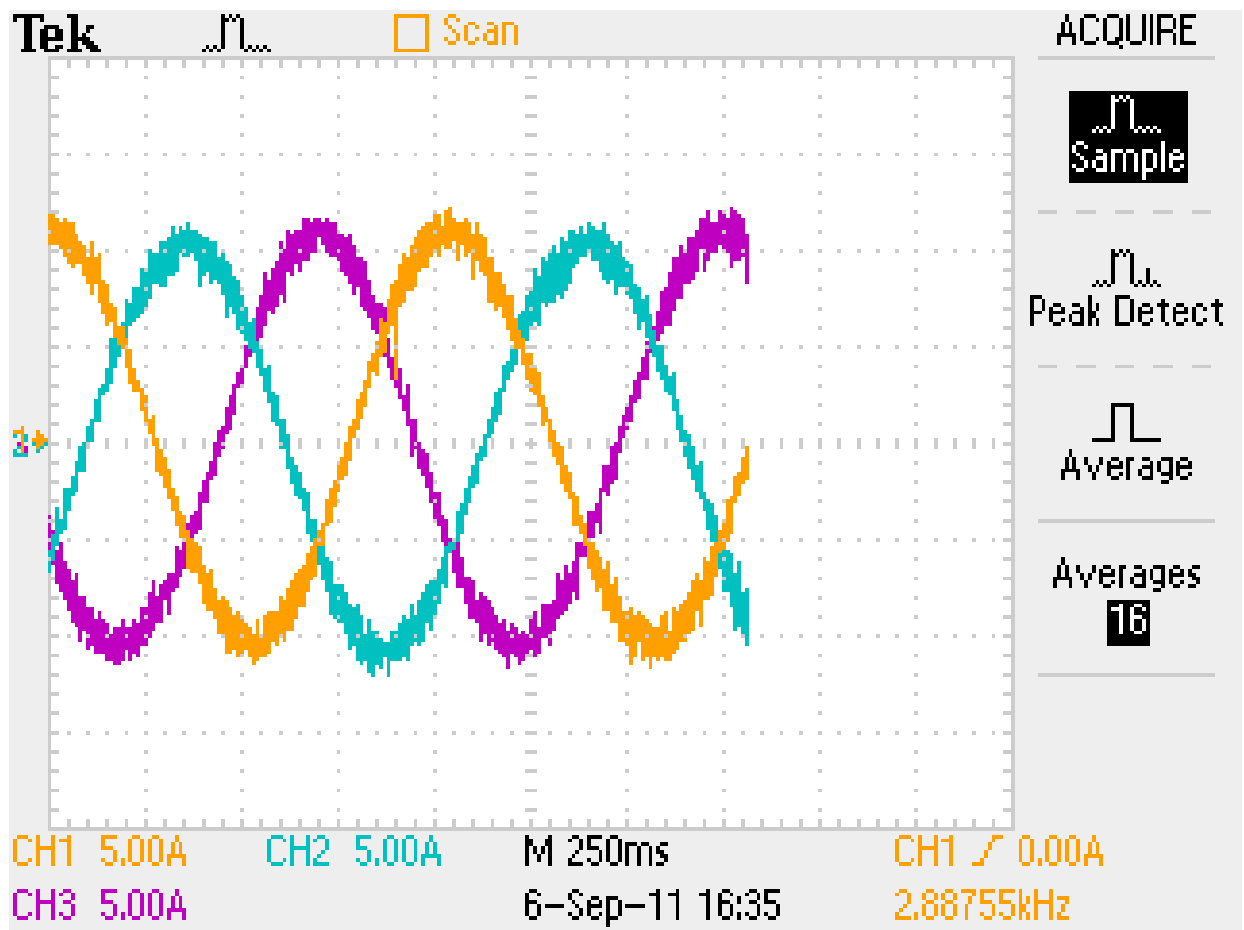


Fig 3.8 Steady-state experimental results: rotor currents

For transient tests reference power would jump from 300W to 600W. The rotor currents are shown in Fig 3.10 and the stator voltage and current waveforms are shown in the Fig 3.11.

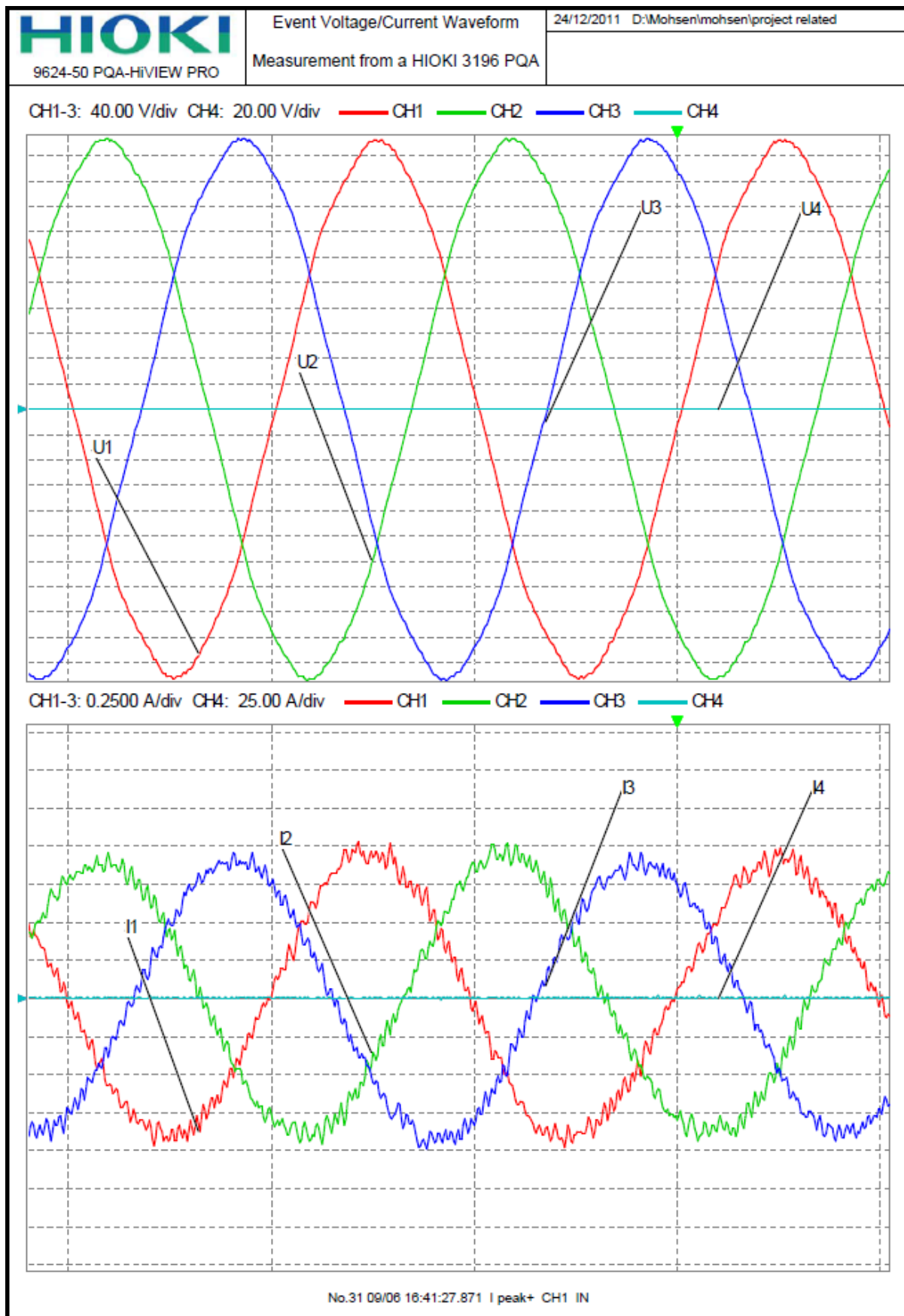


Fig 3.9 Steady-state experimental results: stator voltage and current waveforms

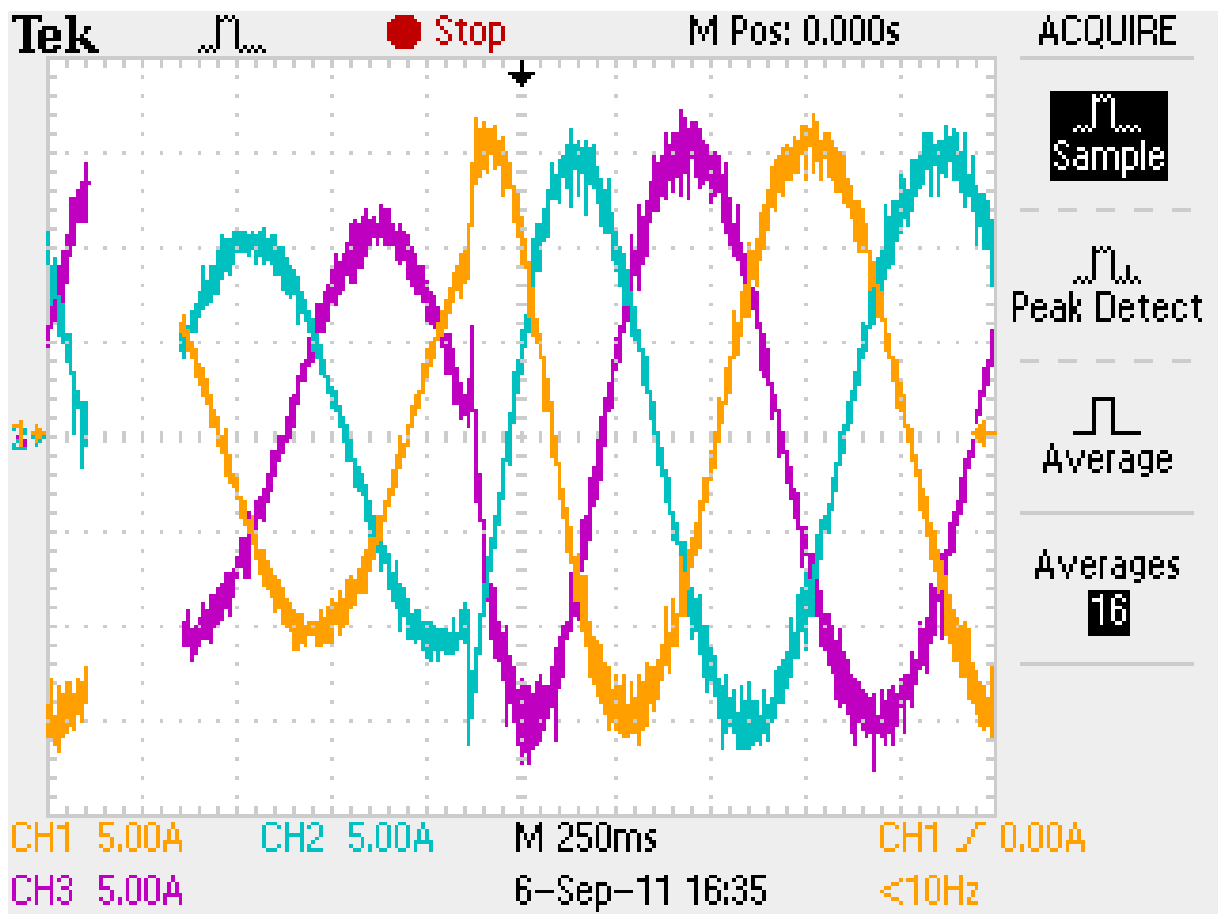


Fig 3.10 Transient experimental results: rotor currents

This is clear that the hysteresis controller acts very quickly to provide the reference current values.

In a separate test, just to experiment the DFIG response to different reactive power demands, the reference reactive power has changed from 300VAR to 750VAR while the active power has set to 0W. The resulting stator voltage and current waveforms are shown in Fig 3.12 . It can be seen that the quick response of the controller provides the required magnetization current to generate the requested reference reactive power.

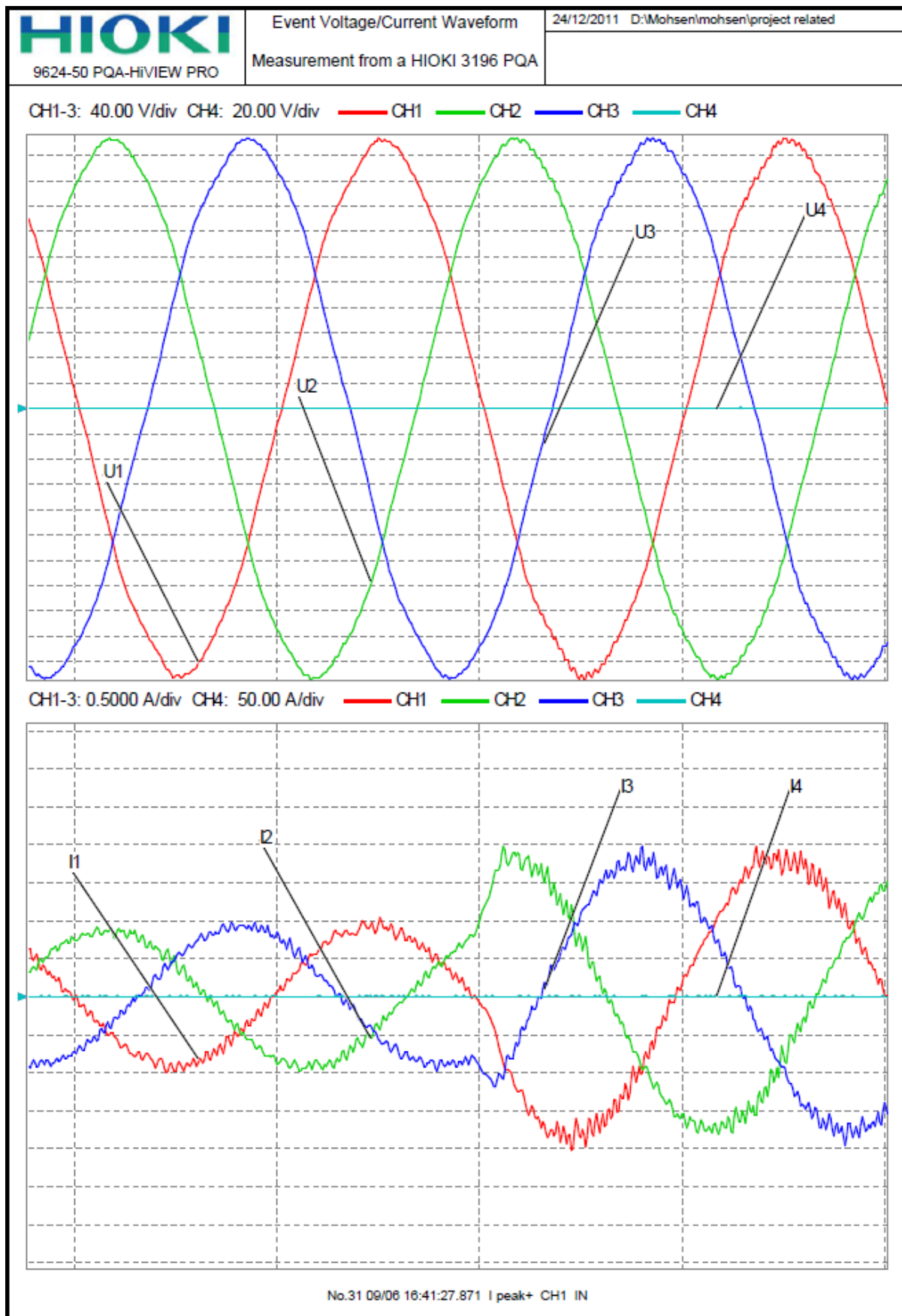
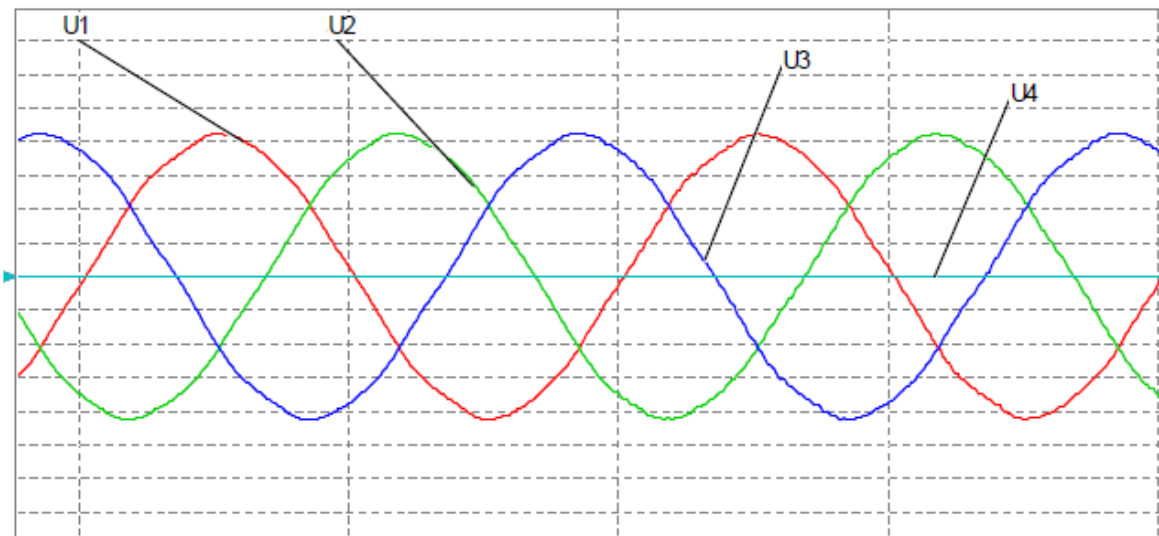


Fig 3.11 Transient experimental results: stator voltage and current waveforms

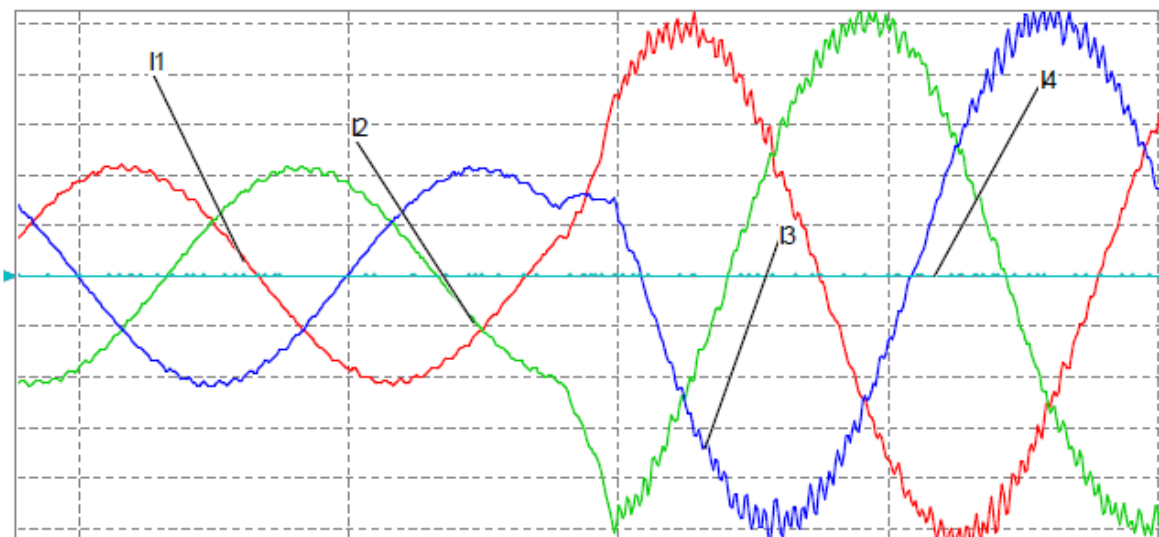
TABLE 3.1 - experimental results: harmonic content of Phase A stator current

 9624-50 PQA-HiVIEW PRO		Event Harmonic List		24/12/2011 D:\Mohsen\mohsen\project related																																																																																																													
		Measurement from a HIOKI 3196 PQA																																																																																																															
CH1 VALUE iHarm OFF																																																																																																																	
<table border="1" style="width: 100%; border-collapse: collapse;"> <thead> <tr> <th>Order</th><th>(A)</th><th>Order</th><th>(A)</th><th>Order</th><th>(A)</th></tr> </thead> <tbody> <tr><td>1</td><td>0.8747</td><td>18</td><td>0.0032</td><td>35</td><td>0.0048</td></tr> <tr><td>2</td><td>0.0174</td><td>19</td><td>0.0023</td><td>36</td><td>0.0033</td></tr> <tr><td>3</td><td>0.0157</td><td>20</td><td>0.0025</td><td>37</td><td>0.0028</td></tr> <tr><td>4</td><td>0.0063</td><td>21</td><td>0.0031</td><td>38</td><td>0.0025</td></tr> <tr><td>5</td><td>0.0090</td><td>22</td><td>0.0021</td><td>39</td><td>0.0036</td></tr> <tr><td>6</td><td>0.0051</td><td>23</td><td>0.0027</td><td>40</td><td>0.0024</td></tr> <tr><td>7</td><td>0.0036</td><td>24</td><td>0.0012</td><td>41</td><td>0.0025</td></tr> <tr><td>8</td><td>0.0045</td><td>25</td><td>0.0020</td><td>42</td><td>0.0032</td></tr> <tr><td>9</td><td>0.0041</td><td>26</td><td>0.0020</td><td>43</td><td>0.0036</td></tr> <tr><td>10</td><td>0.0036</td><td>27</td><td>0.0022</td><td>44</td><td>0.0038</td></tr> <tr><td>11</td><td>0.0047</td><td>28</td><td>0.0021</td><td>45</td><td>0.0039</td></tr> <tr><td>12</td><td>0.0045</td><td>29</td><td>0.0036</td><td>46</td><td>0.0021</td></tr> <tr><td>13</td><td>0.0013</td><td>30</td><td>0.0037</td><td>47</td><td>0.0026</td></tr> <tr><td>14</td><td>0.0019</td><td>31</td><td>0.0024</td><td>48</td><td>0.0045</td></tr> <tr><td>15</td><td>0.0028</td><td>32</td><td>0.0020</td><td>49</td><td>0.0020</td></tr> <tr><td>16</td><td>0.0030</td><td>33</td><td>0.0016</td><td>50</td><td>0.0039</td></tr> <tr><td>17</td><td>0.0040</td><td>34</td><td>0.0033</td><td>THD</td><td>3.84 (%)</td></tr> </tbody> </table>						Order	(A)	Order	(A)	Order	(A)	1	0.8747	18	0.0032	35	0.0048	2	0.0174	19	0.0023	36	0.0033	3	0.0157	20	0.0025	37	0.0028	4	0.0063	21	0.0031	38	0.0025	5	0.0090	22	0.0021	39	0.0036	6	0.0051	23	0.0027	40	0.0024	7	0.0036	24	0.0012	41	0.0025	8	0.0045	25	0.0020	42	0.0032	9	0.0041	26	0.0020	43	0.0036	10	0.0036	27	0.0022	44	0.0038	11	0.0047	28	0.0021	45	0.0039	12	0.0045	29	0.0036	46	0.0021	13	0.0013	30	0.0037	47	0.0026	14	0.0019	31	0.0024	48	0.0045	15	0.0028	32	0.0020	49	0.0020	16	0.0030	33	0.0016	50	0.0039	17	0.0040	34	0.0033	THD	3.84 (%)
Order	(A)	Order	(A)	Order	(A)																																																																																																												
1	0.8747	18	0.0032	35	0.0048																																																																																																												
2	0.0174	19	0.0023	36	0.0033																																																																																																												
3	0.0157	20	0.0025	37	0.0028																																																																																																												
4	0.0063	21	0.0031	38	0.0025																																																																																																												
5	0.0090	22	0.0021	39	0.0036																																																																																																												
6	0.0051	23	0.0027	40	0.0024																																																																																																												
7	0.0036	24	0.0012	41	0.0025																																																																																																												
8	0.0045	25	0.0020	42	0.0032																																																																																																												
9	0.0041	26	0.0020	43	0.0036																																																																																																												
10	0.0036	27	0.0022	44	0.0038																																																																																																												
11	0.0047	28	0.0021	45	0.0039																																																																																																												
12	0.0045	29	0.0036	46	0.0021																																																																																																												
13	0.0013	30	0.0037	47	0.0026																																																																																																												
14	0.0019	31	0.0024	48	0.0045																																																																																																												
15	0.0028	32	0.0020	49	0.0020																																																																																																												
16	0.0030	33	0.0016	50	0.0039																																																																																																												
17	0.0040	34	0.0033	THD	3.84 (%)																																																																																																												
No.31 09/06 16:41:27.871 peak+ CH1 IN																																																																																																																	

CH1-3: 100.00 V/div CH4: 50.00 V/div —— CH1 —— CH2 —— CH3 —— CH4



CH1-3: 0.5000 A/div CH4: 50.00 A/div —— CH1 —— CH2 —— CH3 —— CH4



No.20 09/06 16:42:46.607 | peak+ CH1 IN

Fig 3.12 Reactive power generation

3.6. Conclusions

In this chapter a real time digital control of the Rotor Side Converter (RSC) of a DFIG system is presented. Design aspects and real time simulation is presented. The setup is particularly useful to study various control techniques for DFIG wind turbines. Therefore, the technique will be very suitable to study the grid code compatibility of DFIG wind energy conversion systems. The control algorithm is scalable for larger machines. In this chapter, details of a current controlled (CC) method as an example is implemented and verified by a number of experiments to test the controller's steady state and transient performances. The experimental results show that using proper rotor current magnitude, the DFIG is capable to vary both active and reactive power generation from a DFIG wind power conversion system.

3.7. References

- CHEN, S. Z., CHEUNG, N. C., WONG, K. C. & WU, J. (2011) Integral variable structure direct torque control of doubly fed induction generator. *IET Renew. Power Gener.*, 5, 18-25.
- LIPO, T. A. (2009) A Supersynchronous Doubly Fed Induction Generator Option for Wind Turbine Applications. *IEEE PEMWA Lincoln*.
- MOHSENI, M. & ISLAM, S. (2010) A New Vector-Based Hysteresis Current Control Scheme for Three-Phase PWM Voltage-Source Inverters. *IEEE Trans. On Power Electronics*, 25, no. 9, 2299-2309.
- XU, L. & CARTWRIGHT, P. (2006) Direct Active and Reactive Power Control of DFIG for Wind Energy Generation. *IEEE trans. on Energy Conversion*, 21, NO. 3, 750-758.
- ZHI, D. & XU, L. (2007) Direct Power Control of DFIG With Constant Switching Frequency and Improved Transient Performance. *IEEE TRANSACTIONS ON ENERGY CONVERSION*, 22, NO. 1, 110-118.

Chapter 4

Fault Simulator

4.1. Introduction

In wind farms, the transformers are one of the most essential components that can be affected by various types of faults. In general, the distances between wind turbines are not short while all turbines connect to the internal power network within the farm by means of medium voltage cables just to minimize the power loss. However, the generators typically work with low voltages; therefore, that is the role of the transformers to connect the LV wind turbines to the MV grid. It is the transformer that is most susceptible to three phase faults which is most catastrophic of all. It is quite common that the wind farms are located at remote part of a MV grid which is exposed to power quality problems i.e. voltage sag.

Fig 4.1 shows the fault ride-through capability of wind farms according to grid code that ensures maintaining the current level of network dynamic stability (Ackermann et al., 2007). It is clear from the Fig. 4.1, voltage sags of 15% on any phase must be tolerated for about 600 milliseconds, and that is 30 power cycles. This voltage sag may affect the operation of the generator as well as the transformer. In fact, it may cause several issues like inrush currents or dc bias in transformers that need to be investigated as well as impact on wind power generation.

Moreover, the ability to recreate accurate and realistic fault transients imposed upon actual power system components is highly desirable for improving equipment design and developing effective protection countermeasures. Such studies are also useful in understanding the transient operation of many electrical machines such as induction motors, synchronous machines, transformers, circuit breakers, capacitor banks, wind power plants and many other network assets (Iravani et al., 1995, Fuchs and Masoum, 2008).

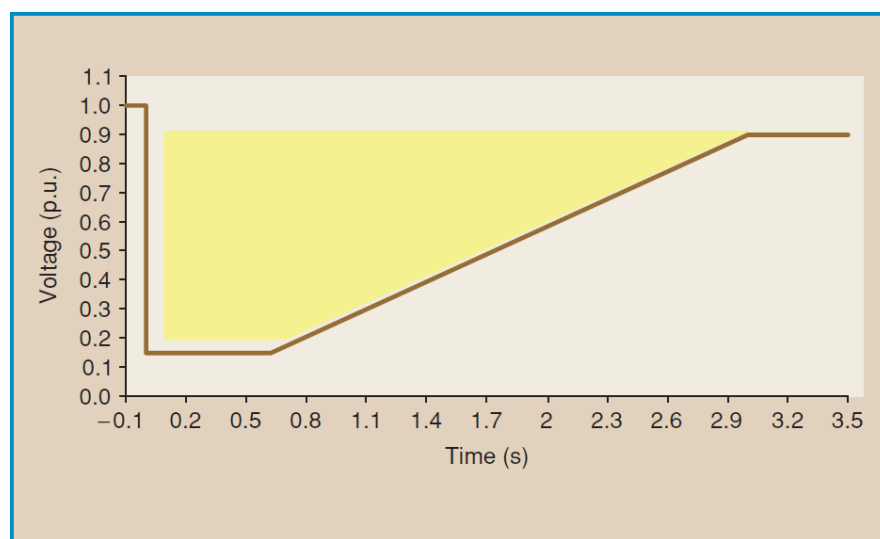


Fig 4.1. Fault ride-through capability of wind farms according to grid code

For testing the impact of various disturbances, this chapter proposes a prototype of a new multi-purpose fault generator capable of injecting various types of controllable disturbances and fault transients. The three phase power supply fault simulator is implemented using a three phase dc to ac converter. Based on a space vector modulation (SVM) approach the converter is capable of generating a variety of three-phase power supply faults and disturbances including voltage sag, swell, voltage unbalance, harmonics, dc-bias, phase jump and etc. The application of this hardware simulator in the testing of transient operation conditions in three-phase power transformers is demonstrated.

More specifically, this chapter focuses on the transient operation of power transformers and how their behaviour can be symptomatic of external disturbances of the surrounding system. Power transformers are vital ubiquitous links in transmission and distribution systems very much exposed to several types of faults and disturbances frequently occurring throughout the network. Therefore, the proposed hardware simulator will subject a selected transformer to different types of faults and investigate its performance.

One of the most common types of faults which severely impact transformer operation is the short duration voltage sag that is typically present at the transformer terminals during a network fault upstream (Masoum et al., 2010). The sudden voltage recovery upon fault clearance can generate magnetic fluxes in the magnetic core beyond rated conditions resulting in core saturation (Bollen, 2003, Styvaktakis and Bollen, 2003). Large magnetizing currents similar to the inrush current phenomenon can occur in the transformer windings (Sainz et al., 2007, Cardelli et al., 2009). Thus this behaviour is very sensitive to the iron-core ferromagnetic characteristics (e.g., hysteresis and saturation) as well as the point-on-wave instants on the voltage waveform that the sag occurs and recovers.

References (Pedra et al., 2005, Styvaktakis and Bollen, 2003, Masoum et al., 2010) have conducted simulation studies on the impacts of symmetrical and unsymmetrical voltage sags on the current peaks of three-phase transformers. However, no controlled experimental studies of this phenomenon have been offered previously due to the lack of precise and controllable fault emulation hardware. The prototype hardware simulator proposed here is therefore applied to the experimental study of a three-phase three-leg transformer subjected to various fault conditions.

The hardware fault simulator prototype is described in full detail and its application to the investigation of transformer transient operating behaviour is demonstrated for symmetrical and unsymmetrical faults subjected to the transformers terminals. The application to three-phase transformer testing is particular interesting since the ferromagnetic nonlinearities, asymmetry in the transformer core structure (e.g., three-leg, five-leg designs) and inherent magnetic flux couplings exhibited by the core-legs all play a significant part in the not-so-well known transient behaviour in currents, mmfs and magnetic fluxes under various fault conditions (Moses et al., 2010, Moses et al., 2011). In this chapter, experimental study is

carried out for a $440\sqrt{3} / 55\sqrt{3}$ V three-phase three-leg transformer which is supplied from the fault generator serving as the distribution grid subjected to typical network disturbances.

4.2. Fault Emulator Hardware Prototype

The three phase fault emulator configuration is shown in Fig 4.2. The fault emulator is based on a modified three phase dc-ac converter. Using space vector modulation any reference voltage vector can be produced at the abc output terminals. Finding the correct reference values for voltage vectors is the main issue in the converter design. In order to generate a specific fault condition it is easier to have separate voltage vectors for positive and negative sequences. This way any swell, sag and phase jump could be implemented by changing the positive sequence voltage set. An unbalanced power supply condition can be emulated by setting the magnitude of the negative sequence voltage set. Furthermore, each voltage harmonic to simulate power supply distortions may have its own reference vectors. The reference voltage consists of two components in $\alpha-\beta$ axis. As we can only apply one reference vector to SVM module, that vector has to include all the information about the magnitude and phase angle of the harmonics, negative sequence, fundamental frequency etc., as follows:

$$\begin{cases} V_\alpha = V_{1\alpha}^+ + V_{1\alpha}^- + V_{3\alpha} + \dots + V_{n\alpha} \\ V_\beta = V_{1\beta}^+ + V_{1\beta}^- + V_{3\beta} + \dots + V_{n\beta} \end{cases} \quad (4.1)$$

where, + and - superscripts describe positive and negative sequence components V_α and V_β are the $\alpha-\beta$ components of the reference vector that needs to be applied in the SVM module and 1,3,...n subscripts represent the fundamental and harmonic components up to nth harmonic.

For each component the following can be written:

$$\begin{cases} V_{1\alpha}^+ = V_1^+ \cos(\omega t + \theta_1^+) \\ V_{1\beta}^+ = V_1^+ \sin(\omega t + \theta_1^+) \\ V_{1\alpha}^- = V_1^- \cos(-\omega t + \theta_1^-) \\ V_{1\beta}^- = V_1^- \sin(-\omega t + \theta_1^-) \\ V_{3\alpha} = V_3 \cos(3\omega t + \theta_3) \\ V_{3\beta} = V_3 \sin(3\omega t + \theta_3) \\ \vdots \\ V_{n\alpha} = V_n \cos(n\omega t + \theta_n) \\ V_{n\beta} = V_n \sin(n\omega t + \theta_n) \end{cases} \quad (4.2)$$

where, $\omega = 2\pi/T$ and T is one cycle of the fundamental frequency and θ is the angular position of each components. Fig 4.3 shows the vector base representation of reference values for each component. As

shown, unlike the negative sequence component, all the voltage harmonic components would rotate in the same direction as the positive component.

Needless to say, as we are using SVM to have a constant switching frequency, designing a filter to remove high frequency components is not an issue.

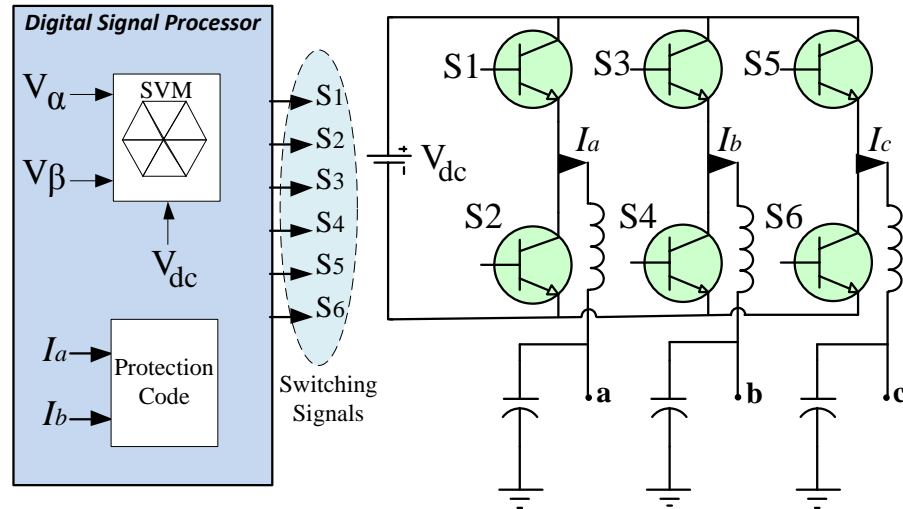


Fig 4.2. Schematics of three phase power supply fault emulator

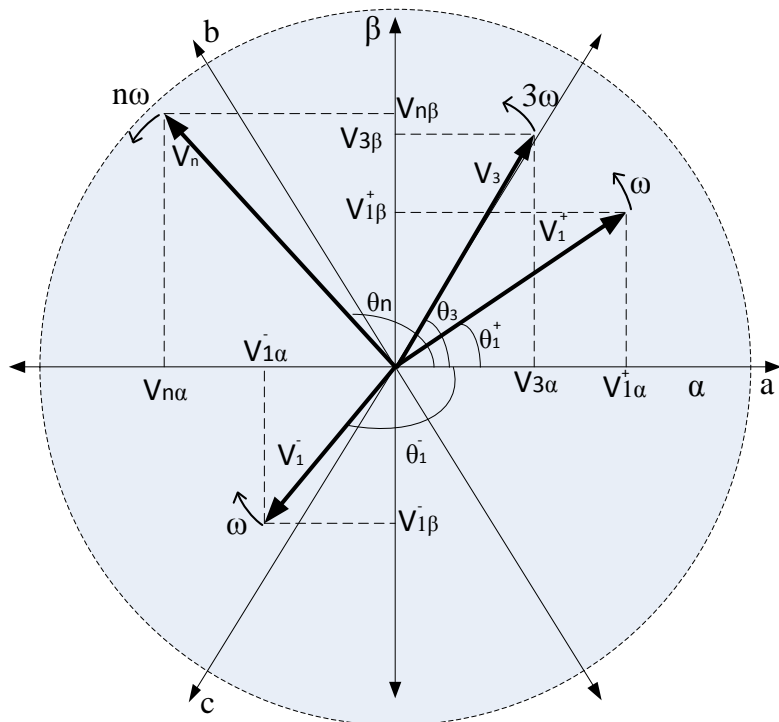


Fig 4.3. Vector base representation of reference values for different components.

4.3. Voltage Sag Transient Disturbances

The focus of this experimental investigation is the short duration power system voltage transients known as sags (or dips) and how they affect transformer operation. The developed hardware fault emulator will be utilized to precisely generate various types of voltage sag transients imposed upon a three-phase transformer. It is therefore worthwhile to discuss the characteristics of the voltage sag phenomenon as well as their causes and detrimental effects in modern power systems and equipment.

4.3.1. IEEE-1159 Definition of Voltage Sag

Voltage sags are classified by the IEEE as short duration power quality disturbances . Specifically, the IEEE-1159 Standard (2009) states that a voltage sag is a decrease in the rms voltage at the power frequency for durations from 0.5 cycles to 1 minute, although they typically only last a maximum of a few cycles due to fast acting protection equipment. There are a multitude of fault modes in three-phase systems resulting in voltage sags that can be of the symmetrical type or unsymmetrical type. Symmetrical sags are intrinsic to balanced three-phase faults resulting in simultaneous sags occurring in all three-phase line or phase voltages. More common is the unsymmetrical sag types occurring for unsymmetrical faults (e.g., line-to-line or line-to-ground). Both types of sag disturbances are investigated in this chapter.

4.3.2. Causes of Voltage Sag

Short interruptions and most long interruptions usually originate in the local distribution network. However, it can be caused by short-circuit faults hundreds of kilometers away in the transmission system. The primary causes of these voltage sags are (Bollen, 2000, Masoum et al., 2010, Fuchs and Masoum, 2008, Iravani et al., 1995):

- Starting of large induction motors.
- Capacitor or reactor bank switching.
- Energization of heavy loads (e.g., arc furnace).
- Transmission and distribution faults.
- Fast bus transfer of load from one power source to another.

4.3.3. Symptoms of Voltage Sags on Power Systems

Most equipment in power systems are extremely sensitive to power quality disturbances and therefore transients like voltage sags often have a large impact on system reliability. Those most significantly

affected are control systems and variable speed drives with respect to industry operations. Main detrimental effects of voltage sags are (Bollen, 2000, Masoum et al., 2010, Fuchs and Masoum, 2008):

- Costly production wastage due to interrupted and spoilt process materials
- Transformer saturation producing high inrush currents.
- Improper operation of variable speed AC drives due to the drop in DC bus voltage.
- malfunctioning of GSC that leads to disturbances in DC bus in wind turbines

With the aid of the developed fault emulator, the transient current behavior in three-phase transformers upon voltage sag recovery will be investigated in this section.

4.3.4. Voltage Sag Magnitude

The most important characteristics of voltage sag are magnitude and duration; however, the during-sag voltage may also contain a rather large amount of higher frequency components. Main approaches are to compute sag magnitude from rms voltage, fundamental voltage component, or peak voltage. These values can be computed over each cycle or half-cycle. As long as the voltage is sinusoidal, it does not matter which approach is used. These methods will give a range of values, with the smallest value being taken as the magnitude of the sag. Most sags have a fairly constant value during the deepest part and allows one to use a single value to represent the sag.

Voltage sags are typically given as a percentage of the nominal voltage to avoid confusion with terminology. This means that a system with a nominal line voltage of 415 V subjected to a sag to 70% would result in the magnitude of the sag being equal to 290.5 V. The accuracy of the measurement is dependent on the sensitivity and sampling time at which the monitoring equipment records the input data.

There are three main calculation approaches to compute the sag magnitude:

- a) *Sag magnitude from RMS voltage-* since voltage sags are recorded as sampled points, the rms voltage can be numerically calculated as:

$$V_{rms} = \sqrt{\frac{1}{N} \sum_{i=1}^N v_i^2} \quad (4.3)$$

where N and v_i are the number of samples per cycle and the sampled voltage (in time domain), respectively.

- b) *Sag magnitude from fundamental voltage-* the magnitude of the voltage sag can also be computed using the fundamental voltage component method, which takes the voltage as a function of time and

results in a complex function. To calculate the magnitude, the absolute of this value is taken, while the argument can be used to calculate the so called phase-angle jump. The fundamental voltage component as a function of time may be calculated as:

$$V_{\text{fundmental}}(t) = \frac{2}{T} \int_{t-T}^t v(\tau) e^{j\omega\tau} d\tau \quad (4.4)$$

This equation results in a complex number as a function of time. The absolute value of this complex number is the voltage magnitude as a function of time.

c) *Sag magnitude from peak voltage-* the peak voltage as a function of time can be obtained using:

$$V_{\text{peak}} = \max_{0 < \tau < T} |v(t - \tau)| \quad (4.5)$$

where $v(t)$ is the sampled voltage waveform and T is an integer multiple of one half-cycle.

In this chapter, the definition of Eq. 5 is used to define experimented voltage sag magnitudes.

Transient Operation in Three-Phase Transformers

There have been very few attempts at studying the transient operation of three-phase transformers considering ferromagnetic nonlinearities and magnetic interactions of fluxes present in multi-leg core geometries. The essential attributes governing three-phase transformer transient behavior are (1) electrical coupling due to winding connections, (2) magnetic coupling and core flux interaction due to core topologies (e.g., three-leg, five-leg designs), (3) nonlinear core representation and (4) lossy behavior due to the ohmic, hysteresis and eddy current losses. A physically accurate representation of these effects is the coupled equivalent electric and magnetic circuits of the transformer windings and core structure as shown in Fig 4.4 for a three-leg transformer (Moses et al., 2010).

As can be inferred by Fig 4.4, voltage sags will have the effect of not only affecting the transformer terminal voltages, but also impact the seldom investigated internal magnetomotive forces which affect the flow of fluxes within the transformer core. Although the terminal voltages are related to the core fluxes by Faraday's Law, there is also an important interaction of fluxes in each leg with one another that also affects the transformers electromagnetic transient behavior. Depending on the type of fault, the core leg fluxes could be driven above their rated values thereby saturating the transformer core resulting in large magnetizing currents.

Furthermore, each core-leg exhibits different and asymmetric saturation behavior due to the differences in the core-leg geometry (e.g., centre leg is shorter). This has seldom been considered in transient studies of three-phase transformers. The experimental study carried out in this chapter sheds light on the transient current behavior in an asymmetric three-leg transformer core subjected to symmetrical and unsymmetrical voltage sag transients.

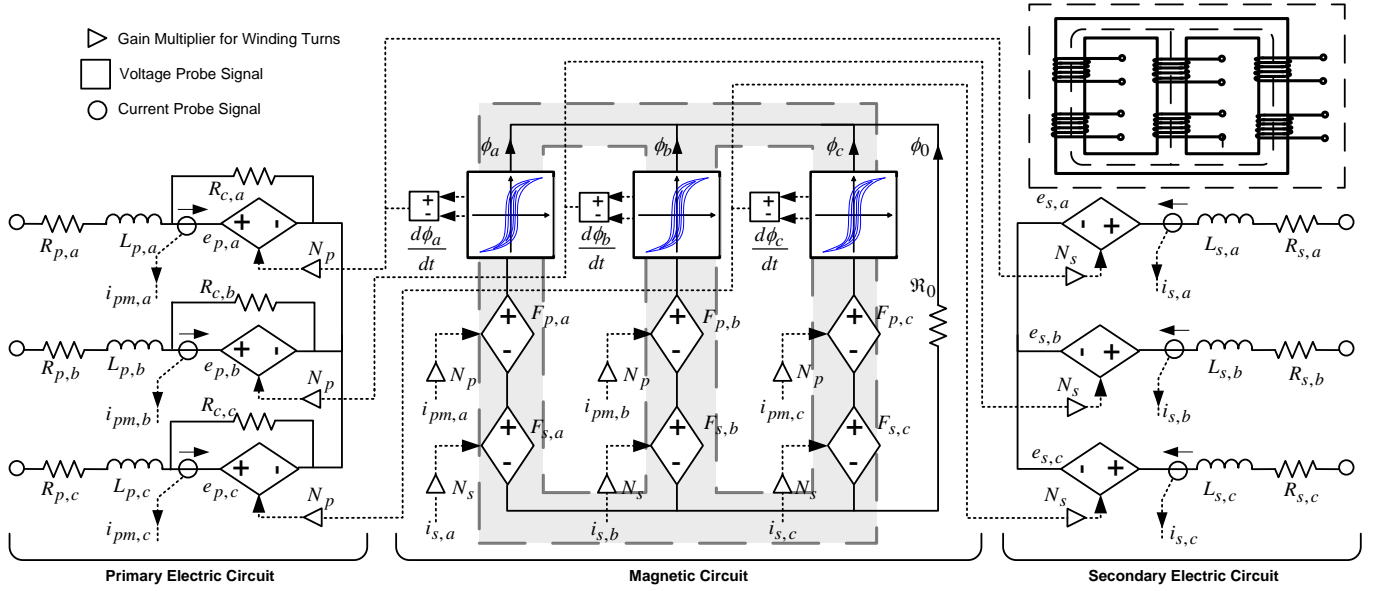


Fig 4.4. Three-phase three-leg transformer representation depicting the electromagnetic couplings of winding mmfs, voltages, currents and core-leg fluxes

4.4. Experimental Results

In order to test the performance of the prototyped fault emulator, the three phase outputs of the device are connected to the low voltage terminals of a three-phase three-leg transformer. The transformer primary and secondary windings are rated at 440 and 55 V (10 A), respectively, and operate at a nominal power frequency of 50 Hz. For this experiment, the transformer is operating under no-load and the windings are connected in wye-G/wye-G configuration resulting in primary/secondary line voltages of $440\sqrt{3} / 55\sqrt{3}$ V. The electrical data of the transformer is listed in Table 4.1. Further information about the transformer characteristics are available in (Moses et al., 2010, Moses et al., 2011).

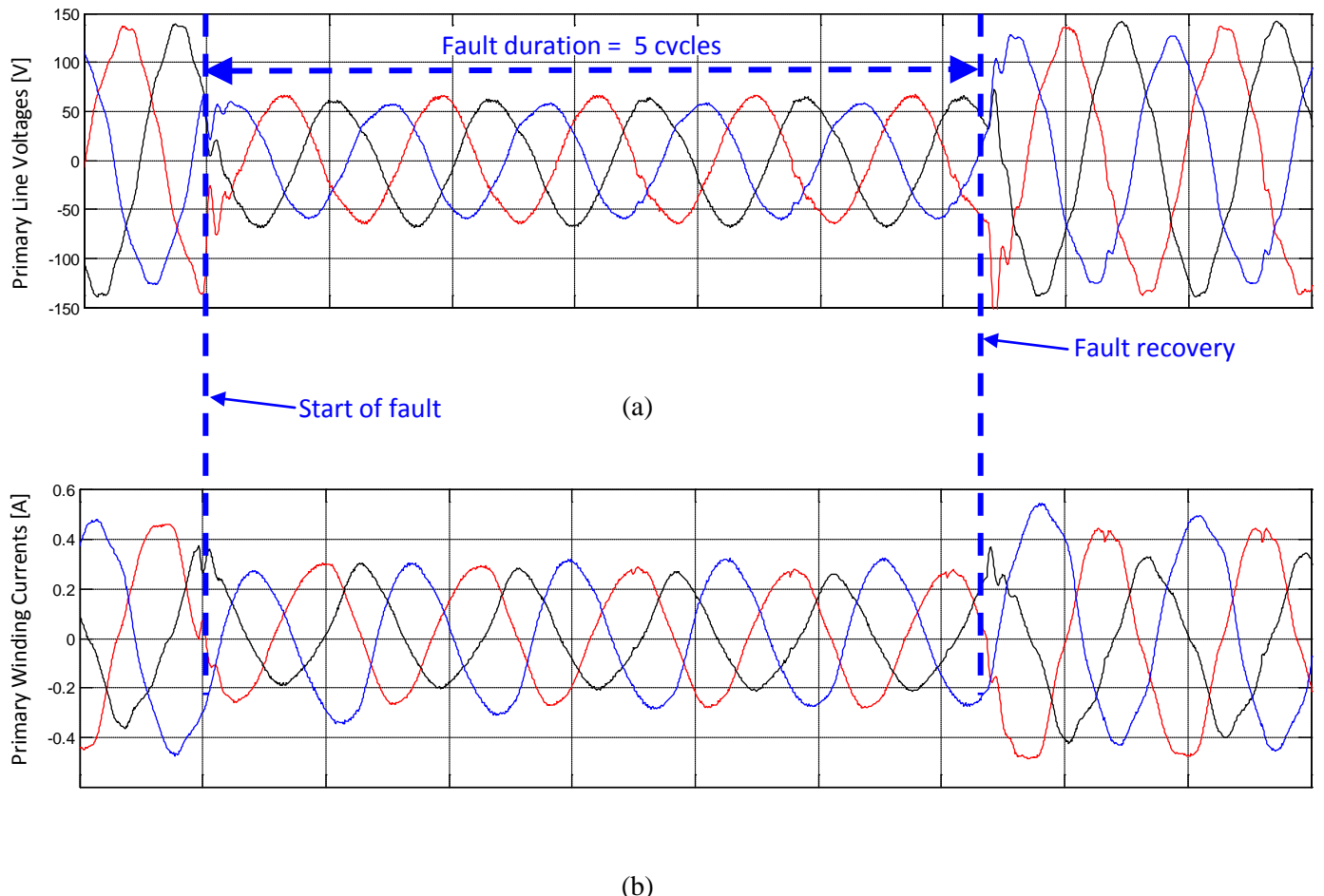


Fig 4.5. Impact of three-phase symmetrical sag imposed upon transformer terminals. (a) Primary line voltage waveforms and (b) transformer magnetizing currents. Fault duration = 5 cycles.

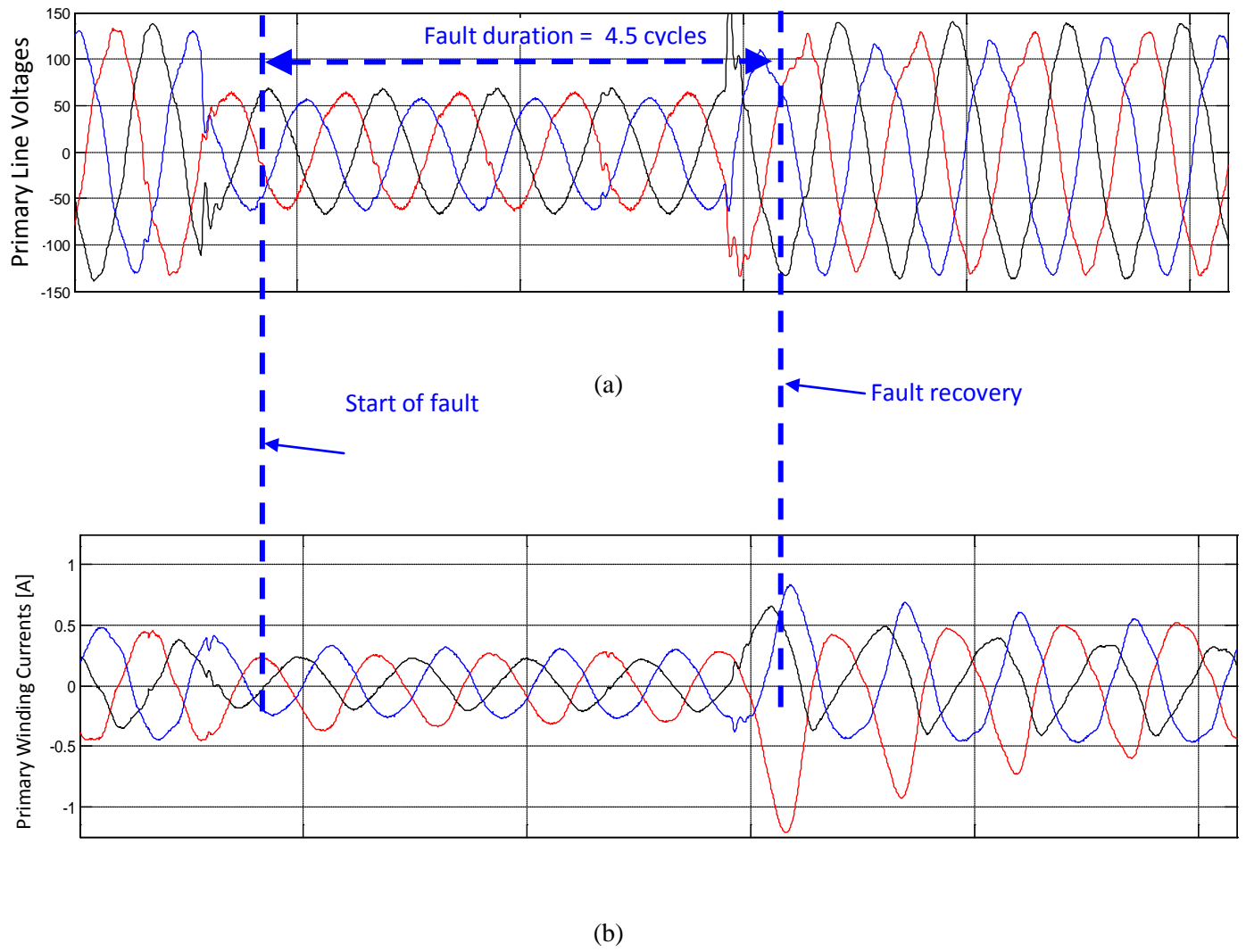


Fig 4.6. Impact of three-phase symmetrical sag imposed upon transformer terminals. (a) Primary line voltage waveforms and (b) transformer magnetizing currents. Fault duration = 4.5 cycles.

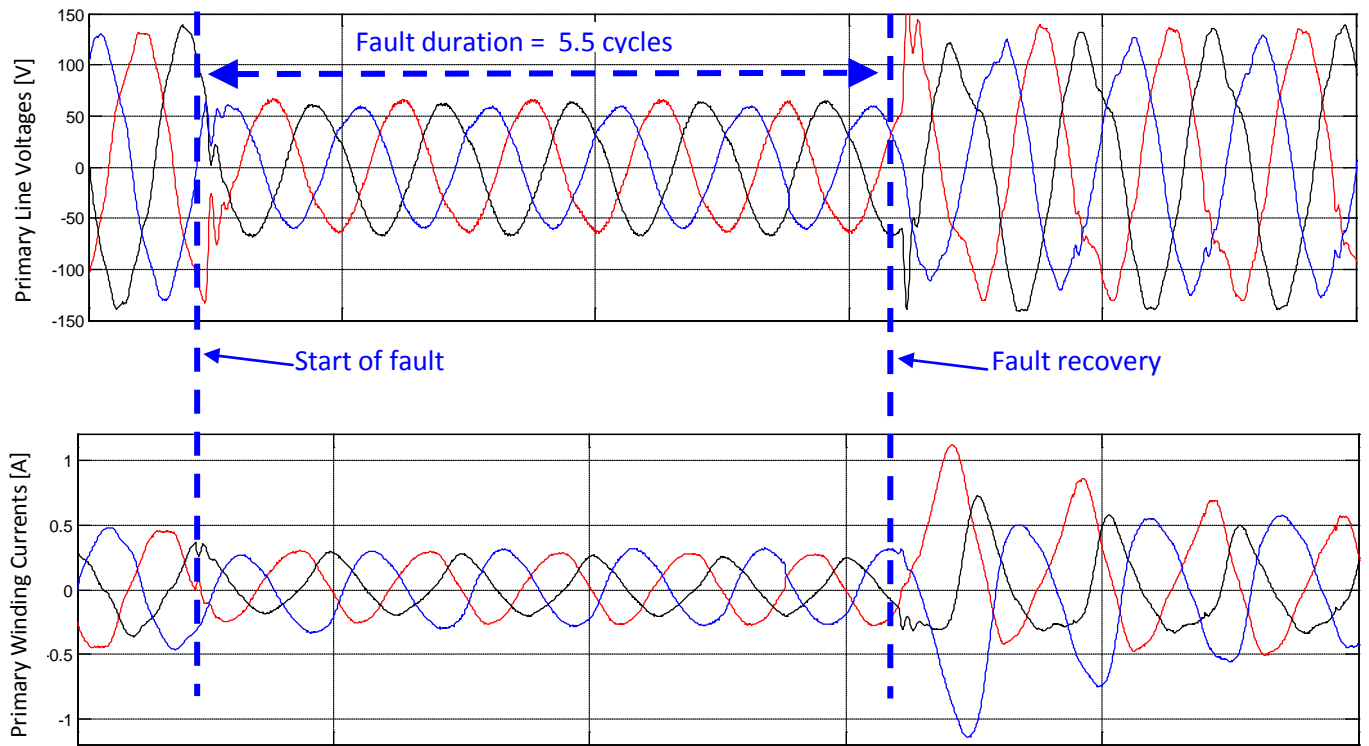


Fig 4.7. Impact of three-phase symmetrical sag imposed upon transformer terminals. (a) Primary line voltage waveforms and (b) transformer magnetizing currents. Fault duration = 5.5 cycles.

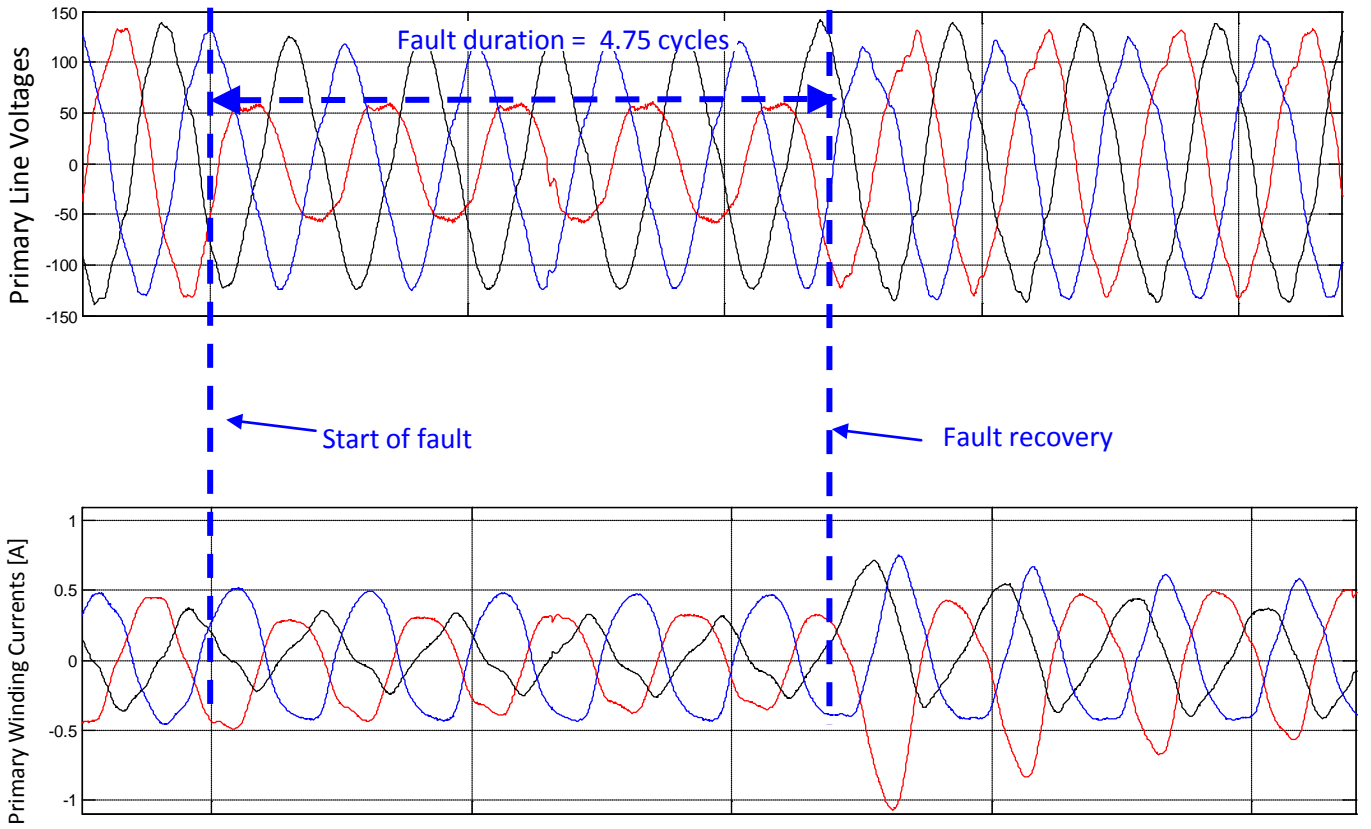


Fig 4.8. Impact of three-phase unsymmetrical sag imposed upon transformer terminals. (a) Primary line voltage waveforms and (b) transformer magnetizing currents. Fault duration = 4.75 cycles.

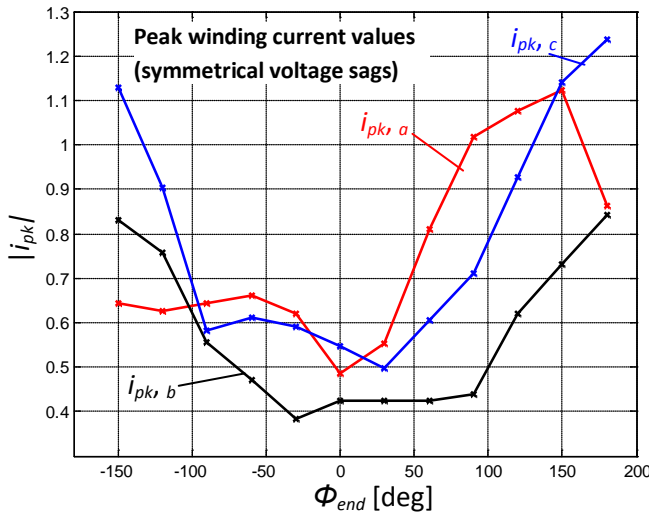


Fig 4.9. Measured effects of different sag recovery angles ϕ_{end} (symmetrical sag conditions) and fixed sag starting angle $\phi_{start} = 0^\circ$ on absolute peak values of transformer winding current amplitudes $|i_{pk}|$.

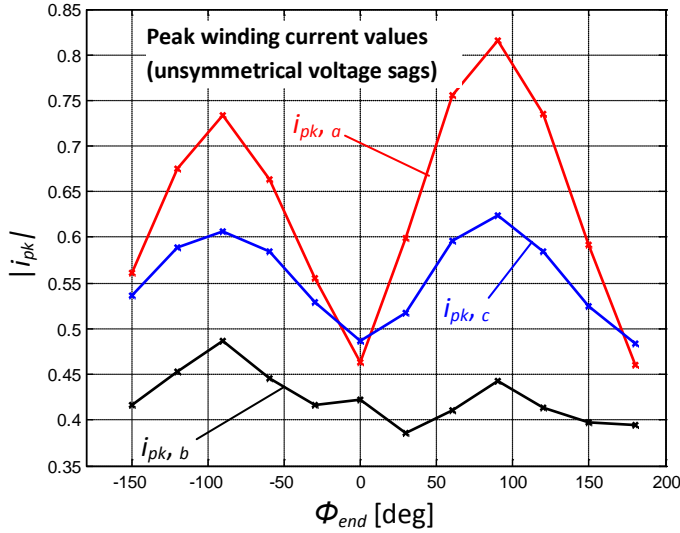


Fig 4.10. Measured effects of different sag recovery angle ϕ_{end} in phase a only (unsymmetrical sag conditions) and fixed sag starting angle $\phi_{start} = 0^\circ$ on absolute peak values of transformer winding current amplitudes $|i_{pk}|$.

4.4.1. Measurement Methodology

A number of tests for symmetrical and unsymmetrical voltage sags are performed to evaluate the performance of the fault emulator with the transformer. The fault emulator can be easily programmed with specified fault durations, sag depth as well as fault angles for starting and recovery instants that are referenced to the troughs of the voltage waveform in phase a-b. The programmed fault angles carry a ± 1 degree experimental uncertainty. Measurements of transformer primary line voltages and winding currents are made using the Hioki 3196 power quality analyzer capable of automatically detecting and capturing waveforms of fault transients such as voltage sags. The waveforms are stored digitally and are transferred to a computer for analysis and plotting. For all results, each test was performed at least three times to verify the consistency and repeatability of observed waveforms.

4.4.2. Results

The fault emulator was first configured to subject the transformer to balanced symmetrical voltage sags at 50% magnitude at the transformer primary terminals. This is typical of fault conditions that may occur on transmission lines upstream from the transformer. Figs 4.5-4.7 show the transformer magnetizing currents for three different sag instants. If the voltage sag initiation and recovery angles are timed correctly, then it is possible that no significant inrush currents occur as indicated

in Fig 4.5. However, if the recovery angle is varied by a small degree, significant increases in transformer currents occur as shown in Figs 4.6-4.7 which could potentially damage transformer windings and insulation.

It is worthwhile noting that despite the balanced nature of the emulated fault, the transformer currents are asymmetric in wave-shape. This is primarily due to the fact that each core-leg exhibits different ferromagnetic properties since the core structure in three-leg designs is asymmetric (centre leg is shorter). Therefore, upon fault recovery, the flow of transformer magnetic fluxes can become unevenly biased within the magnetic circuit (Fig 4.4) resulting in different saturation levels and observed magnetizing currents in each core-leg.

In the next test, the effect of unsymmetrical voltage sags imposed upon the transformer terminals was tested. This is a more common scenario compared to symmetrical faults. The fault emulator was configured for simulating a single-phase fault by imposing a 50% voltage sag on line-to-line voltage a-b supplying the transformer (Fig 4.8). Under such sag conditions, the unbalanced transformer terminal voltages result in imbalances in the internal magnetomotive forces supporting the core-leg fluxes which also become unbalanced. Although a single-phase fault is simulated, due to the transformer magnetic circuit couplings, all other line currents supplying the transformer are affected during and after the voltage sag. When the voltage sag recovers, significant inrush currents are observed in all three-phases which eventually decay to steady-state values. These excessive peak transformer currents can cause permanent transformer damage.

For a more precise investigation of the relation of voltage sag recovery angles on peak transformer currents, the fault emulator was programmed to vary the recovery angle between -180 and +180 degrees relative to the negative voltage peak for symmetrical and unsymmetrical sags. Fig 4.9 shows samples of the measured peak currents of the transformer windings for different symmetrical voltage sag recovery angles. Note that due to the aforementioned core structure asymmetry and magnetic couplings in the transformer, the variation in peak currents is not identical in each phase. As can be noted, all observed winding peak currents can exhibit significant variations depending on the fault recovery instants.

The variation in peak transformer currents for different unsymmetrical voltage sag recovery instants is shown in Fig 4.10. The pattern of peak current variations is significantly different to the symmetrical voltage recovery case. Unlike the symmetrical sag case, two recognizable maxima for peak currents can be distinguished for each of the three-phase winding currents. The peak current maxima occur for the same recovery angles in each phase which is a consequence of the strong magnetic couplings present in the transformer core.

A hardware fault emulator has thus been successfully trialed to carry out very precise fault measurements of transient behavior in three-phase three-leg transformers for different fault scenarios. The experimental results are in agreement with theoretical predictions previously offered by software based modeling studies(Masoum et al., 2010, Pedra et al., 2005). This experimental approach is easily customizable for wider applications in testing other power components subjected to a variety of power system disturbances.

4.5. Conclusion

In this chapter, the implementation of a hardware fault simulator prototype is described and presented. A space vector based analysis of each voltage components including positive and negative sequences and different voltage harmonic components provides us a tool to generate a variety of possible three phase voltage source failures as well as voltage sag, swell, voltage unbalance, harmonics, dc-bias, phase jump and etc. Then the simulator has been used to study the effect of balanced and unbalanced voltage sags on a low voltage three-phase three-leg power transformer. Results demonstrate the capability of the fault emulator in studying the impact on grid simulated by a three phase transformer.

TABLE 4.1 - Transformer Electric Circuit Test Data

Description	Data
Rated primary winding voltage (v_p)	440 V
Rated secondary winding voltage (v_s)	55 V
Turns ratio (N)	8
Operating frequency (f)	50 Hz
Rated secondary current (i_s)	10 A
Primary winding resistance (R_{pa}, R_{pb}, R_{pc})	9.423 Ω (0.0268 pu)
Secondary winding resistance (R_{sa}, R_{sb}, R_{sc})	0.147 Ω (0.0268 pu)
Primary leakage inductance (L_{pa}, L_{pb}, L_{pc})	6.341 mH (0.00566 pu)
Secondary leakage inductance (L_{sa}, L_{sb}, L_{sc})	0.0991 mH (0.00566 pu)

$$Z_{p, \text{base}} = N^2 \cdot Z_{s, \text{base}} = N^2 \cdot v_{s, (\text{rated})} / i_{s, (\text{rated})} \text{ (primary referred)}$$

4.6. References

- BOLLEN, M. H. J. (2003) Voltage recovery after unbalanced and balanced voltage dips in three-phase systems. *IEEE Transactions on Power Delivery*, 18, 1376-1381.
- CARDELLI, E., DELLA TORRE, E., ESPOSITO, V. & FABA, A. (2009) Theoretical considerations of magnetic hysteresis and transformer inrush current. *IEEE Transactions on Magnetics*, 45, 5247-5250.
- FUCHS, E. F. & MASOUM, M. A. S. (2008) *Power quality in power systems and electrical machines*, Academic Press/Elsevier.
- IRAVANI, M. R., CHAUDHARY, A. K. S., GIESBRECHT, W. J., HASSAN, I. E., KERI, A. J. F., LEE, K. C., MARTINEZ, J. A., MORCHED, A. S., MORK, B. A., PARNIANI, M., SHARSHAR, A., SHIRMOHAMMADI, D., WALLING, R. A. & WOODFORD, D. A. (1995) Modelling and analysis guidelines for slow transients-Part I. Torsional oscillations; transient torques; turbine blade vibrations; fast bus transfer. *IEEE Transactions on Power Delivery*, 10, 1950-1955.
- MASOUM, A., MOSES, P. S. & ABU-SIADA, A. (2010) Impact of voltage sags on three-phase power transformers. *Proc. Australasian Universities Power Engineering Conference (AUPEC)*. Christchurch, New Zealand.
- MOSES, P. S., MASOUM, M. A. S. & TOLIYAT, H. A. (2010) Dynamic modeling of three-phase asymmetric power transformers with magnetic hysteresis: no-load and inrush conditions. *IEEE Transactions on Energy Conversion*, 25, 1040-1047.
- MOSES, P. S., MASOUM, M. A. S. & TOLIYAT, H. A. (2011) Impacts of hysteresis and magnetic couplings on the stability domain of ferroresonance in asymmetric three-phase three-leg transformers. *IEEE Transactions on Energy Conversion*, 26, 581-592.
- PEDRA, J., SAINZ, L., CORCOLES, F. & GUASCH, L. (2005) Symmetrical and unsymmetrical voltage sag effects on three-phase transformers. *IEEE Transactions on Power Delivery*, 20, 1683-1691.
- SAINZ, L., CORCOLES, F., PEDRA, J. & GUASCH, L. (2007) Theoretical calculation of inrush currents in three- and five-legged core transformers. *IEEE Transactions on Power Delivery*, 22, 986-995.
- STYVAKTAKIS, E. & BOLLEN, M. H. J. (2003) Signatures of voltage dips: transformer saturation and multistage dips. *IEEE Transactions on Power Delivery*, 18, 265-270.

Chapter 5

Conclusions

5.1. Summary of Dissertation

In this thesis, a set of new converter /control techniques are developed for the Grid Side and Rotor Side converter applications in DFIG wind power generation. A real time digital simulation technique is also presented which is capable of studying in real time the performance of the DFIG wind power generator connected to grid. A number of practical control strategies for DFIGs are implemented and their performances are compared. Results show that a new improved direct power controller is able to provide very quick transient response for both the active power and the reactive power output from the DFIG wind energy conversion system. Extensive simulations and practical implementation of the algorithms on a digital controller embedded inside a digital signal processor are implemented. The hardware and software of the developed prototype DFIG control mechanism is described in detail in this dissertation. In addition, to study the effect of voltage sag and other types of transient disturbances and faults, a prototype of a fault generator using the same digital signal processor has been implemented. Effect of such disturbances on a transformer is investigated which is the nearest most probable location of a grid fault or disturbance.

In chapter one, an introduction followed by literature review is presented. In the literature review, a variety of control methods for DFIG are evaluated. In particular suitability of these methods are investigated to satisfy related grid codes for unbalance voltages, voltage sag and active power and reactive power control.

Chapter two, is dedicated to grid side converter, and presents four different control solutions for the GSC.

The first proposed method is the *direct active power control*, which is based on instantaneous dc-side current demand. In the provided solution:

- PLL circuit is eliminated
- Computation time is reduced and high sampling rates are not required.
- Dynamic response is fast and transient distortions with balanced and unbalanced source voltages are negligible.
- High frequency current harmonics are minimal and there is no need for ferrite cores or high frequency inductors.
- The reference signal can be generated in a single switching cycle and there is negligible dc voltage disturbance.
- Unlike conventional ac-dc systems the output dc voltage can be higher or lower than the maximum value of input voltage.

- In the buck operating mode, smaller voltage rating of switches can be selected and high voltage supplies can operate with low voltage switches.

The second proposed method is *Improved Predictive Direct Power Control*, which offers a more accurate mathematical model to improve the performance of a recently introduced predictive direct power controller (P-DPC). The method provides a constant switching frequency and can effectively follow the active and reactive power references. The proposed controller is very fast with no steady state error which makes it especially suitable for high power applications with low switching frequencies e.g. working as GSC.

The third method is a new *fuzzy predictive direct power control (FP-DPC)* strategy, simulated and implemented using a Texas Instrument digital signal processor. While on the control loop, two separate fuzzy blocks modify the active and reactive power error signals before applying it to an improved predictive direct power control module. The idea behind this new strategy is to reduce the stress on the control system in steady state condition and also to obtain a faster transient response. The resulting controller benefits from the smoothness of conventional vector based solutions and the natural quick response of predictive methods.

Based on simulation and experimental results, the FP-DPC method has the following advantages:

- It uses a vector base switching pattern with a constant switching frequency.
- It utilizes an accurate converter model that ensures better operation in low switching or high power applications without substantial sub-switching oscillations.
- Due to the application of a simple fuzzy signal conditioner block, the new controller is less sensitive to parameter variations i.e. input inductor estimation errors.

The fourth method is the proposed *Average Current Control* strategy, which has a constant frequency. This controller benefits from both space vector modulation technique and average current control (ACC) strategy. The controller advantages are as follows:

- This method decrease switching losses in system by keeping the switching frequency constant.
- Its implementation is relatively simple compared to existing approaches.
- The method exhibit a very fast transient response similar to the conventional HCC.
- The method is especially suitable for high power applications with low switching frequencies e.g. grid side converters, and rectifier of electric vehicles.

In chapter three, a real time digital control of DFIG system design is presented. The setup is particularly useful to study various control techniques for DFIG wind turbines. A current controlled (CC) method as an example is implemented and verified by a number of experiments to test the controller's steady state and transient performances. Experimental results show that using proper rotor current control, the DFIG is capable of generating both active and reactive power.

In chapter four, the implementation of a hardware fault simulator prototype is described and presented. A vector based analysis of each voltage components including positive, negative sequences and different voltage harmonic components provides us a tool to generate a variety of possible three phase voltage source failures as well as voltage sag, swell, voltage unbalance, harmonics, dc-bias, phase jump and etc. In this work, an application of the fault simulator has been demonstrated by studying the electromagnetic effects of balanced and unbalanced voltage sags on a low voltage three-phase three-leg power transformer.

5.2. Contributions

The key results of arising from this dissertation have been published in 8 refereed journal and international conferences. The key contributions are as follows:

- Introducing the concept of direct active power control strategy and investigating its application for DFIG
- Improving an existing predictive method for three phase power converters to be employed in GSC
- Providing a smart control strategy for the three phase converters using the fuzzy and predictive control method to improve dynamic and steady state response of three phase converters
- Presenting an improved average current control strategy for three phase power converters.
- Providing a detailed design document for a DFIG prototype that is able to handle variety of control strategies
- Designing and implementing of a three phase fault generator to simulate any required three phase fault e.g. voltage sag, swell, voltage unbalance, harmonics, dc-bias, and phase jump

5.3. Future works

The following topics are suggested for future research in extension of this work.

- Using the prototype real time digital simulator and the fault emulator, more studies can be performed on wind power generators to examine different control strategies and topologies under certain types of balanced and unbalanced three phase faults.
- Improved parameter estimation methods for utilizing the predictive control strategies with more accurate parameter values. This would improve the transient and steady state response of such methods.
- Investigating the operation of FP-DPC on the RSC to further improve the dynamic response of the DFIG to meet most stringent of the grid codes.
- Improving the dynamic response of the GSC by using storage units. The storage unit can limit the dc-bus voltage disturbances that occur by variety of faults. This will also lead to minimize the dc-bus capacitor value.